

APPLYING DIFFERENTIALLY POLARIZED LIGHT (DPL) IMAGING FOR  
IMPROVING VISIBILITY OF PERITONEAL METASTASES

A thesis submitted by

Robert Michael Trout

In partial fulfillment of the requirements for the degree of

Master of Science

in

Biomedical Engineering

Tufts University

May 2017

© 2017

Robert Michael Trout  
ALL RIGHTS RESERVED

Advisor: Irene Georgakoudi

## ABSTRACT

Determining whether the peritoneum is positive for metastases is an important factor when a clinician stages the progression of various abdominal cancers. Currently, the examination of the peritoneum takes place via laparoscopy, however the sensitivity with which cancer lesions are detected with this method needs improvement. This work is concerned with the application of differentially polarized light (DPL) imaging in laparoscopy to improve the contrast of surface features resembling cancer lesions. The performance of this imaging modality was assessed through examination of tissue phantoms and ex vivo samples modeling the optical properties of the metastatic peritoneum. It was found that compared to current conventional imaging, DPL imaging substantially increases the contrast of tumor tissue on a peritoneal surface in a human biopsy sample. With this, an optical system was also designed to enable DPL imaging in a clinical laparoscope.

**ACKNOWLEDGEMENTS**

Irene Georgakoudi

Xiaocheng Jiang

Martin Hunter

Thomas Schnelldorfer

Dimitra Pouli

Carlo Alonzo

Huan-Hsuan Hsu

Nishanth Krishnamurthy

## TABLE OF CONTENTS:

LIST OF FIGURES: .....	vi
CHAPTER 1: THE CLINICAL NEED AND DIFFERENTIALLY POLARIZED LIGHT .....	1
Introduction .....	1
Clinical Need: Peritoneal Metastasis Screening.....	1
Differentially Polarized Light in Biomedical Imaging.....	4
Optical Description of DPL.....	12
CHAPTER 2: TESTING THE CONCEPT .....	17
Introduction .....	17
Benchtop DPL Laparoscope Setup .....	17
Imaging Results: Optical Phantoms.....	20
CHAPTER 3: QUANTITATIVE VISUALIZATION OF CANCER LESIONS IN DPL IMAGING .....	25
Introduction .....	25
DPL Apparatus.....	25
Image Processing.....	26
Imaging Results.....	28
Imaging Analysis.....	30
CHAPTER 4: IMPLEMENTING DPL IMAGING IN A CLINICAL SETTING .....	41
Introduction .....	41
Device Design.....	41
Device Operation.....	43
Design Challenges .....	48
Device Verification.....	62
Alternative Design Considerations .....	65
CHAPTER 5: CURRENT DIRECTIONS FINAL THOUGHTS .....	67
Introduction .....	67
Additional Device Development .....	67
PDMS Phantom Testing .....	69
Conclusion.....	70
APPENDICES .....	71
A. Cancer Incidence Data.....	71

A-1. Cancer Incidence Rates .....	71
A-2. Digestive System Cancer Stage Distribution .....	71
B. MATLAB Coding.....	72
B-1. DPL Image Processing .....	72
B-2. Contrast Computation .....	73
B-3. Detected Signal Modeling .....	75
B-4. Functions .....	76
C. Device Control Code.....	79
D. Thorlabs LCC111125-A Variable Retarder Performance Data.....	87
BIBLIOGRAPHY .....	94

## LIST OF FIGURES:

Figure 1: Example image of peritoneum possessing several metastatic carcinomas. (Abid et al., 2013). .....	3
Figure 2: DPL endoscope probe design by Steve Jacques (Jacques, 2002).....	8
Figure 3: DPL endoscope probe design by the Myakov group (Myakov et al., 2002).....	9
Figure 4: (a) A rigid endoscope consists of an imaging channel and an illumination channel. (b) The Mueller polarimetric endoscope consists of a stainless-steel sheath, a motorized rotation stage, a rigid endoscope, a polarization state analyzer (PSA) and a CCD image sensor. The part that rotates during acquisition is represented in red, and the stationary part is in purple. (c) A photo of the Mueller polarimetric endoscope (Qi et al., 2016). .....	10
Figure 5: General behavior of the polarization of the reflectance from polarized illumination in bulk and surface regimes. ....	14
Figure 6: Analyzing the polarization of the reflectance signal to separate the bulk and surface reflectance. ....	15
Figure 7: Experimental optical setup designed to implement DPL imaging. ....	17
Figure 8: Mirror image of the laparoscope illumination at maximum intensity (a) and minimum intensity (b) corresponding to parallel and perpendicular analyzer orientations respectively. The ratio of the perpendicular intensity to the parallel intensity is displayed in c. ....	18
Figure 9: DPL imaging of a bead plaque-Spectralon phantom. Images for each polarization component (a parallel, b perpendicular) as well as their average and normalized difference (c and d respectively). In e, intensity as a function of position along the illustrated bisecting line is plotted, along with the raw DPL for comparison. Dashed lines indicate the boundary of the feature. 1mm scale. ....	20
Figure 10: Conventional and DPL imaging of silk scaffold implants (solid white arrows) and empty control holes (dotted white arrows) in porcine muscle. (a) presents the conventional image, while b is DPL. Intensity plots around both the silk feature (c) and empty hole (d) were created for the conventional and DPL modes. The bounds of each feature are indicated by dashed lines. 1mm scale.....	22
Figure 11: Conventional (a, b) and DPL (d, e) of porcine muscle with and without a lymphoma cell feature (circled in white) added. Intensity plots intersecting the location of the feature are presented in conventional (c) and DPL (f). The plot's intersection with the feature boundary positions are marked by the dashed lines. 1mm scale. ....	23
Figure 12: Schematic for the benchtop manual DPL imaging setup. ....	25
Figure 13: The Bayer-tiled arrangement of RGB filters over the CCD array of a color camera..	26
Figure 14: Imaging of a human ovarian tumor biopsy (circled in blue) placed atop a human peritoneum biopsy. 6a was taken in conventional non-polarized RGB, while 6e was imaged in DPL mode. The corresponding individual red, green, and blue channels are displayed alongside each image. 1mm scale. ....	28

Figure 15: Quantifying the level of contrast between a feature (tumor tissue, orange ROI) and background (healthy peritoneum, blue ROI) for the sample exhibited in fig. 11. Values for contrast calculated on this basis are presented in the plot on the left for conventional and DPL modes in color and each individual RGB channel.....	30
Figure 16: Conventional and DPL imaging (green color channel) of both a tumor (a, b) and a normal peritoneum biopsy (c, d) placed on a peritoneum background. For each of these four images, the contrast of the biopsy feature (blue) against the background (orange) is measured in color and in each individual color channel. 1mm scale.....	32
Figure 17: Comparison of glare signal versus tumor signal in the image from 8b. The signal intensity along the dotted green line is plotted below the image, with the dashed red line demarcating a glare spot, while the dashed blue lines flank the tumor signal. 1mm scale.....	34
Figure 18: Plot of the contrast values of a healthy peritoneal biopsy and a tumor biopsy for a given RGB color channel and imaging modality. Values derived from the sample exhibited in fig. 8.....	37
Figure 19: Mapping of the per-pixel contrast against the average image intensity for the same image set presented in fig. 13. 1mm scale.....	38
Figure 20: (a) Grayscale DPL image of a tumor biopsy placed on a peritoneum background (image from 13b). Insets b and c illustrate the standard and dilated glare masks applied to the image in a. 1mm scale.....	39
Figure 21: Simplified diagram of a clinical laparoscope.....	41
Figure 22: Modified laparoscope setup designed to implement DPL imaging.....	42
Figure 23: Plot illustrating the dependence of the retardance on light wavelength and applied voltage for the wavelength retarder model used here (Thorlabs 2017).....	44
Figure 24: Diagram of the experimental setup for determining the optimal half-wave retarding voltage.....	45
Figure 25: Plot of the average intensity for the raw Bayer-tiled images of a white standard at various retarder voltages. The maximum of the plot is indicated by the dashed red line at 1.4V.....	46
Figure 26: Imaging results collected from the setup in figure 24 for the half-wave retarding voltage (a, 1.4V) and zero retarding voltage (b, 25V). The ratio of b to a is displayed in c. .	46
Figure 27: Time course for the operation of the camera shutter in conjunction with the wavelength retarder.....	47
Figure 28: Mueller matrix values as a function of position within the field of view of a Karl-Storz laparoscope with a sapphire window (a), and a fused silica window (b) (Qi et al., 2012). .....	53
Figure 29: Fraction of error in signal due to the wavelength dependencies of the retarder as a function of signal wavelength.....	58

Figure 30: Plot of the measured illumination intensity spectrum for the xenon arc lamp used in the Storz laparoscope. Spectrum is modeled by a Gaussian. ....	59
Figure 31: Detection efficiency spectra for the RGB camera used (FLIR 2017). Manufacturer-provided data in a, corresponding Gaussian models of this data in b.....	60
Figure 32: Expected and observed spectra for the RGB camera signal detection of the illumination. Expected case is without the influence of the retarder error (solid lines), observed is with this error included (dashed lines).....	61
Figure 33: Process diagram describing the fabrication of a PDMS optical phantom with controlled feature geometry. ....	63
Figure 34: (a) SolidWorks model of the printed mold defining feature geometries. (b) PDMS phantom resulting from the mold printed from this design. ....	64



## **CHAPTER 1: THE CLINICAL NEED AND DIFFERENTIALLY POLARIZED LIGHT**

### **Introduction**

It is the purpose of this chapter to outline the clinical need, describe the optical behavior of differentially polarized light (DPL) imaging, and address how this behavior is exploited and serves as a means of addressing the clinical need.

### **Clinical Need: Peritoneal Metastasis Screening**

For patients who suffer from the numerous varieties of abdominal cancer (ovarian, bowel, pancreatic, etc.), the prescribed treatment protocol can depend heavily on the degree of the cancer's progression. Thus, it is important the clinician is aware of the severity of the case and can accurately stage its advancement in the patient. If the accuracy of this staging is in question, so too is the efficacy of the prescribed treatment.

To illustrate this clinical scenario, consider a hypothetical patient suffering from gastrointestinal cancer. In general, the standard treatment options available for this patient consist of surgery, chemotherapy, radiation therapy, or a combination of these. As mentioned, the application of these treatments will vary depending on the stage of the cancer. Stage 0 gastrointestinal cancer patients exhibit some abnormal (precancerous) cell phenotypes within the mucosa (innermost tissue lining of the intestine). This stage is effectively treated through surgery, excising the suspicious tissue in a gastrectomy. Stage I is characterized by the distinct development of cancerous tissue within the mucosa/submucosa or the muscle layer of the stomach. Treatment also includes gastrectomy, but the surgery may also be followed by chemoradiation therapy. Stage II cancer has spread farther towards the stomach (present in the

serosa and sub serosal membranes surrounding the stomach) and/or has reached up to 6 lymph nodes near the primary tumor. Now more aggressive gastrotomies are applied, consistently followed by postoperative chemo- and radio-therapy. By stage III, the cancer has potentially spread to other nearby organs, and/or compromised 7 or more lymph nodes. Effective treatment often requires radical surgical resection in conjunction with aggressive post- and peri-operative chemoradiation therapy. Finally, in the case of a stage IV patient, the presence of cancer is detected in areas in the body more distant from the primary tumor than those detailed in previous stages, and is associated with metastasis. In cases such as these, only palliative treatments are pursued as it is effectively impossible to cure the disease at this point. Thus, surgery is rare unless it is required to remove an obstruction, and other therapies are only applied where they would provide relief from symptoms and improve patient quality of life (NIH, 2017).

Here, the concern is specifically with the diagnosis of stage IV cancer patients exhibiting signs of metastasis. The patient group this applies to is significant: according to data reported by the Surveillance, Epidemiology, and End Results Program of the National Institute of Health (Cancer Statistics, 2017), of all newly diagnosed cancer patients in the United States from 2005-2014, abdominal cancers composed over 20% of the cases. Of these incidences of abdominal cancer, 27.3% exhibited metastasis. Thus, approximately 5.5% of all new cancer patients are positive for metastatic abdominal cancers and are candidates for laparoscopic examination. The data from which these statistics are derived may be examined in appendix A. Given the annual increase of 1.7 million new cases of cancer predicted for 2017 (Siegal et al., 2017), this means that nearly 100,000 new cases of metastatic abdominal cancers will arise this year.

As detailed earlier, the metastatic-stage cases of interest here are defined by the presence of cancer tissue growth in sites distant from that of the primary tumor. One common procedure by which the clinician may detect such satellite growths involves the visual screening of the interior of the peritoneum for the presence of cancer lesions. The peritoneum is a thin tissue membrane that surrounds the abdominal organs; in the event where an abdominal tumor becomes metastatic, small white lesions commonly form on its surface, detailed in the figure below:

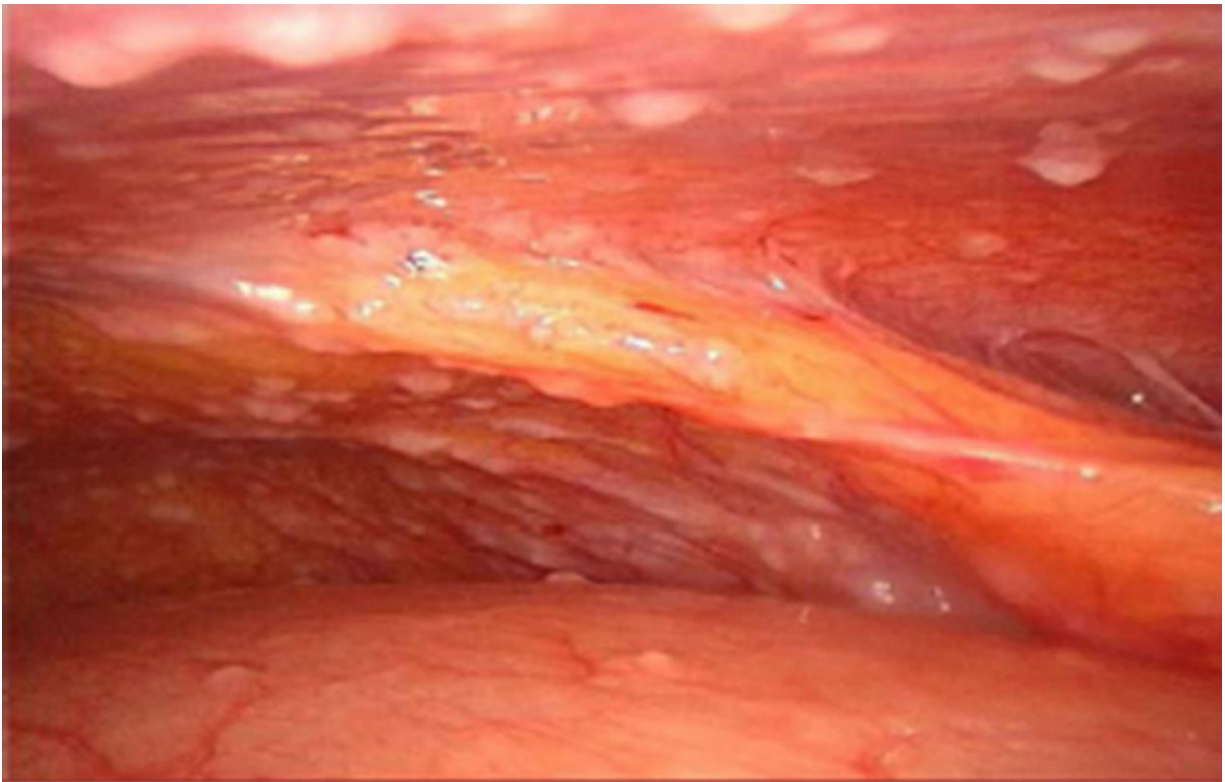


*Figure 1: Example image of peritoneum possessing several metastatic carcinomas. (Abid et al., 2013).*

Currently, the procedure by which this screening takes place involves the insertion of an optical device called a laparoscope into the abdomen through an incision. Once inserted, the clinician may conduct their search of the peritoneum for metastases as the laparoscope relays the image of the interior. Accordingly, obtaining a detailed image of the peritoneum surface is of great interest to clinicians to more reliably identify the lesions.

Unfortunately, utilizing current laparoscopic imaging techniques, the sensitivity with which the clinician can identify the presence of these lesions is unsatisfactory, with false negative rates as high as 36% (Schnelldorfer et al., 2014) in complete laparotomies. The consequence of these false negatives is that they result in the application of a treatment plan for non-metastatic cancers to a pathology that is metastatic. However, if the diagnosis for metastasis is a false negative, more aggressive treatment likely associated with stage II and III cancers will be applied under the assumption that there is a chance of inducing remission in these stages. This results in a reduction in the patient's quality of life as they undergo costly and strenuous treatment measures which will not likely result in remission due to the undiagnosed metastatic nature of their cancer. It is this scenario that drives clinical need: it is desired to prevent the baseless reduction in patient quality of life caused by false negatives. To achieve this, it is proposed to improve the ability of laparoscopy to visualize metastatic lesions of the peritoneum. With this, the sensitivity of laparoscopic imaging to metastatic cancer would improve, reducing the rate of false negatives for cancer metastasis.

### **Differentially Polarized Light in Biomedical Imaging**

Given that much of this work is concerned with optical techniques, it is useful to frame the pathology described here in an optical context before proceeding. In the case of standard imaging like that in fig. 1, the primary source of optical contrast between the lesions and the peritoneum is their difference in absorption. The absorbance spectrum of the peritoneum is dominated by the hemoglobin contained in the blood vessels of the tissue, imparting a reddish appearance to the reflectance. Conversely, the cancer tissue composing the lesions is not so heavily infiltrated by blood vessels and thus does not contain any significant absorbing agents,

resulting in their white appearance. It is the distinction between the reddish reflectance of the peritoneum and the broadband reflectance of the lesions that is used to visually identify metastases in conventional imaging. However, this is not the only optical property that may be exploited to distinguish between these two tissues: the cancer tissue composing the metastases is also significantly more scattering in the visible wavelengths than the peritoneum, with intraperitoneal tumor tissues typically exhibiting a reduced scattering coefficient of  $\sim 10\text{cm}^{-1}$  (Wang et al., 2005), while the coefficient associated with the peritoneum itself is roughly half of this value (Bashkatov et al., 2016). While the light scattering of tissue is not of great consequence in the case of conventional imaging, it is key in the realm of differentially polarized light.

Essentially, DPL imaging is a polarized imaging modality that which serves to separate the light scattered from the surface of a sample from light scattered from the interior. Thus, it is theorized that if DPL imaging were to be implemented in laparoscopy, the visibility of surface features of the peritoneum including the lesions would be improved, increasing the sensitivity with which clinicians can detect them. This would help achieve the reduction in the number of false negatives reported during patient exams and ensure relevant treatments are applied more often.

The potential of DPL imaging as a method of selectively resolving the surface features of tissue was recognized as early as 1997, when Demos and Alfano examined various forms of polarized imaging of biological tissues (Demos et al., 1997). They found that when imaging in the DPL modality, the surface detail of the sample (in this case, a human palm) was notably

improved. Following this, others began to exploit this phenomenon when conducting optical interrogation of tissue surfaces.

Gurjar et al. and Hunter et al. both conducted studies concerned with the light-scattering spectroscopy (LSS) signal from tissue epithelia (Gurjar et al., 2001; Hunter et al., 2006). This optical signal consists of the spectrum of light scattered from a tissue sample. Based on the distribution of this spectrum, information concerning the cellular morphology of the tissue may be determined, including data on the nuclear size, population density, and refractive index distributions of the cells under study. These parameters are functions of the pathological state of the epithelial cells, allowing the distinction between cancerous, pre-cancerous, or healthy cells by the sampling of this scattering spectrum. However, the signal from the surface epithelium is small compared with the diffuse signal from deeper within the tissue bulk, making the analysis of epithelium's LSS difficult. To address this, the authors applied the properties of DPL in their imaging systems to help isolate the signal received from the surface epithelium from that of the bulk tissue. This allowed for the precise examination of the LSS signal from the epithelium without interference from the tissue bulk signal.

Yaroslavsky et al. combined the polarized imaging of DPL with fluorescence to create a fluorescent imaging system which could limit the detected signal to the surface of the tissue sample (Yaroslavsky et al., 2004). They applied this system towards the improved visualization of surface-layer pathologies exhibited in nonmelanoma skin cancers. It was demonstrated that following the application of fluorophores preferentially retained by cancerous tissue, the basal cell carcinomas present on the epithelial surface could be delineated in polarized fluorescence imaging with detail superior to regular fluorescence as well as histopathology. Once again, this

approach takes advantage of DPL's ability to limit the signal to the surface layer of the sample, removing any background originating from deeper within the bulk. When examining surface pathologies like basal cell carcinomas, this serves to isolate the diseased tissue from the bulk in imaging, permitting a more detailed study of its features.

In addition to these implementations of DPL in microscopy, there are also several groups concerned with its use in endoscopy. Their endeavors draw a close parallel with our own in laparoscopy, thus it is necessary to explore the possibility of applying their designs to our clinical need while considering their work.

Consider first the DPL probe designed by Steve Jacques (Jacques, 2002) in figure 2 below:

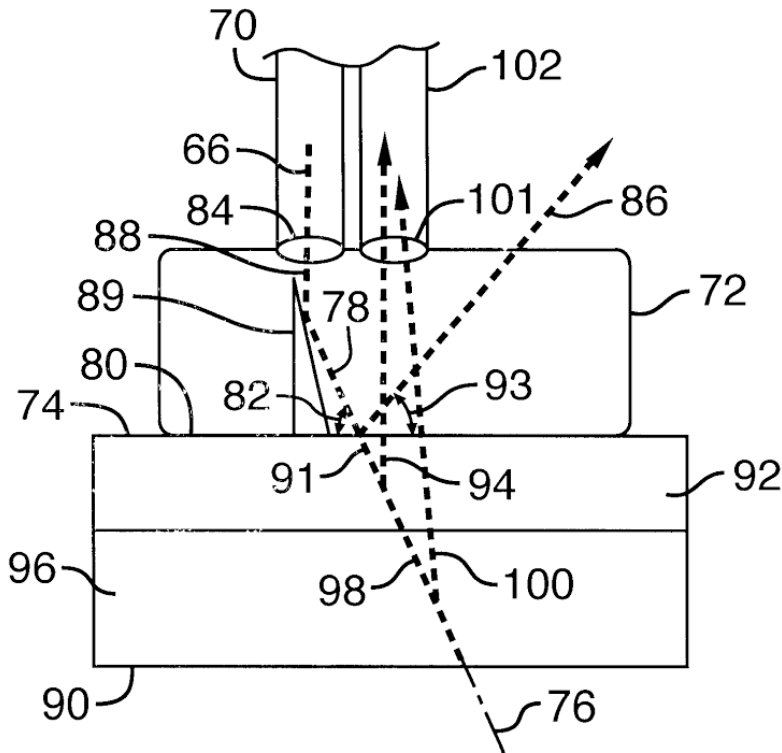


Figure 2: DPL endoscope probe design by Steve Jacques (Jacques, 2002).

Here, the polarized illumination (66) emerges from a polarization-maintaining fiber (70) and is deflected off a mirror (89) into an interface formed between the tissue surface (92) and the glass probe tip (72). The formation of this interface combined with the deflected angle of the illumination allows the reflection of specular reflectance (glare) (86) at an angle (93) that will not result in its collection by the detection fiber (102). The tissue reflectance (94, 93) is sampled by the detection fiber and analyzed by polarization optics upstream to generate parallel and perpendicular images for computing the DPL image.

For our purposes, the main issue with this proposed configuration is that it is designed to operate with the probe in physical contact with the interrogated tissue to create a flat glass-tissue interface (interface between 72 and 92) which reflects specular reflectance at an angle not sampled by the detection (101). This forces the working distance of the probe to a short, fixed



separation from the tissue surface. These characteristics make the device better suited for the close inspection of a small predetermined feature, but here to meet the clinical need it is desired that wide-field scanning be possible to rapidly screen a large surface (the peritoneum) at variable distances for the presence of lesions. This requires the probe to be out of contact with the tissue, and demands an optic which allows variable focus for accommodating different working distances. It should be noted that while Jacques's probe is lacking these requirements, taking the probe out of contact with the tissue to meet them sacrifices the ability to direct specular reflection away from the detection. However, this challenge may be addressed in other ways (glare detection, changing viewing angle) in the development of a contact-free probe.

Following Jacques, Myakov et al. created their own design for a polarized endoscopic probe (Myakov et al., 2002):

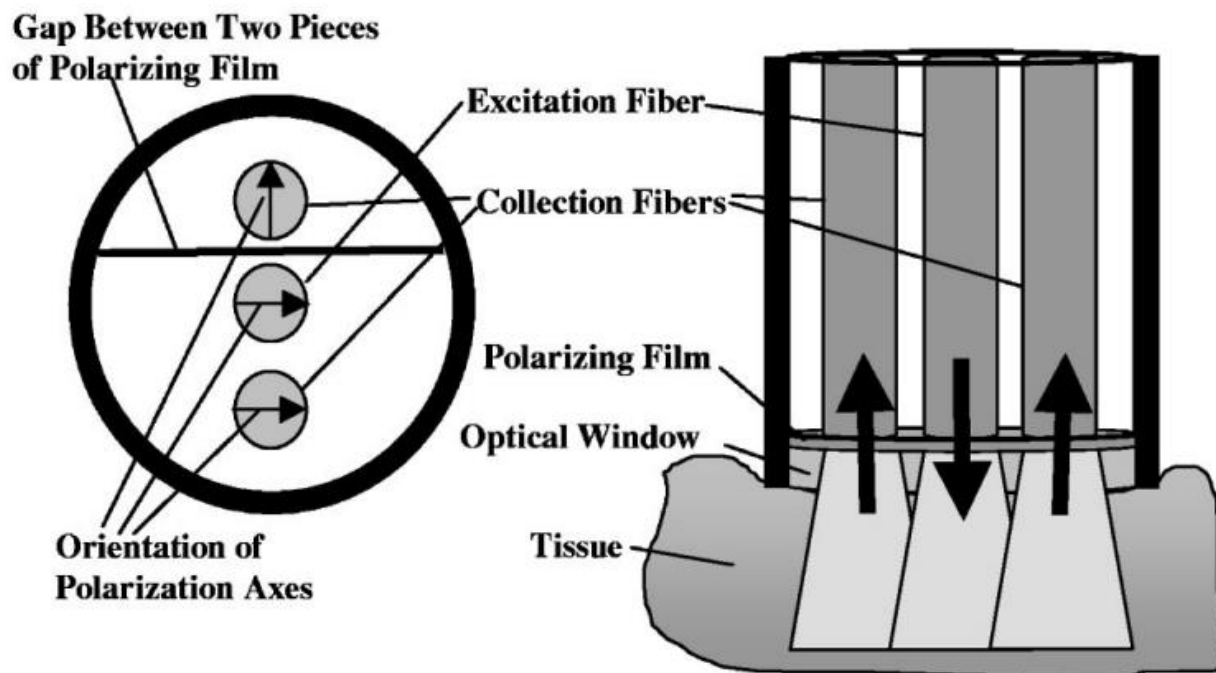


Figure 3: DPL endoscope probe design by the Myakov group (Myakov et al., 2002).

On the left side of figure 3 the front face of the distal end of the probe is presented. In this design, three optical fibers each carry the illumination, parallel, and perpendicular signals (middle, bottom, and top respectively) separately. Like Jacques' device, this probe is designed to operate in contact with the tissue surface, which once again conflicts with the need for wide-field examination. In addition to this, there is a greater conflict in the fact that this system does not provide a spatially resolved image of the sample, rather it collects only the net intensity of the reflectance incident on the end of the collection fibers. This would further cripple the screening capabilities of this device, requiring the scanning of the peritoneum surface with a probe area even smaller than that of Jacques', after which a mapping of the detected signal would have to be assembled to resolve the presence of any lesions. Thus, this would be an inappropriate implementation to address the clinical need.

More recently, Qi and Elson developed the design for a Mueller polarimetric endoscope (Qi et al., 2016) detailed in the figure 4 below:

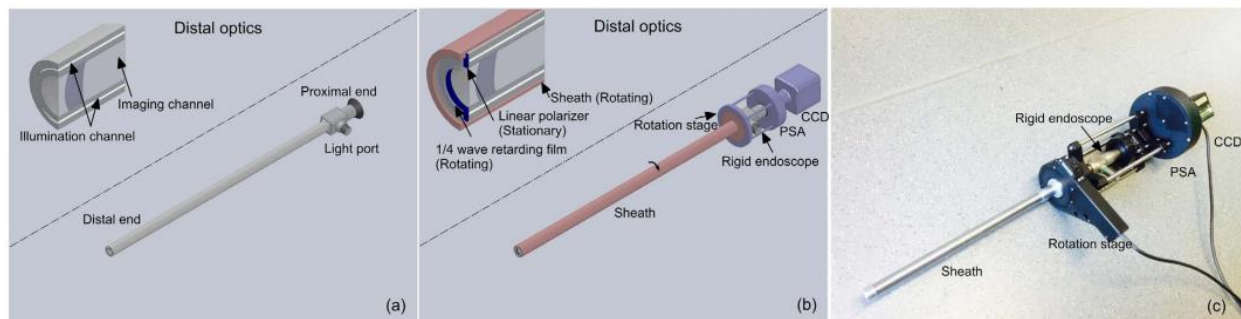


Figure 4: (a) A rigid endoscope consists of an imaging channel and an illumination channel. (b) The Mueller polarimetric endoscope consists of a stainless-steel sheath, a motorized rotation stage, a rigid endoscope, a polarization state analyzer (PSA) and a CCD image sensor. The part that rotates during acquisition is represented in red, and the stationary part is in purple. (c) A photo of the Mueller polarimetric endoscope (Qi et al., 2016).

This system measures with detail the transformation of the polarization state of the incident illumination as it is reflected off the imaged tissue. This transformation is quantified in the form of a Mueller matrix, hence the device name, and from it information regarding the

linear depolarization, circular depolarization, directional birefringence, optical rotation, and diattenuation may be derived if so desired (Ghosh et al., 2008).

Here, the derived property of linear depolarization contains the same information as DPL, effectively making this Mueller system DPL-capable. Further, unlike Jacques' and Myakov's designs, this one is capable of imaging in a wide field of view without the need to be in contact with the tissue surface. There is one major shortcoming however, in the form of the very long collection time the device requires for each image it takes due to the methods associated with the acquisition of a Mueller matrix:

To measure the complete Mueller matrix of some optically active sample (tissue in this case), it must be first separately illuminated with four forms of polarized light. These forms include linearly polarized light in the horizontal (0 degrees), vertical (90 degrees), and diagonal (45 degrees) directions, as well as circularly polarized light. Under each of these illuminations, the polarization state of the detected reflectance from the sample is examined. Combining the information from the reflectance polarization at each illumination, a Mueller matrix describing the properties of the sample may be computed. The optical systems responsible for illumination and detection in this case are referred to as the polarization state generator (PSG) and polarization state analyzer (PSA) respectively.

In Qi and Elson's design, the PSG consists of a  $\frac{1}{4}$  wave retarding film coupled to the rotating sheath (fig. 4b, red) combined with a fixed linear polarizer (inset fig. 4b, blue). To provide the four forms of polarized illumination required to compute the Mueller matrix, the retarding film must be oriented with respect to the linear polarizer at four separate angles (specifically, -45, 0, 30, and 60 degrees where the polarizer is oriented at 90 degrees). Thus, for

each Mueller image, the retarding film must rotate through four angular positions for the system to expose at four illuminations separately. This severely limits the frame rate of the image stream due to the need for multiple exposures and the operational limitations imposed on the rotation rate of the retarding film; currently the minimum time it takes to acquire a single image is 15 seconds. This limits the video frame rate of the device to far less than one frame per second, and requires that the probe be held still for the duration of each 15 second exposure. These limitations would make the screening of the peritoneum with this system quite onerous, as the clinician would have to be aware of the timing of each exposure period and hold the probe steady for its duration during the examination. In addition, if this device were to operate at its maximum frame rate, there would be negligible downtime between exposures and the probe could not be moved without affecting an exposure. Thus, the frame rate must be lower than this maximum if it is intended to move the probe at all between exposure periods while streaming images. The severely limited framerate and awkward operating requirements make this system impractical to use in the context of the clinical need.

Unfortunately, in each case these prior arts prove lacking in some aspect in the specific context of screening for peritoneal metastases. Thus, in addition to our investigation of DPL as a method of improving lesion visibility, we will also propose our own novel system design for its clinical implementation in Chapter 4.

### **Optical Description of DPL**

Here the fundamental optical phenomenon behind DPL imaging exploited by these biomedical imaging applications is detailed. Jacques et al. provide an elegant stochastic

description to this end: consider a tissue sample is illuminated with light linearly polarized in one direction, where the angular deviation of the reflectance polarization from the illumination polarization may be described by the following Gaussian distribution:

$$p(\theta) = \frac{1}{\sigma\sqrt{\pi/2}} e^{-\left(\frac{\theta^2}{2\sigma^2}\right)}$$

The variance  $\sigma$  for this distribution is equal to  $\chi\tau$ , the diffusivity multiplied by the optical path length (Jacques et al., 2000). Here, diffusivity ( $\chi$ ) is related to the average amount the light's angle of polarization changes with each scattering event, and the optical path length ( $\tau$ ) describes the total number of scattering events encountered by the light as it travels through the sample. Together, these parameters influence the variance of the polarization angle of the sample reflectance. As  $\chi$  or  $\tau$  increase, the polarization angle distribution of the signal spreads due to the larger number of scattering events, and the depolarization of the signal increases.

It can be expected that for some diffusivity, if the optical path is long enough, eventually the polarization of the light will become completely randomized due to the large variance  $\sigma$  in polarization angle resulting from large  $\tau$ . For biological tissues, it was found that this complete randomization of the incident polarization resulted from optical paths associated with tissue depths greater than ~200-300 microns (Jacques et al., 2000). Thus, light which penetrates to the bulk volume of the sample beyond this distance in the sample before exiting as reflectance becomes depolarized. Conversely, light that follow a shorter  $\tau$  (less than ~200-300 microns), undergoes fewer scattering events before exiting as reflectance and retains some degree of polarization parallel to that when it was first incident on the sample. The general relationship between optical path length and reflectance polarization is illustrated in the figure below:

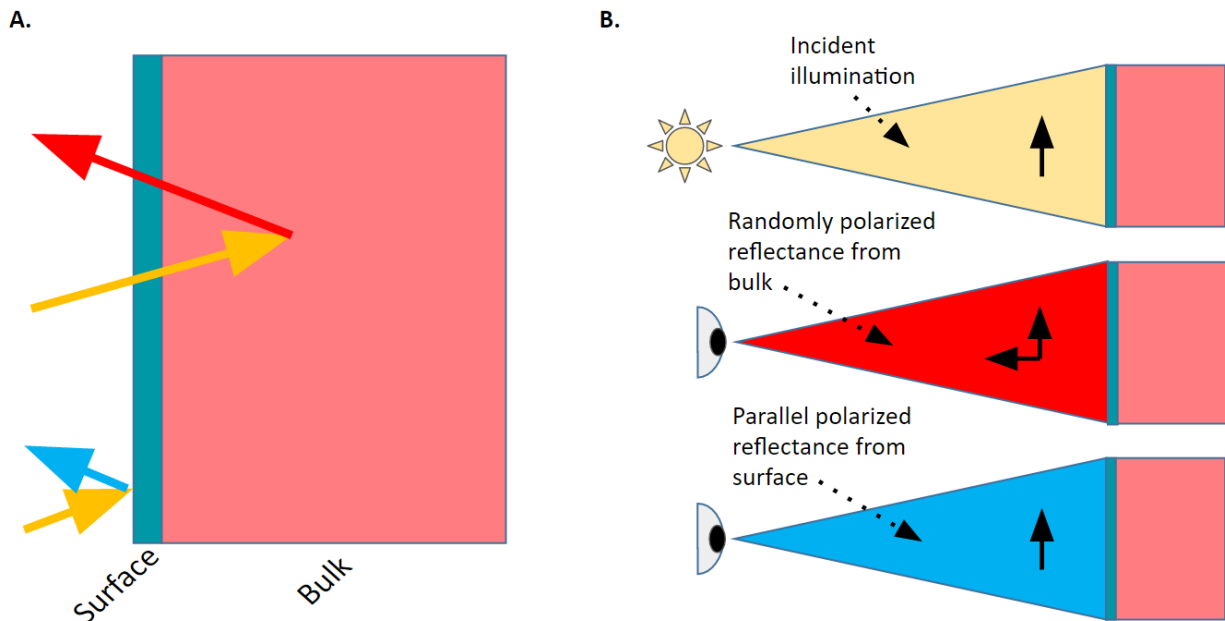


Figure 5: General behavior of the polarization of the reflectance from polarized illumination in bulk and surface regimes.

Figure 5a shows the scenario exhibited in DPL imaging where the sample is illuminated with linearly polarized light (yellow), and the reflectance of this illumination is received from both the surface (blue) and the bulk (red) of the sample. 5b presents the polarization states of the illumination, reflectance from the bulk, and reflectance from the surface. Reflectance originating from deeper within the sample follows a longer optical path and becomes randomly polarized. This state of random polarization is symbolized in 5b as the two perpendicular black arrows of equal length, indicating that the light is polarized equally in the directions parallel and perpendicular to the polarization of the incident illumination. In contrast, the surface reflectance retains the direction of the incident polarization, and is still completely polarized parallel to the illumination, as signified by the identical black arrows in both the illumination and surface reflectance signals.

The distinction between the polarization states of the surface and bulk signals is exploited in differentially polarized light imaging to remove the bulk signal, leaving only the surface

signal. To achieve this, the signal received from reflectance is examined through a linear polarizer (henceforth referred to as the analyzer) in two configurations. In the first of these configurations, the analyzer is oriented parallel to the illumination polarization, passing the surface signal, and half of the depolarized bulk signal, as detailed in figure 6a. Next, the analyzer is oriented perpendicular to the illumination polarization (6b), blocking the surface signal, while again passing half of the bulk signal.

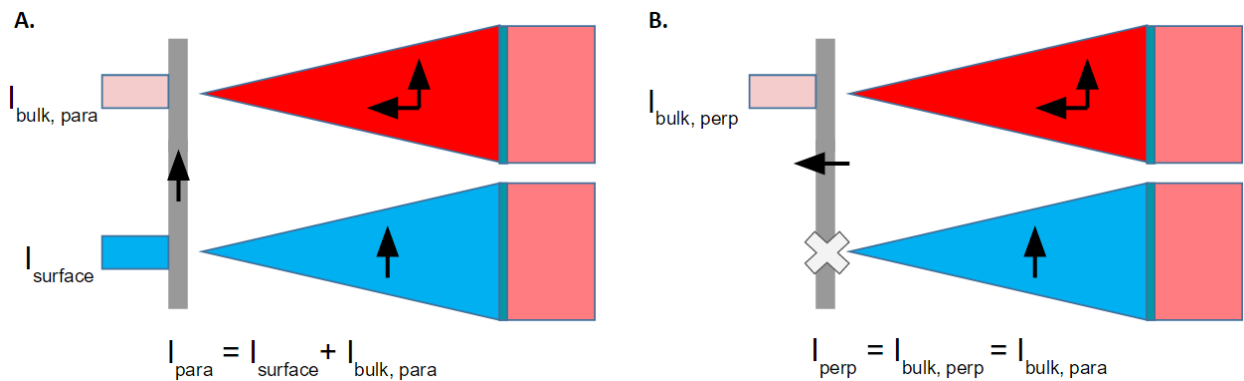


Figure 6: Analyzing the polarization of the reflectance signal to separate the bulk and surface reflectance.

Thus, the total intensity of the parallel-polarized reflectance,  $I_{\text{para}}$ , is the sum of the surface signal and half of the bulk signal, whereas the perpendicular polarized signal is composed only of half the bulk signal. With this, it is possible to separately image the sample in both parallel and perpendicular analyzer configurations. The perpendicular image may then be arithmetically subtracted from the parallel image to produce a difference image limited to signal received from the surface reflectance:

$$I_{\text{para}} = I_{\text{surface}} + I_{\text{bulk, para}}$$

$$I_{\text{para}} = I_{\text{surface}} + I_{\text{perp}}$$

$$I_{\text{para}} - I_{\text{perp}} = I_{\text{surface}}$$

Additionally, to generate an image representative of conventional depolarized imaging for comparison, the average of the parallel and perpendicular images may be taken to recover the entire signal independent of polarization.



## CHAPTER 2: TESTING THE CONCEPT

### Introduction

Given the theoretical relevance of DPL imaging to surface feature examination, data was sought to help verify this theory. In this chapter, the potential for this imaging technique to improve feature visibility is examined via a benchtop DPL system with various optical phantoms.

### Benchtop DPL Laparoscope Setup

The following experimental setup was utilized to acquire proof of concept DPL images:

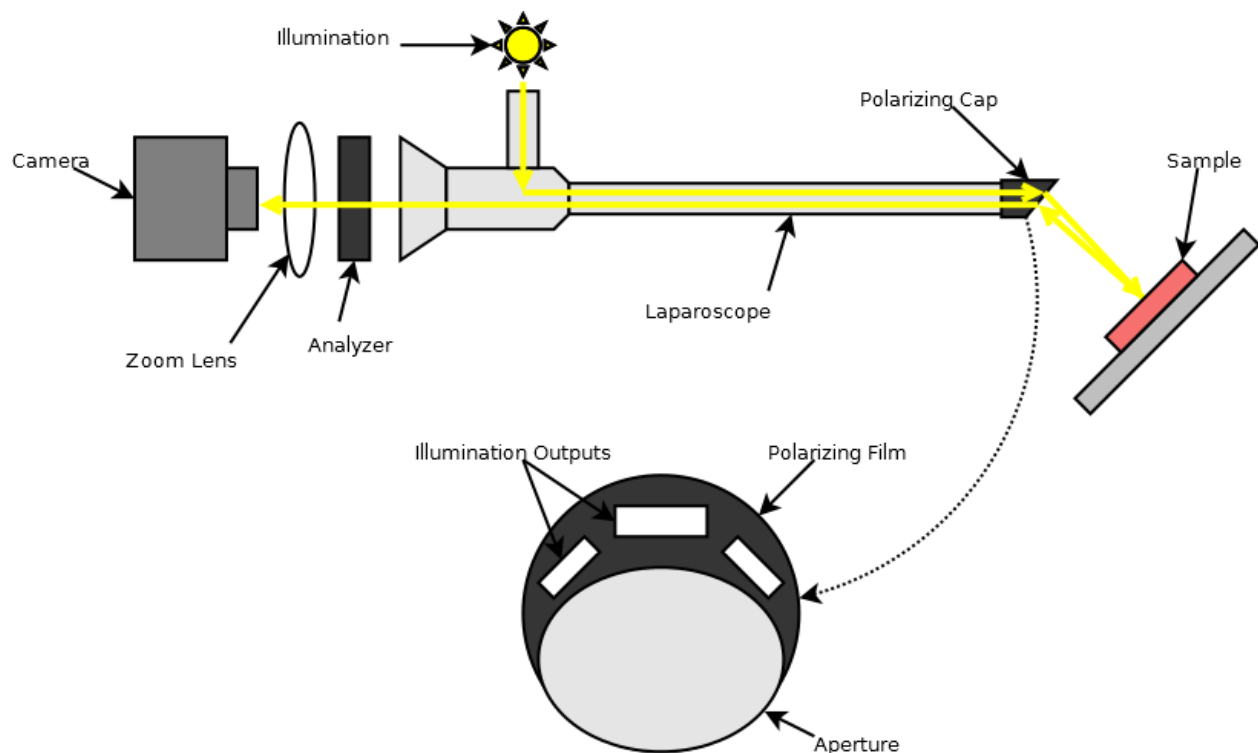


Figure 7: Experimental optical setup designed to implement DPL imaging.

Starting from the right, a specially designed polarizing cap (Eickhoff, 2014) is placed over the tip of a laparoscope. The inset details the front face of this cap, which is composed of a

crescent shaped polarizing film covering the illumination output of the laparoscope, while leaving the aperture below clear. This cap's addition serves to supply the linearly polarized illumination required for DPL imaging.

The laparoscope optic itself consists of a ~30cm long metal tube containing a fiber optic and a gradient index (GRIN) lens. The fiber optic delivers light from the illumination source to the sample at the distal (right) end, while the GRIN lens receives the reflectance image returned from the sample and relays it to the proximal (left) end. At this point, the signal passes a linear analyzer before being focused by a zoom lens onto a camera CCD.

To ensure the analyzer and illumination polarizations are oriented appropriately, a mirror image of the illumination is resolved by the system, and the analyzer is rotated while monitoring the live intensity average supplied by the imaging software. Once this intensity is minimized, the analyzer orientation is noted as perpendicular to the illumination. The parallel orientation is then denoted as the perpendicular orientation plus 90 degrees. The resulting images of the illumination at parallel (8a) and perpendicular (8b) analyzer orientations are depicted in the following figure:

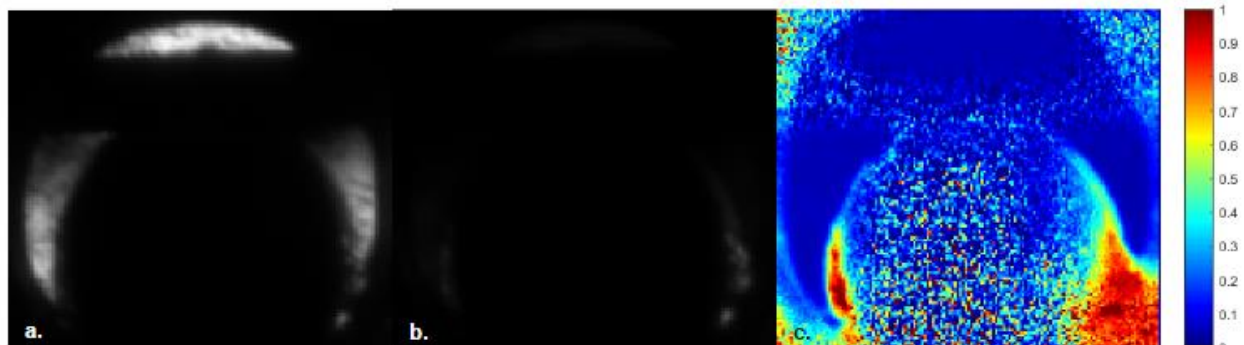


Figure 8: Mirror image of the laparoscope illumination at maximum intensity (a) and minimum intensity (b) corresponding to parallel and perpendicular analyzer orientations respectively. The ratio of the perpendicular intensity to the parallel intensity is displayed in c.

In 8c, the ratio of the perpendicular to the parallel image is calculated. Ideally, this ratio should be close to zero in the regions of illumination seen in 8a. For the most part, this is the case, and the ratio is  $<5\%$ . However, there is some amount of depolarized light leakage seen in the bottom edges of the illumination in 8b, which is confirmed by ratios in this region approaching 1 in 16c. To quantify the amount of depolarized leakage relative to the polarized illumination, the ratio of the average intensities of 8b and 8a was calculated, yielding a value of 9%. This indicates that 9% of the applied illumination is depolarized. The presence of depolarized light in the illumination does not necessarily compromise the DPL signal. The magnitude of the DPL signal is proportional to the magnitude of the polarized light signal, and is independent of any depolarized component, which will be removed in the image subtraction. The problem would arise where the illumination is composed overwhelmingly of depolarized light such that there is very low polarized illumination intensity. Here the detector would receive a correspondingly low DPL signal that may make visualizing the sample difficult. Fortunately, in this case,  $>90\%$  of the illumination intensity is polarized, ensuring a significant amount of polarized illumination is delivered for a given lamp power.

To acquire a DPL image, the analyzer is first oriented parallel to the illumination polarization and an image is collected by the camera. Then, the analyzer is oriented perpendicular to the illumination and a second image is collected. The signal of this second image is subtracted from that of the first via MATLAB (Appendix B-1) to produce the DPL image. For comparison, the conventional non-polarized image is reconstructed by taking the average of the parallel and perpendicular images.

## Imaging Results: Optical Phantoms

To verify the basic level of functionality in this system, a phantom was devised which possessed a feature and background that in theory should be very distinguishable in DPL imaging. The feature of the phantom was created from a drop of 5 $\mu$ m diameter polystyrene microbead solution (concentration 0.3% solids) dried into a plaque on a glass coverslip. The background upon which this coverslip was placed was a Spectralon white standard. Due to the highly diffuse scattering of this background, it was expected that the reflectance from the Spectralon would be randomly polarized, while the backscatter from the beads would retain more of the incident polarization. The results may be seen below:

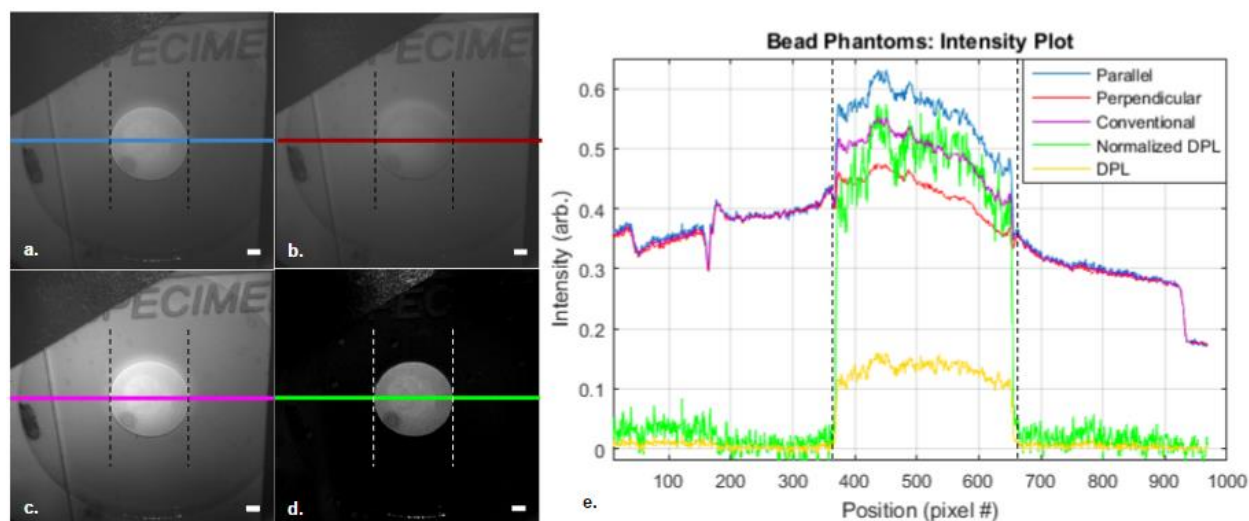


Figure 9: DPL imaging of a bead plaque-Spectralon phantom. Images for each polarization component (a parallel, b perpendicular) as well as their average and normalized difference (c and d respectively). In e, intensity as a function of position along the illustrated bisecting line is plotted, along with the raw DPL for comparison. Dashed lines indicate the boundary of the feature. 1mm scale.

To better understand the nature of the signals in images a-d, their intensities as a function of position along a slice (colored lines) was plotted in e. Directing attention first to the plots of the parallel (blue) and perpendicular (red) image components in e, it is evident that the bead plaque (flanked by dashed lines) retains some of the incident polarization in its reflectance,

resulting in a greater parallel intensity compared to perpendicular. This difference between the two signals is expressed in the DPL signal (yellow). Conversely, the Spectralon background (outside the dashed lines) presents virtually no difference in the parallel and perpendicular signals, thus has nearly zero DPL signal, due to its depolarized reflectance. In this way, the DPL image has its background brought to nearly zero while retaining signal from the feature. When the feature intensity in the DPL image is normalized to that of the feature intensity exhibited in the conventional image (c, purple plot of e), the visibility of the feature is significantly increased due to the reduction in background intensity.

Given the promising results encountered in the bead phantom, it was decided to continue towards more tissue-like samples. The next phantom fabricated consisted of a porcine muscle tissue (derived from the psoas major muscle) background with implanted silk scaffold to serve as the scattering feature. Fabrication involved the boring of four 3mm deep holes in the tissue with a 1mm diameter biopsy punch (white arrows in figure 10a-d). Of these holes, two had cylindrical silk scaffold fragments 1mm in diameter and 2mm in height inserted (solid white arrows). These silk scaffolds were fabricated via salt leaching protocol with 6% w/v silk solution as described by Nazarov et al. (Nazarov et al., 2004). The two remaining holes were left empty to act as controls (dotted white arrows).

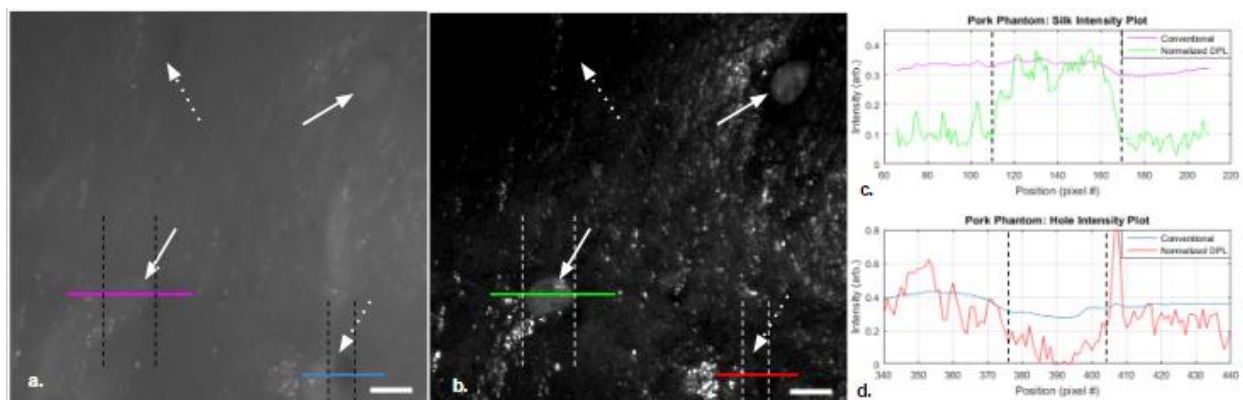


Figure 10: Conventional and DPL imaging of silk scaffold implants (solid white arrows) and empty control holes (dotted white arrows) in porcine muscle. (a) presents the conventional image, while b is DPL. Intensity plots around both the silk feature (c) and empty hole (d) were created for the conventional and DPL modes. The bounds of each feature are indicated by dashed lines. 1mm scale.

Once again, the visibility of the scattering feature (silk, solid white arrows) is improved in the DPL (10b) versus the conventional image (10a), while the visibility of the empty control holes (dashed white arrows) does not change appreciably. These observations are confirmed by the corresponding plots in c and d which indicate that the silk feature (flanked by dashed lines) exhibits increased signal to background in DPL (green) compared to conventional (purple), while this increase is not evident for the empty hole feature (also flanked in dashed lines) between DPL (red) and conventional (blue). The reduced width of the empty hole relative to the silk feature is due to its partial collapse since it has no feature to hold it open. These results suggest both that the presence of holes in the sample do not generate “false” DPL signal, and that DPL can increase the visibility of a scattering feature against a tissue background.

To model a feature more physiologically similar to a cellular tissue, the next phantom was designed with a cell-based feature instead of silk. In this case, a porcine muscle sample was once again bored with a small hole (flanked by dotted lines in figure 11a, b, d, and e) of the same size as those in the silk phantom. The sample was then imaged in conventional (11a) and DPL (d) modalities. Following this, a drop of highly concentrated (pelleted) lymphoma cancer cell

suspension was pipetted into the hole. The resulting phantom was imaged in conventional (11b) and DPL (e) modalities.

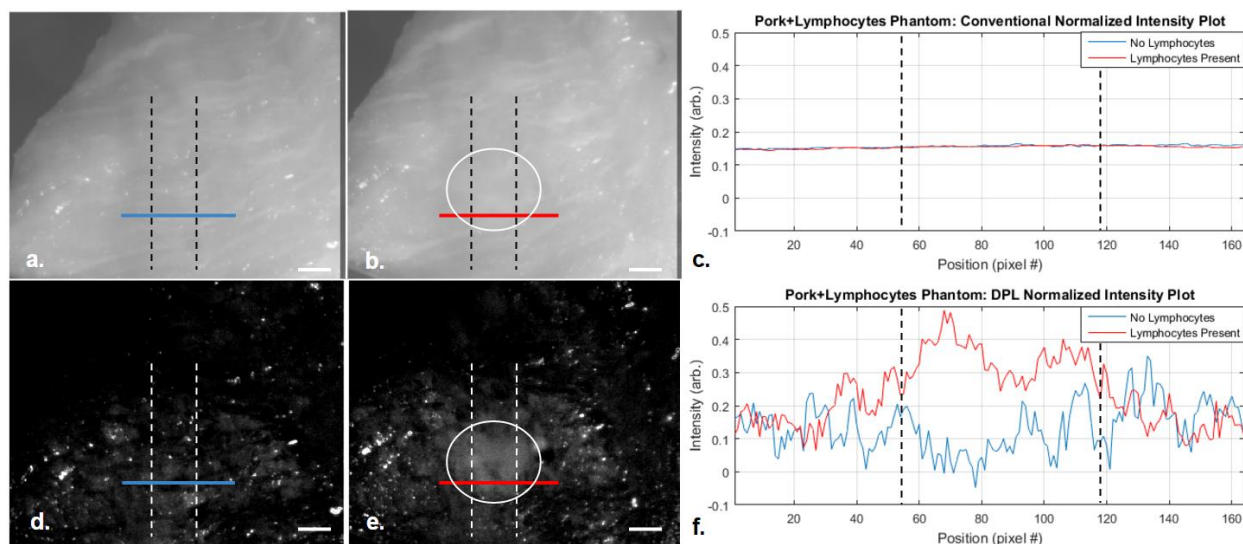


Figure 11: Conventional (a, b) and DPL (d, e) of porcine muscle with and without a lymphoma cell feature (circled in white) added. Intensity plots intersecting the location of the feature are presented in conventional (c) and DPL (f). The plot's intersection with the feature boundary positions are marked by the dashed lines. 1mm scale.

Studying the conventional imaging in figure 11a and b, the addition of the lymphoma cells (circled in white) is virtually undetectable. However, in the case of the DPL imaging in d and e, the lymphoma cells are visible as a cloudy feature surrounding the hole in the muscle. The large feature size (~2mm diameter cloud) compared to the hole (~1mm diameter) is due to the poor confinement of the lymphoma sample to the hole; essentially the sample formed a droplet that occupied the hole but also overflowed slightly onto the surrounding surface. Plots of the intensity over the feature location are provided for conventional (c) and DPL (f), with the points of intersection of the plot with the feature edge marked with dashed lines. From these data, it is demonstrated how the application of DPL imaging can provide distinction between the lymphocytes (f, red plot) and their background (blue) while they are nigh-invisible in the plot for the conventional modality (c).

At this point, a strong case for the proof of concept for the application of DPL is materializing. Namely, its ability to improve the visibility of a scattering feature placed on a background by measuring the polarized reflectance. This ability has been demonstrated in a variety of phantoms of differing degrees of comparison to the clinical pathology. The next logical step is to move towards a proof of principle which shows that DPL can maintain this observed degree of performance in a more clinically relevant model.



## CHAPTER 3: QUANTITATIVE VISUALIZATION OF CANCER LESIONS IN DPL IMAGING

### Introduction

As mentioned in the prior chapter, it is desired to examine a clinically relevant sample with a DPL system to establish a proof of principle. This chapter outlines how this was attempted, and the results encountered.

### DPL Apparatus

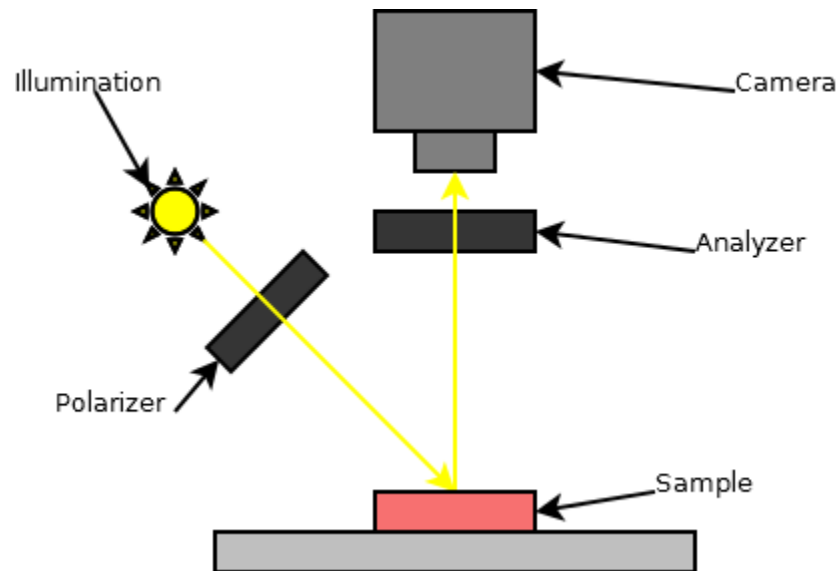
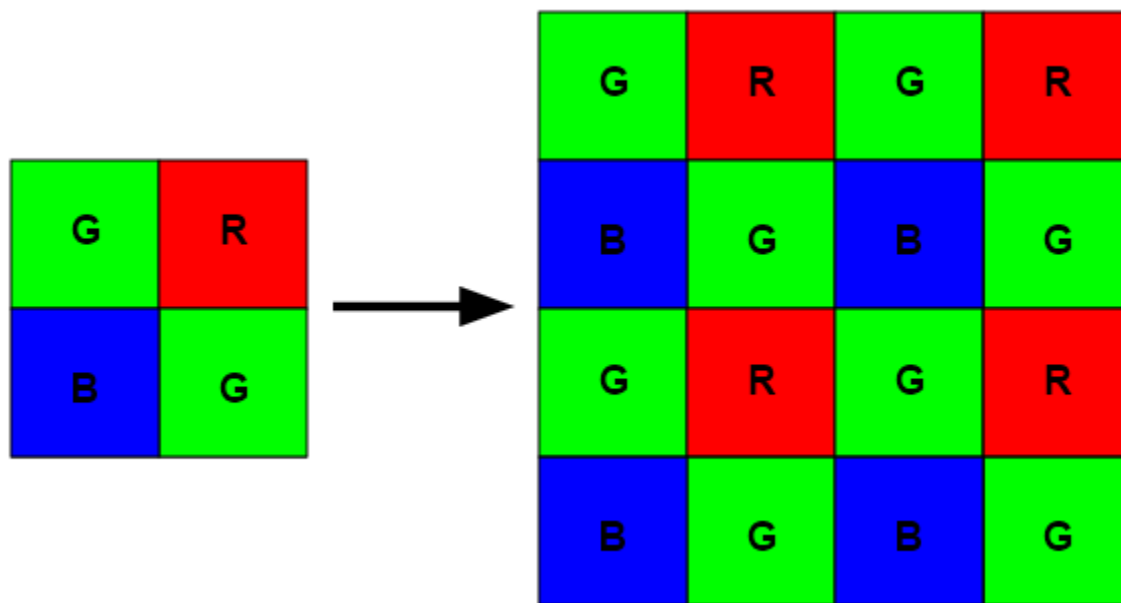


Figure 12: Schematic for the benchtop manual DPL imaging setup.

Figure 12 above depicts the simplified benchtop optical setup utilized for proof-of-principle imaging. Once again, a polarizer is positioned in front of the illumination to linearly polarize it, and an analyzer placed in front of the camera which may be oriented perpendicular or parallel to the illumination polarizer. This allows for the separate collection of the parallel and perpendicular components of the reflectance.

## Image Processing

The camera employed in the current device design is a RGB camera, as opposed to the monochrome camera applied in Chapter 2. The CCD arrays used by these types of cameras are covered by a great number of red, green, and blue color filters in an arrangement referred to as Bayer tiling (Bayer, 1976):



*Figure 13: The Bayer-tiled arrangement of RGB filters over the CCD array of a color camera.*

The basic tile element is shown on the left in figure 13, it is a mosaic of these tiles that forms the sensor array of the camera, analogous to the array on the right. The signal read from this array forms the raw Bayer-tiled image, which is then read by a color processing algorithm to produce the final image. Depending on the algorithm applied, the resulting image may be in RGB color or in monochrome. In the former case, for every pixel in the array, a red, green, and blue intensity value is extrapolated from neighboring color pixels and the pixel itself, creating an image with the same spatial resolution as the raw Bayer tile array, but where each pixel has a red, green, and blue value associated with it instead of just its filter's color. In the monochrome case,

a single intensity value is calculated for each pixel as the weighted average of the three-color intensities in the local area.

In either case, the intensity values for each pixel are recorded as 12bit unsigned integers by the camera. Following the collection of the parallel and perpendicular polarized images, each of the intensity values in the perpendicular image is subtracted from its corresponding value in the parallel image via MATLAB. This is straightforward for monochrome images, where corresponding subtracted pixels share the same position, and only slightly more complicated for RGB images. For RGB images, the raw Bayer-tiled image is recorded without any of the camera's color-processing algorithms applied to avoid any potential artifacts they may introduce when applied prior to subtraction (this mostly concerns automatically applied color correction like white balance). The images are then subtracted from one another in the same manner as in the monochrome case, after which MATLAB's `demosaic()` function is used to generate an RGB color image from the Bayer-tiled difference image via a simple linear color processing algorithm without correction. This functionality is also detailed in the MATLAB code of appendix B-1.

While not necessarily a vital feature of DPL imaging, the ability of the system to image in RGB is not simply a novelty, it does provide additional practical information beyond what is gleaned in monochrome. At the very least, it allows the system to meet the original capabilities of a conventional non-polarizing laparoscopes, which image in RGB color. However, in addition to this, it has been found that the low resolution spectral information provided by the three color channels can prove useful when trying to resolve lesions more clearly.

## Imaging Results

In an ovarian cancer patient, a biopsy was taken of the peritoneum and of the bulk tumor. In this case, there was no indication of metastases on the peritoneum. Thus, a metastasis model was assembled by placing a  $\sim 1\text{mm}^2$  excised portion of the tumor atop the peritoneum biopsy. This model was then imaged in DPL and non-polarized modalities, after which the lesion feature intensity in the DPL image was normalized to that in the non-polarized image. Below are the collected RGB images (figure 14a and e) along with the separated presentation of each of their color channels (b-c for DPL, f-g for non-polarized):

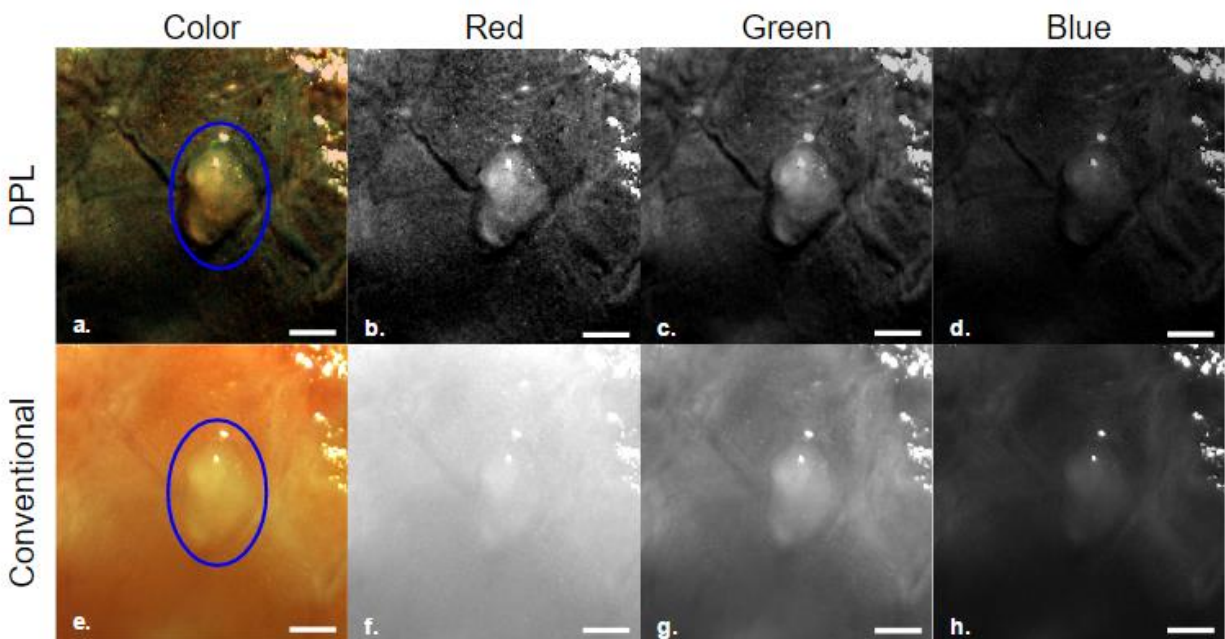


Figure 14: Imaging of a human ovarian tumor biopsy (circled in blue) placed atop a human peritoneum biopsy. 6a was taken in conventional non-polarized RGB, while 6e was imaged in DPL mode. The corresponding individual red, green, and blue channels are displayed alongside each image. 1mm scale.

When transitioning from conventional (fig. 14e-h) to DPL (a-d) imaging it is immediately apparent that there is some improvement to the visibility of the model lesion in all color channels. Looking at the pairs of images associated with each channel, some qualitative observations may be made. In each case, there appears to be some level of improvement in tumor

visibility when transitioning from the conventional to the DPL modality, as mentioned earlier. The improvement is most drastic in the red channel, and subtler in the green and blue channels. This observation is attributed to the fact that most the background signal is composed of red light due to the hemoglobin in the vasculature of the peritoneum. Thus, when this background signal is reduced via DPL imaging, the biggest effect is seen in the red channel. Another interesting aspect contained in the color channel information is the improvement in tumor contrast that is exhibited in conventional imaging depending on the selected channel. When comparing fig. 14f, g, and e, it appears that the visibility of the tumor is improved simply by viewing it through the blue or green channels without need for DPL imaging. Once again, this has to do with the background signal being mostly red light, while the tumor is white (red, green, and blue). Therefore, viewing the sample through the green or blue channels filters out the red signal from the background, while the tumor remains in the image thanks to having blue and green components to its signal. In this way, the visibility of the tumor is improved.

This phenomenon is somewhat analogous to the narrow band imaging (NBI) modality currently applied in endoscopy. NBI filters the illuminating light, limiting its spectra to a narrow bandwidth (usually around 30nm) centered around blue (415nm) or green (540nm) wavelengths. The high absorbance of these wavelengths by hemoglobin allows for the superior visualization of blood vessels on the surfaces of tissues by increasing their negative contrast against the background tissue from their absorbance of the illumination (Gono et al., 2003). There are other useful features of NBI, but this is the one we see also exploited in our system. In the same way that NBI illuminates with green and blue bands to reduce the signal from blood vessels and increase their contrast, we can do the same by instead examining the collection in

only the green and blue bands provided by the color filters on our Bayer-tiled sensor. In our case, reducing the signal from blood serves to darken the background, while in NBI it darkens the feature. In both cases this increases the contrast of the feature, only in NBI this is negative contrast, while in our application it is positive contrast.

## Imaging Analysis

DPL images appear to qualitatively improve the visualization of the tumor tissue, but it is desired that some more quantitative data be acquired in support of these observations. Thus, a parameter must be conceived which somehow captures the degree of visibility of the tumor against the peritoneum. It was decided that this “visibility” parameter is best described by the contrast of the feature (tumor) against its background (peritoneum). Contrast is defined here by the formula for Weber contrast:  $(\text{Signal} - \text{Background})/\text{Background}$  (Peli, 1990). To quantify this contrast, the following approach was applied:

First, two regions of interest (ROIs) are drawn on the sample image, shown encircled in orange and blue in the image contained in figure 15 below:

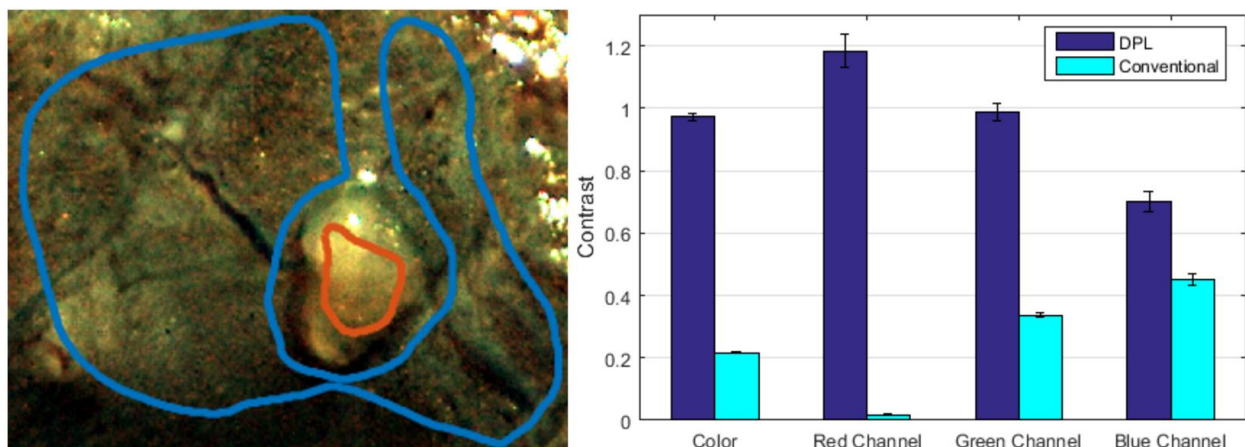


Figure 15: Quantifying the level of contrast between a feature (tumor tissue, orange ROI) and background (healthy peritoneum, blue ROI) for the sample exhibited in fig. 11. Values for contrast calculated on this basis are presented in the plot on the left for conventional and DPL modes in color and each individual RGB channel.

Here, one ROI defines the region the tumor biopsy occupies (orange), while the other defines the region of the background peritoneum the biopsy rests on (blue). The average intensity within the biopsy ROI serves as the value of the signal, while the average intensity within the peritoneum ROI excluding the biopsy ROI is taken as the value of the background. Note that in this case the ROIs are drawn to avoid glare spots, which would otherwise inflate the average value of each region regardless of the tissue composition; the glare signal is a function only of the sample surface angle, and is not dependent on the presence or absence of tumor tissue. The Weber contrast is then calculated for these signal and background values, yielding an estimate for the contrast of the biopsy against the peritoneum. The results for this value under various conditions may be seen in the plot in fig. 15. Note that the error bars in this plot are derived not from a sample of several biopsies as may be expected by default. Rather, these error bars represent the standard deviation of the contrast as propagated from the standard deviation from the mean signal and background values. They represent an estimate of the potential variance in the contrast based on the variance of the pixel intensity values within each ROI.

This plot helps confirm the qualitative trends in contrast observed in fig. 14. Once again, it may be seen that DPL provides a substantial improvement in contrast over conventional imaging, with the greatest difference in contrast exhibited in the red channel. As expected, it can also be seen that the contrast in the conventional color image may be improved by examining the green or blue channel separately.

With these results, it was decided that our case for DPL imaging would be furthered by setting up a tumor-negative control for comparison to the tumor model. This was intended to ensure that the signal produced by the tumor in the prior images is due to the difference in tissue

composition between tumor and peritoneum, not simply the physical presence of a tissue biopsy regardless of its type. To examine this scenario, another tumor-peritoneum model was set up as outlined previously, and following imaging of it (green channel displayed for best tumor visibility in fig 16a and b below), the tumor biopsy was removed and replaced with a biopsy of the peritoneum of the same dimensions. This was then imaged as well (fig. 16c and d):

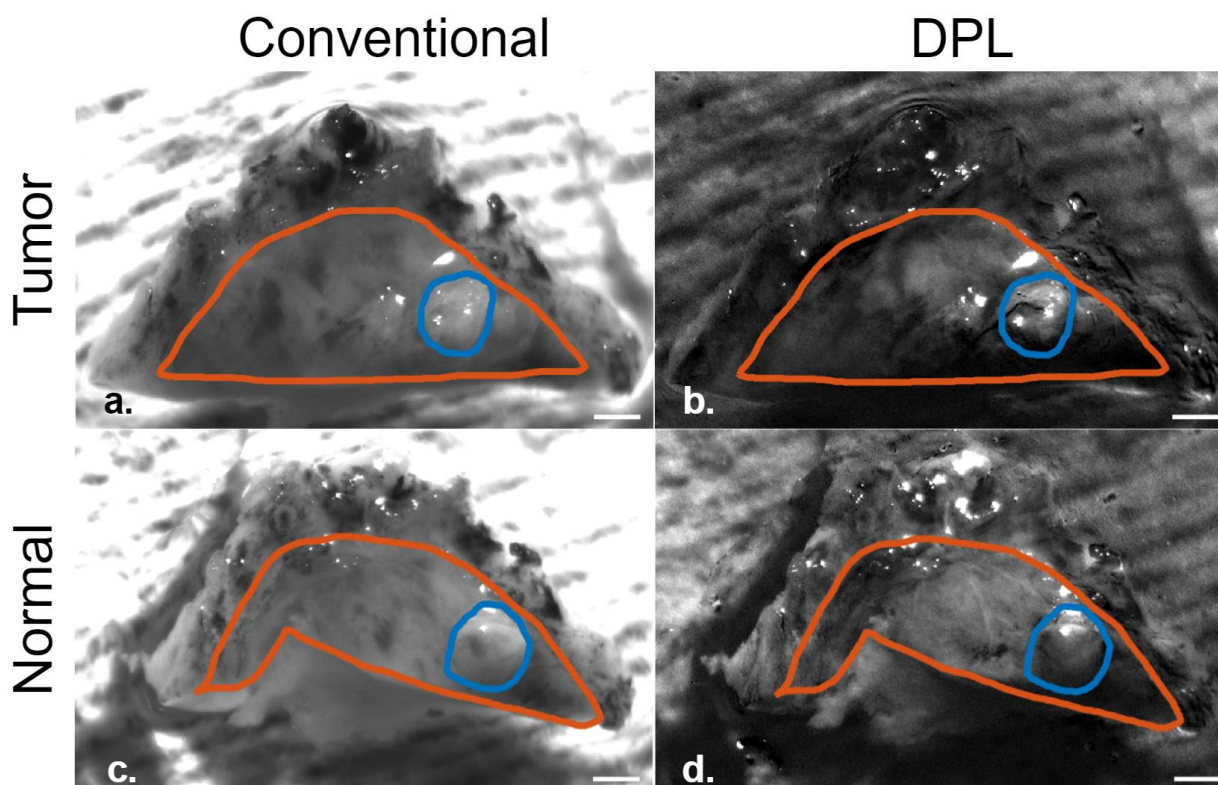


*Figure 16: Conventional and DPL imaging (green color channel) of both a tumor (a, b) and a normal peritoneum biopsy (c, d) placed on a peritoneum background. For each of these four images, the contrast of the biopsy feature (blue) against the background (orange) is measured in color and in each individual color channel. 1mm scale.*

However, before extracting contrast data from these images, there are some problems that must be addressed. First, glare is more prevalent, and more sophisticated measures are needed for removing its influence from the ROIs than simply drawing the ROIs around it. To address this automated detection and masking of the glare was applied in the image prior to contrast calculation. In this application, reference to an image “mask” refers to a two-dimensional array



of binary values (Booleans in our application, treated arithmetically as 0 and 1) with the same spatial resolution of the image it is associated with. Element-wise multiplication of an image with its mask results in the “masked” image. This resulting image has the same values of the original image at every pixel multiplied by a true value (1) in the mask. However, every pixel multiplied by a false value (0) is set to zero. Thus, the creation of a mask allows the selective suppression of a population of pixels in an image while leaving others alone. This may be applied to remove glare: given a mask associated with the glare pixels of an image is created, the image may be multiplied (hereafter referred to as masked) by the inversion of this mask to set glare pixels in the image to zero.

The generation of the glare mask is achieved by applying the Canny edge detection algorithm in MATLAB to outline sharp intensity spikes in the image characteristic of glare. An example of how distinct the difference between glare and tumor signal is detailed below:

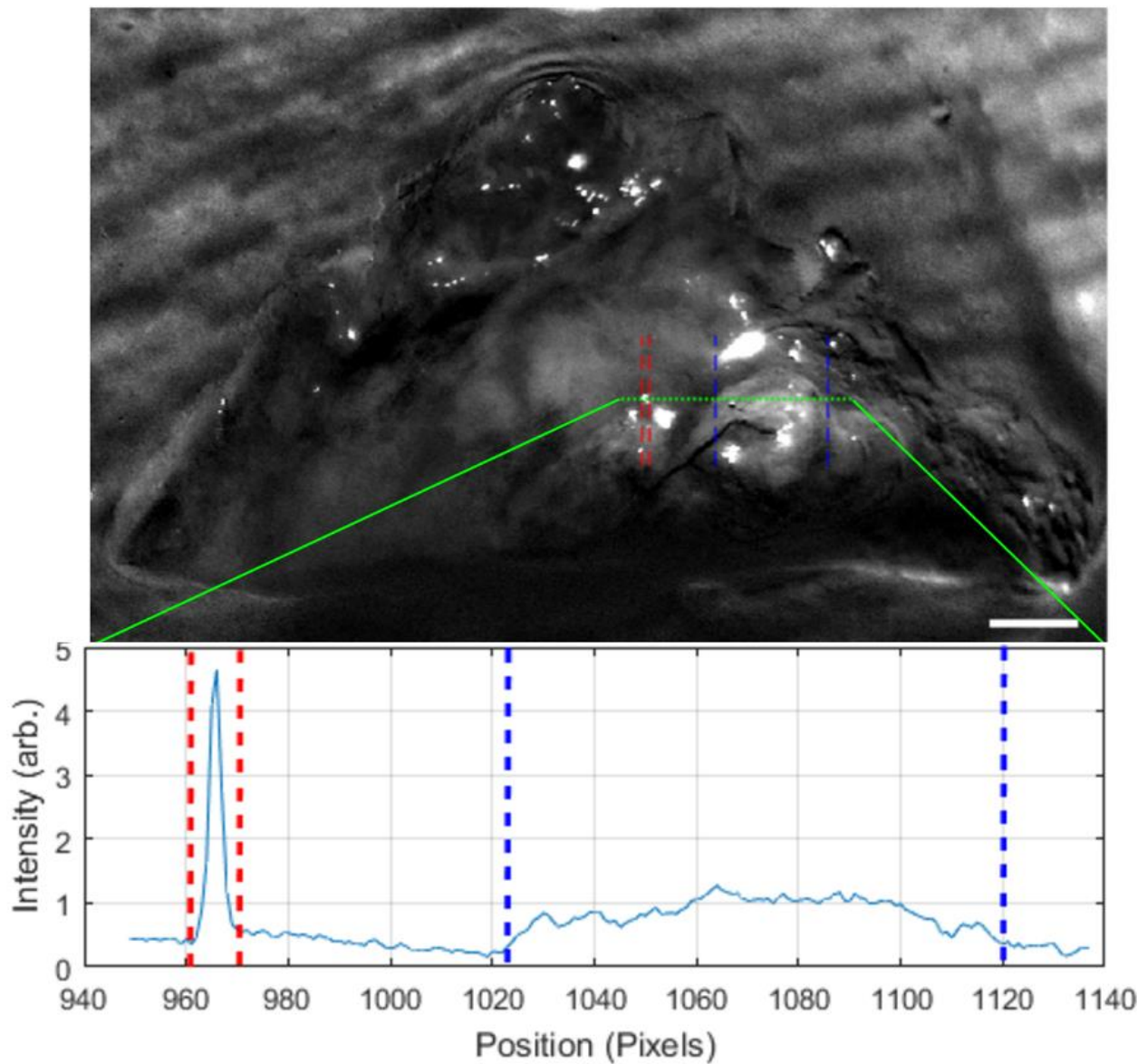


Figure 17: Comparison of glare signal versus tumor signal in the image from 8b. The signal intensity along the dotted green line is plotted below the image, with the dashed red line demarcating a glare spot, while the dashed blue lines flank the tumor signal. 1mm scale.

As the Canny algorithm analyzes the image, it identifies these steep gradients characteristic of glare (flanked by dashed red lines in fig. 17) and marks the edge of these gradients. The process by which the Canny algorithm achieves this is as follows: first, a smoothing filter (usually a Gaussian filter) is applied to smooth edges resulting from noise while leaving larger nonrandom features intact. The 2-D intensity gradient is then calculated for the

filtered image, generating an image of the intensity gradient. Each pixel in this image has a gradient vector associated with it described by a magnitude and an angular direction. For each vector, the angle value is rounded to the closest cardinal or semi-cardinal direction on one half of the compass (0, 45, 90, or 135 degrees). This is because for any one pixel, a gradient calculated between it and its 8 immediate neighbors can only have 8 possible directions. The other half of vector angles are not used because they describe the same edge direction (0 and 180 degrees, etc.) perpendicular to the vector. So far, the outlined process is integral to many other edge detection algorithms. Canny's innovation involved the further refinement of the detected edges thus far.

To start, the discovered edges are thinned to one pixel in width. This is achieved by selecting an edge pixel, then examining its neighbors that lie in a direction parallel to its gradient vector. Of this pixel and its neighbors, the gradient maximum among them is found and kept while the other pixels are discarded. The process is then repeated for the next pixel along the edge (perpendicular to the gradient). Once completed, a user defined upper and lower threshold is applied to the thinned edges. This essentially examines each remaining edge pixel, and if the magnitude of its gradient is above the upper threshold, the pixel is kept, and labeled a strong pixel. If it falls between the upper and lower threshold it is also kept, but is labeled a weak pixel. Lastly, if it is below the lower threshold, it is discarded entirely. The resulting population of weak pixels are then examined for their connection to a strong pixel. If a strong pixel is not connected to the pixel through a series of adjacent weak pixels, it is discarded. The final product is a precise detection of strong edges that are not interrupted if their gradient becomes weaker as one travels along the edge (Canny, 1986).

The resulting outlines of the glare traced by the Canny algorithm and the regions they enclose are converted to a mask for the glare present in the image which may then be applied to the image to remove the glare. The MATLAB implementation of this is detailed in appendix

This step was taken for two reasons: first, it automates the process of accounting for glare, helping to reduce potential bias introduced by the user trying to manually avoid the glare spots. Secondly, it allows for easier and more complete inclusion of the sample area within the ROIs as opposed to the limitations imposed by being forced to draw two simply connected curves around glare spots, which is more difficult in this image. In addition to masking glare, it was also desired to be able to draw the feature and background ROIs in an intersecting fashion, such that the feature ROI may be drawn inside the background ROI as seen in fig. 16, rather than the background ROI tracing around the feature ROI as in fig. 15. This would provide a better-tuned and more representative calculation of contrast, and was enabled by forming a mask for the feature ROI, and excluding the pixels within this mask from the population of pixels within the background ROI. With these additional image processing techniques in place, the contrast values for the images may be calculated from the masked feature (fig. 16, blue) and background (orange) ROIs:

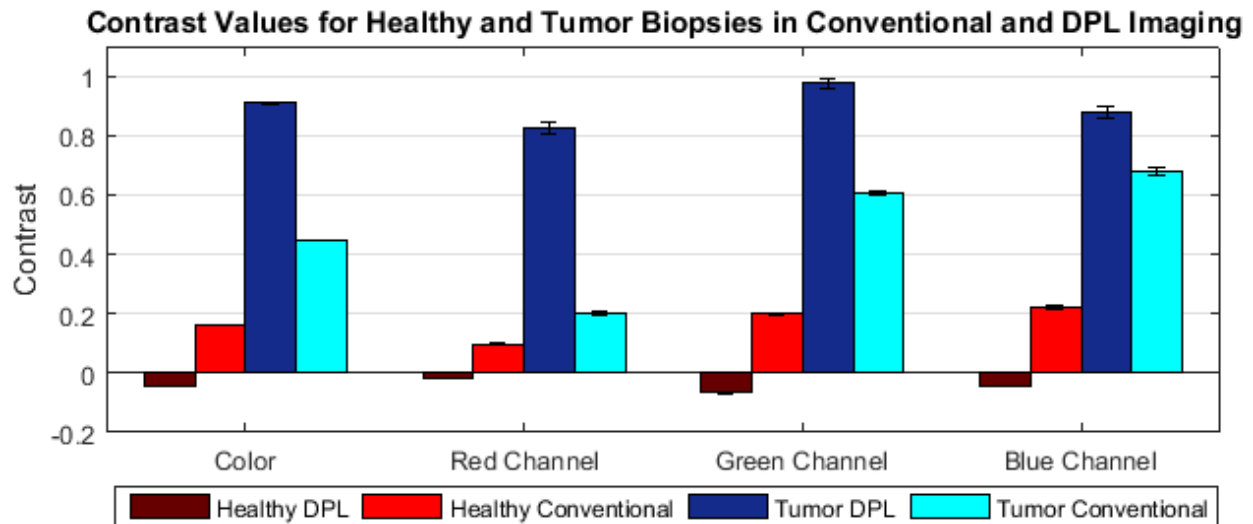


Figure 18: Plot of the contrast values of a healthy peritoneal biopsy and a tumor biopsy for a given RGB color channel and imaging modality. Values derived from the sample exhibited in fig. 8.

For the tumor biopsy (cold colors), the observed trends in the contrast values are consistent with those witnessed for the previous sample in fig. 15, with one notable exception: the highest absolute contrast is seen in the green channel instead of the red channel. It is suspected that this phenomenon is likely due to the heterogeneity of the tissues examined here, producing subtly different results for different samples of the same tissue. In addition to the tumor data, we now have a control to compare with. In the case of the healthy biopsy (hot colors), in the DPL modality the feature was nearly invisible, demonstrating the ability of DPL imaging to distinguish healthy and tumor tissue on an optically intrinsic basis, rather than simply by detecting the physical presence of a tissue biopsy regardless of its nature.

Taking the analysis of these samples one step further, a more general approach to contrast quantification is proposed for the case where the location of the feature is unknown, or it is desired that the contrast of two areas of the same image be compared. Here, since no feature ROI can be defined, the Weber contrast of each individual pixel intensity against the average intensity of the image (average of background ROI, including biopsy) is calculated and mapped. There is

a caveat when applying this method: it is most effective only when the area of the biopsy does not take up the majority of the image background. If it did, the average value of the image would not differ much from that of the biopsy, and pixels within the biopsy would be reported as low contrast. In these samples the biopsies take up a minority (~12% maximum) of the background area which has allowed the acquisition of meaningful results in these mappings:

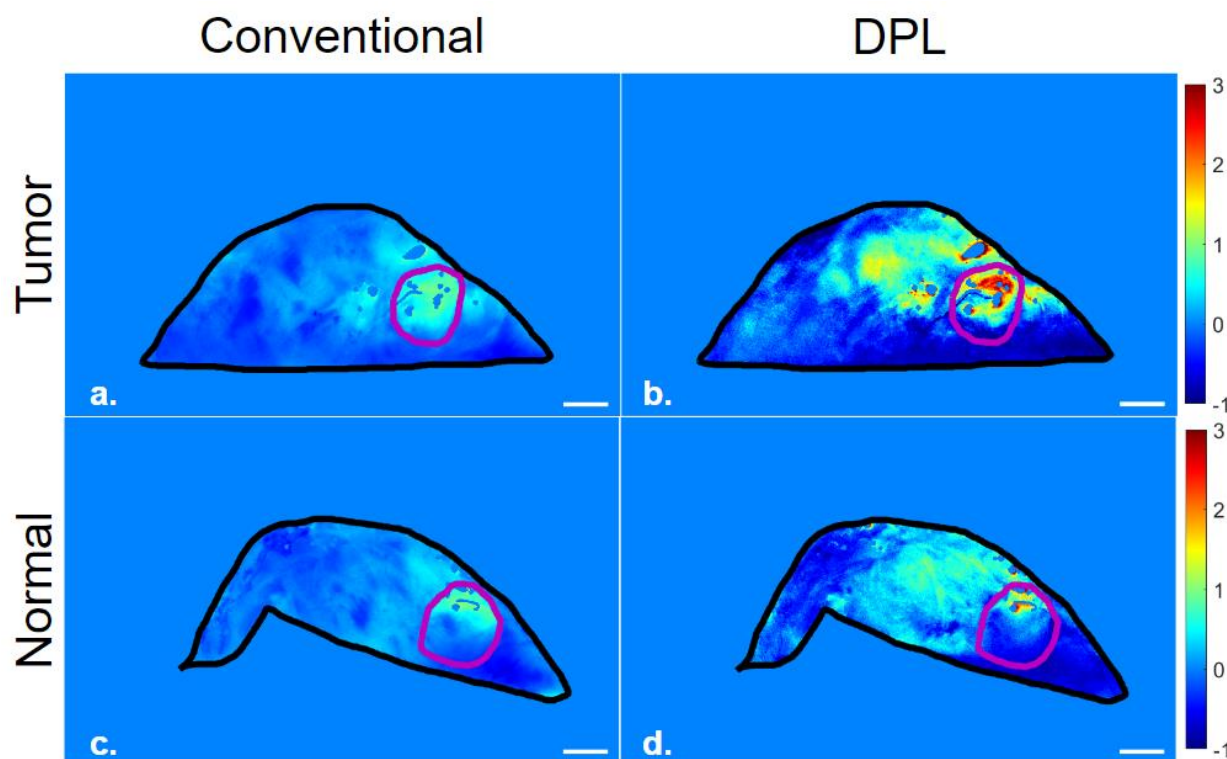


Figure 19: Mapping of the per-pixel contrast against the average image intensity for the same image set presented in fig. 13. 1mm scale.

This allows the observation of contrast against the image average as a function of position within the image, shown in fig. 19. It may be seen that the contrast of pixels associated with the tumor is maximized in DPL (purple ROI in 19b), while there is a lack of this increased contrast in the case of the healthy biopsy (purple ROI in d). Conversely, the contrast provided for the tumor in conventional imaging (purple ROI in a) is not much greater than that from a healthy biopsy (purple ROI in c) compared to DPL. While these data are supportive of DPL in tumor

visualization, they reveal a potential concern that must be addressed. Looking at fig. 19b, it may be seen that a large glare spot was masked above the tumor biopsy. Despite the masking, there remains a thin halo of contrast similar in magnitude to the contrast of the tumor. These halos cannot be effectively excluded by the Canny edge detection without removing the tumor signal, and are likewise too low in intensity to effectively threshold without drastically affecting the tumor image. While presence of glare in the tumor ROI is sparse enough that it may be concluded that majority of the contrast within it is due to the tumor itself and not these glare halos, there is still a question of how the presence of these halos skews the average intensities of ROIs used to calculate contrast here and in fig. 18. Fortunately, their contributions to the averaged ROI values has been found to be small. Consider the following glare-masked grayscale DPL images of the sample from fig. 19a-b:

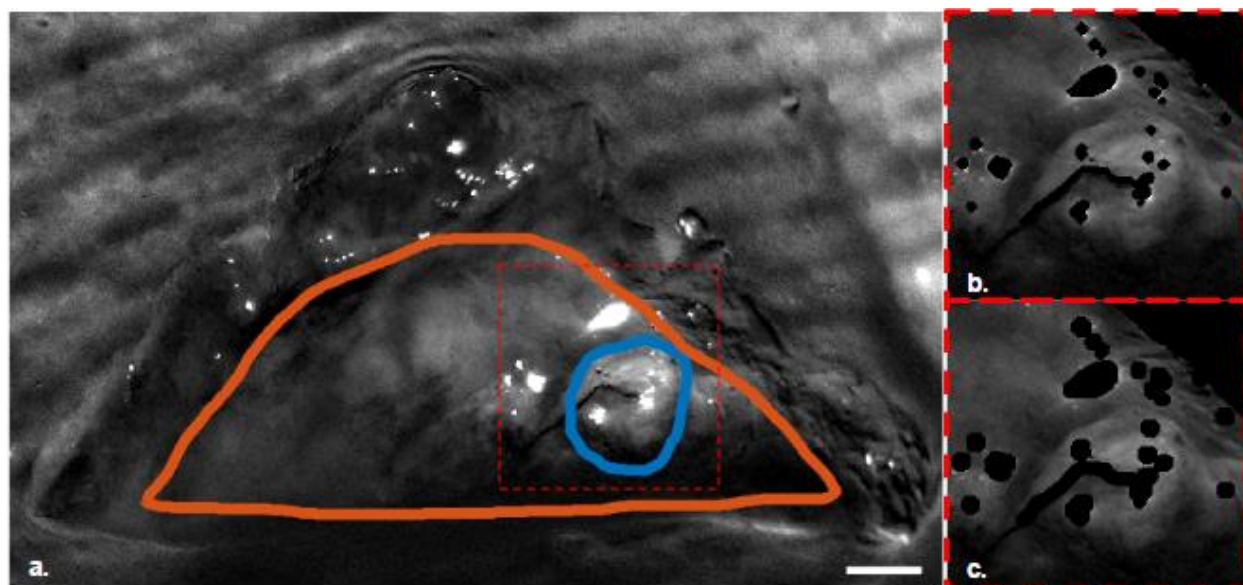


Figure 20: (a) Grayscale DPL image of a tumor biopsy placed on a peritoneum background (image from 13b). Insets b and c illustrate the standard and dilated glare masks applied to the image in a. 1mm scale.

Here the original glare mask may be seen in fig. 120b. This mask was dilated to suppress the glare halos mentioned earlier, the result of this is presented in 20c. For the background ROI,

halo suppression resulted in a 0.3% decrease in the mean intensity of the ROI, while the mean feature intensity decreased by 0.7%. This would propagate a 0.8% decrease in the calculated contrast between the two ROIs. Thus, the effect of these halos is neglected in favor of retaining a more complete image without unnecessary masking.



## CHAPTER 4: IMPLEMENTING DPL IMAGING IN A CLINICAL SETTING

### Introduction

At this point, it is evident that DPL imaging has the potential to improve peritoneal cancer lesion visibility, however this progress is meaningless without a means of implementation in the clinic. It is not possible to effectively apply the manually operated benchtop setup outlined earlier at the video rates desired to examine the peritoneum of patients in surgery. This chapter is intended to address this problem, and details the transition from a laboratory to clinical setting for this imaging modality.

### Device Design

In chapter 1 we exhausted any potential pre-existing DPL-capable endoscope systems well-suited to peritoneal screening, demonstrating the necessity of proposing a novel design. It was decided that the most efficient form of this design would be a modified version of the laparoscopic system currently applied for peritoneal metastasis screening. Below is a simplified schematic for a typical unmodified clinical laparoscope:

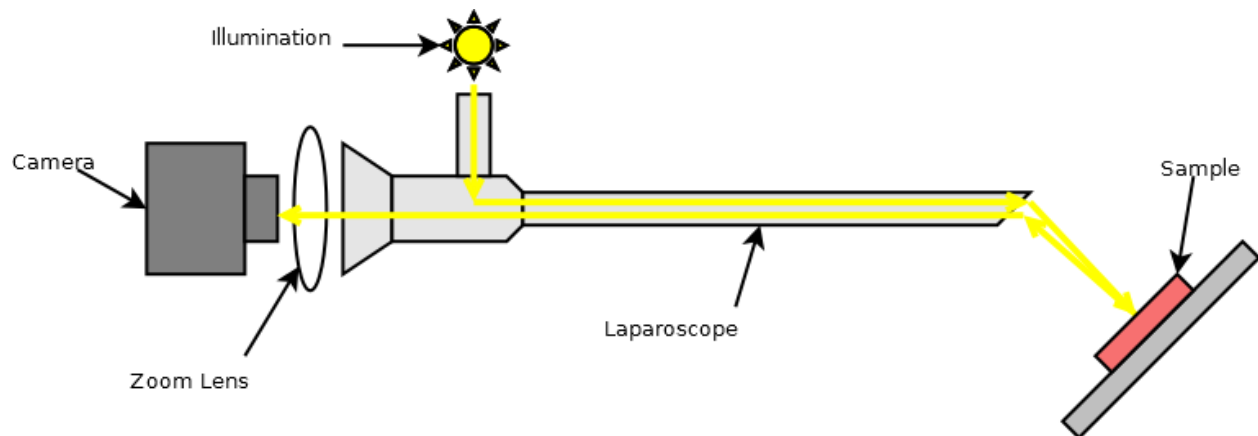


Figure 21: Simplified diagram of a clinical laparoscope.

To enable DPL imaging in this device, there are two main modifications that must be made to the optical train. First, a linear polarizer must be inserted such that the illumination is linearly polarized. Second, a variable analyzer must be introduced such that the polarization components of the reflectance both parallel and perpendicular to the illumination polarization may be detected separately.

The modifications applied here to support this functionality are outlined in figure 22 below, with the three added components in blue:

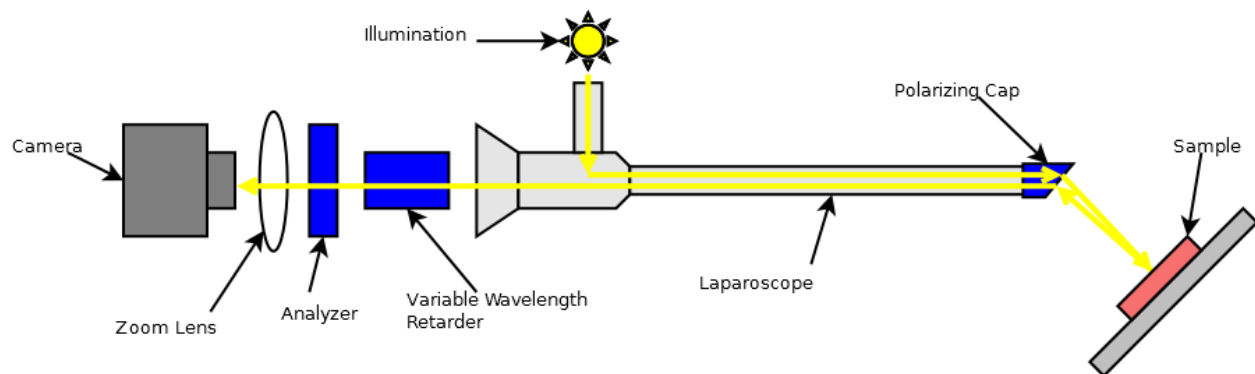


Figure 22: Modified laparoscope setup designed to implement DPL imaging.

As the collected reflectance travels to the left towards the camera, it is incident on two elements, a voltage-controlled variable wavelength retarder (Thorlabs LCC1111T-A), and a second linear polarizer (analyzer). The analyzer may be oriented parallel or perpendicular to the cap polarizer, in this case it is perpendicular. The variable wavelength retarder is oriented with the slow axis 45 degrees offset from the analyzer's polarization angle. In this way, when the retarder is set to zero retardance (effectively making the retarder invisible to the incoming signal) the camera sees the polarization of the image perpendicular to the illumination. If the wavelength retarder is set to half-wavelength retardance, the parallel and perpendicular components of the reflectance polarization are rotated 90 degrees. Now the camera sees the parallel component

through the analyzer since this component has been rotated into alignment, while the perpendicular component has been rotated 90 degrees out of alignment, extinguishing its signal as it passes the analyzer. In this way, depending on the retardance setting, either a parallel or perpendicular polarization image may be focused onto the detector via a zoom lens (computer® M3Z1228C-MP varifocal zoom lens). Once an image for each polarization is acquired, they may be subtracted as described earlier to yield the DPL image. The camera used here is a Point Grey model BFLY-PGE-23S2C-CS, which is a 12 bit-per-pixel camera with RGB color and monochrome imaging capability. This camera's CCD has a greater intensity resolution (12-bit) than that typically applied in laparoscopes (8-bit). This substitution concerning sensitivity was made because the DPL signal is several times weaker than the total reflectance. Thus, to effectively resolve this signal in detail a greater intensity resolution is required than that typically applied in regular endoscopic reflectance imaging.

### **Device Operation**

First, a mirror image of the illumination is resolved, and the analyzer is aligned perpendicular to the illumination polarization via the same methods detailed in Chapter 2. Following this, the variable wavelength retarder is placed in position and set to approximately half-wavelength retardance ( $\sim 1.4V$ ). The fast axis of the retarder is then rotated relative to the analyzer. Like the calibration of the analyzer, once the angular position of the retarder is found where the average image intensity is at an extremum (maximized in this case, the fast axis should be 45 degrees offset from the analyzer angle at this point), the retarder is fixed at this position.

Next, the optimal zero and half-wavelength retarding voltages of the retarder are determined. Examining the performance data for the retarder below:

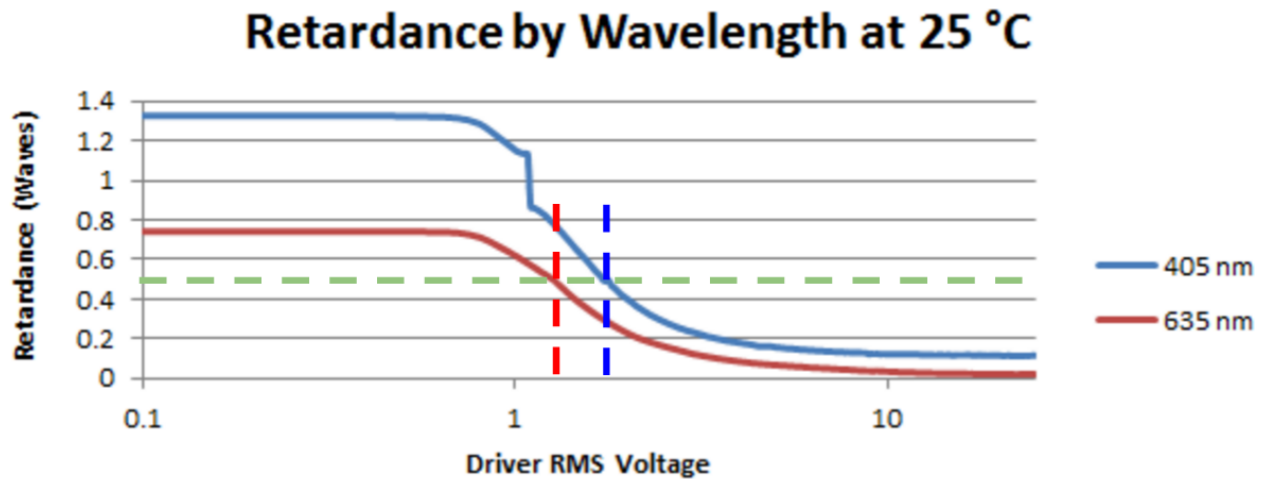


Figure 23: Plot illustrating the dependence of the retardance on light wavelength and applied voltage for the wavelength retarder model used here (Thorlabs 2017).

Provided by the manufacturer, this plot indicates that the retardance may be driven to near zero with the application of a high voltage, with subtle retardance variation with wavelength. This establishes the zero retardance voltage at the maximum operating voltage, 25V. The dashed green line marks the second target retardance at half-wavelength. The voltage required to enforce this retardance varies more with wavelength, ranging from 1.3 (red dashed line) to 1.7V (blue dashed line) over the range of wavelengths 405-635nm.

To determine the optimal half-wavelength retardance voltage for the range of possible detected wavelengths emitted by the illumination, the following experimental setup is applied:

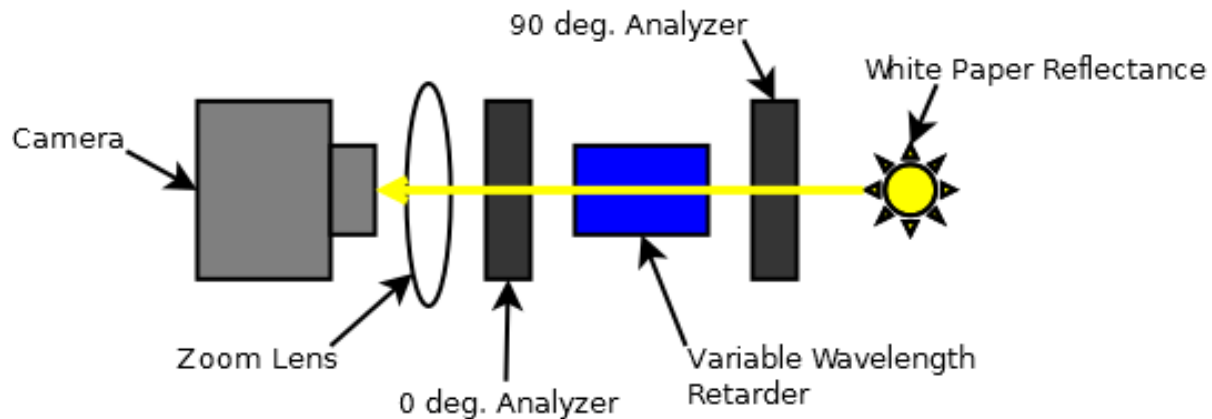


Figure 24: Diagram of the experimental setup for determining the optimal half-wave retarding voltage.

Here, if the wavelength retarder were not present, the signal read by the camera from the illuminated paper would be extinguished by its passage through the crossed analyzers. Placing the retarder back between the polarizers with its slow axis oriented 45 degrees from the analyzer axes, as the voltage of the retarder is varied, the polarized light incoming from the right analyzer will have the component of its polarization parallel to the slow axis of the retarder phase shifted relative to the perpendicular component. As the voltage is varied, this phase shift approaches 180 degrees, or half-wavelength retardance, and the signal received by the camera will approach a maximum as the polarization of the light from the 90-degree analyzer is rotated into alignment with the 0-degree analyzer. Because the half-retardance voltage is dependent on wavelength, there will be a different voltage for the signal maximum in each color channel. However, there will be a single voltage associated with the maximum for the intensity averaged across all color channels, it is this voltage that is sought as an approximation in place of custom voltages for each color channel. To find the value of this singular voltage, a series of raw Bayer-tiled images was acquired while incrementing the voltage of the retarder. The average intensity of each of these images was computed and plotted against the applied voltage to find the maximum:

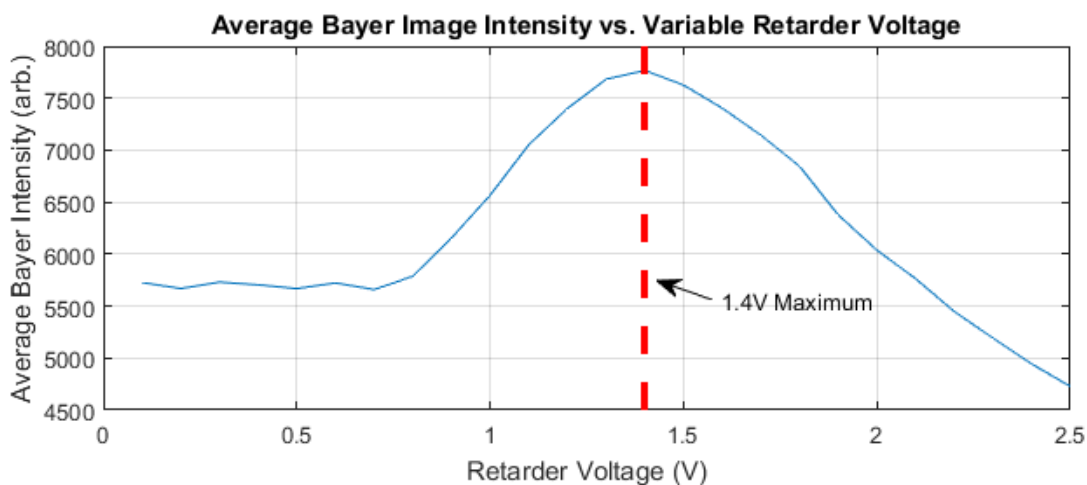


Figure 25: Plot of the average intensity for the raw Bayer-tiled images of a white standard at various retarder voltages. The maximum of the plot is indicated by the dashed red line at 1.4V.

These data indicate the optimum voltage for this setup is 1.4V. With this, the two operating voltages of the retarder are established: 25V for zero retardance, and 1.4V for half-wavelength retardance. Below are a pair of test images (converted to grayscale) taken at each of these voltages with the setup described by figure 24:

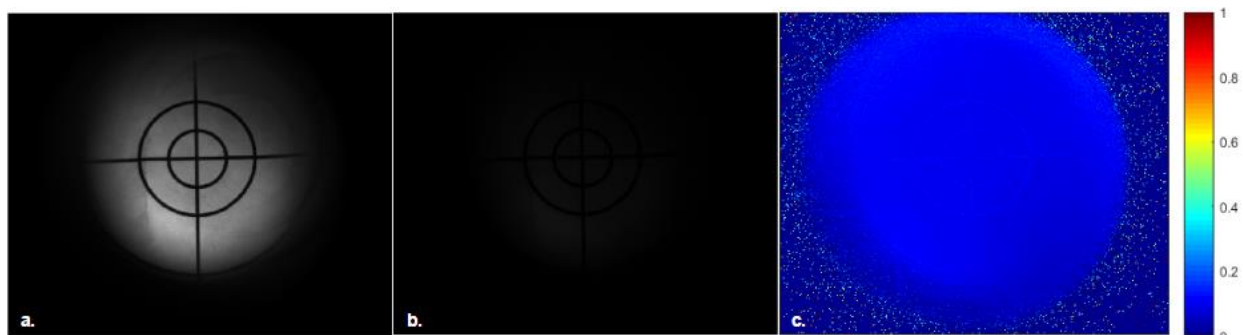


Figure 26: Imaging results collected from the setup in figure 24 for the half-wave retarding voltage (a, 1.4V) and zero retarding voltage (b, 25V). The ratio of b to a is displayed in c.

Given perfect retardance of all wavelengths at each voltage, the ratio of fig. 26b to 26a should be zero within the FOV (field of view). Due to the wavelength dependencies of the retarder detailed previously in figure 23, this ideal performance is not exhibited, but it is close, with the intensity of 26b less than 10% of that in 26a for much of the FOV. The implications of imperfect retardance in this system will be examined in greater detail in the following section.

Once all of these optical elements are calibrated appropriately, the camera is signaled to start capturing images by a software program utilizing the camera and retarder APIs (application program interfaces, see appendix C for details). The program essentially queries the camera frame rate, then sets the retarder voltage controller to switch between its two operating voltages at half this frame rate. After exposing the first image, the voltage controller is triggered to begin modulating between the two voltages, syncing the switching voltage with the data reading period following the exposure of each frame. This process is detailed in the figure below:

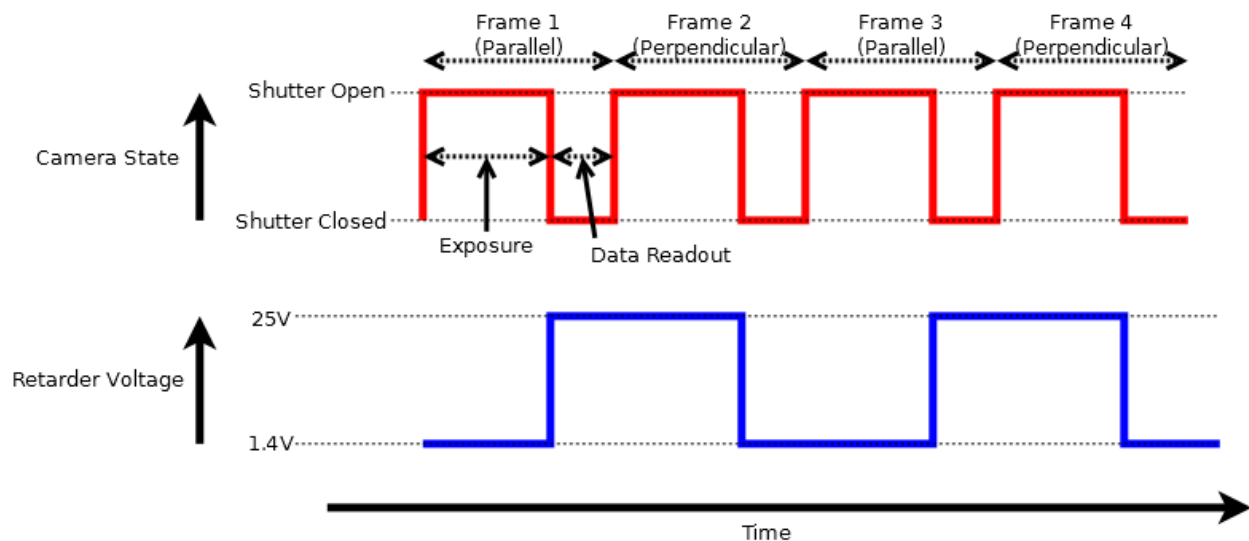


Figure 27: Time course for the operation of the camera shutter in conjunction with the wavelength retarder.

This results in the recording of a series of images of which the first is exposed during the collection of the parallel polarized reflectance, the second during the perpendicular, and so forth alternating in this way at the camera's frame rate. For every pair of polarized images, the DPL image is computed from them following data readout and appended to a vector of images. After the number of specified frames is exposed and appended, this image vector is converted to AVI video format for viewing. The current state of this controller requires further refinement before implementation, details concerning this will be provided as future directions in Chapter 5.

## Design Challenges

While the design proposed here is certainly sound in an ideal case, there are a few polarization properties intrinsic to certain components that have the potential to complicate its functionality. We have already briefly touched on one of these complications, that is the retarder's wavelength dependence, but there are some other additional sources of error that must be accounted for.

Before addressing these error sources, it is useful to become familiar with some tools that help describe polarization states and effects. The tool in this case is called Mueller calculus, the concept of which was briefly touched upon in the examination of the Mueller endoscope of Qi and Elson in Chapter 1. This is a method by which the polarization state of light is described by a four-element vector called the Stokes vector, and the transformations applied to the light polarization by optical elements is quantified by a 4x4 matrix called the Mueller matrix.

For a given beam of light of arbitrary polarization, the Stokes vector takes the following form:

$\begin{bmatrix} I \\ Q \\ U \\ V \end{bmatrix}$ , where I is the total intensity of the beam, Q is the intensity of linear polarization in the

horizontal (oriented 0 degrees, positive Q) and vertical (oriented 90 degrees, negative Q), U is the intensity of linear polarization in the diagonal direction (45, positive U, and 135 degrees, negative U) and V is the intensity of circular polarization (positive V for right circular, negative for left).

In the context of DPL imaging, there are two components of polarization we are concerned with in the collected signal. First is a completely linearly polarized component in the



vertical direction of intensity B retaining the polarization of the illumination, described by the

Stokes vector  $\begin{bmatrix} B \\ -B \\ 0 \\ 0 \end{bmatrix}$ . It is this intensity that is isolated in the DPL modality. The elements of this

vector may be interpreted as follows: all the total intensity of this component ( $I = B$ ) is linearly polarized in the vertical direction, resulting in  $Q = -B$ . This component has no net diagonal polarization or circular polarization, thus  $U = V = 0$ .

The second component is the depolarized component, described by the Stokes vector  $\begin{bmatrix} A \\ 0 \\ 0 \\ 0 \end{bmatrix}$ .

These elements indicate a beam of light of intensity  $I = A$  which exhibits no net polarization in any form,  $Q = U = V = 0$ . It is this intensity which is removed from the image in DPL imaging.

Armed with this information, the polarization of the total signal reflected from the sample may be expressed as the sum of these polarized and depolarized components:

$$\begin{bmatrix} A \\ 0 \\ 0 \\ 0 \end{bmatrix} + \begin{bmatrix} B \\ -B \\ 0 \\ 0 \end{bmatrix} = \begin{bmatrix} A + B \\ -B \\ 0 \\ 0 \end{bmatrix}$$

Having arrived at an expression for the Stokes vector of the reflectance, it is now desired to study the effect the polarizing elements of the device have on this signal.

The transformation in the polarization of light as it passes a polarizing element is quantified in the context of Stokes vectors in the form of Mueller matrices. Given light of a certain Stokes vector incident on a polarizing element, the resulting Stokes vector of the light transmitted through the optic is given by the multiplication of the incident vector with the

Mueller matrix associated with the polarizing optic. Ideally, there are only two polarizing optics the sample reflectance must pass through in this system: the wavelength retarder and the analyzer. The Mueller matrix for the analyzer (or more generally, a linear polarizer) provides a good introduction to the properties of Mueller matrices, and the matrix for the horizontally aligned analyzer used in the system is given below:

$$\frac{1}{2} \begin{bmatrix} 1 & 1 & 0 & 0 \\ 1 & 1 & 0 & 0 \\ 0 & 0 & 0 & 0 \\ 0 & 0 & 0 & 0 \end{bmatrix}$$

To put this matrix in a more intuitive context, if we imagine a beam of depolarized light

(Stokes vector  $\begin{bmatrix} A \\ 0 \\ 0 \\ 0 \end{bmatrix}$ ) incident on a linear polarizer, intuitively we would expect the transmitted

beam of light to be entirely linearly polarized and half the intensity of the incident beam.

Expressing this transformation in Mueller calculus:

$$\frac{1}{2} \begin{bmatrix} 1 & 1 & 0 & 0 \\ 1 & 1 & 0 & 0 \\ 0 & 0 & 0 & 0 \\ 0 & 0 & 0 & 0 \end{bmatrix} \begin{bmatrix} A \\ 0 \\ 0 \\ 0 \end{bmatrix} = \begin{bmatrix} (1/2) A \\ (1/2) A \\ 0 \\ 0 \end{bmatrix}$$

This confirms our intuition, the resulting Stokes vector indicates that the beam is half the intensity of the incident ( $I = 1/2 A$ ), and the entirety of this intensity is linearly polarized in the horizontal direction ( $Q = 1/2 A$ , while  $U = V = 0$ ).

Now we consider the Mueller matrix of a wavelength retarder oriented with its fast axis 45 degrees offset from the horizontal, as applied in our system:

$$\begin{bmatrix} 1 & 0 & 0 & 0 \\ 0 & \cos \varphi & 0 & -\sin \varphi \\ 0 & 0 & 1 & 0 \\ 0 & \sin \varphi & 0 & \cos \varphi \end{bmatrix}$$

Here, the parameter  $\varphi$  refers to the phase difference imposed by the retarder between light polarized along its fast and slow axis, henceforth referred to as the phase retardance. The two operating states of this retarder are at half-wavelength retardance ( $\varphi = \pi$  radians) and zero retardance ( $\varphi = 0$  radians). The corresponding Mueller matrices for these two states are

$$\begin{bmatrix} 1 & 0 & 0 & 0 \\ 0 & -1 & 0 & 0 \\ 0 & 0 & 1 & 0 \\ 0 & 0 & 0 & -1 \end{bmatrix} \text{ and } \begin{bmatrix} 1 & 0 & 0 & 0 \\ 0 & 1 & 0 & 0 \\ 0 & 0 & 1 & 0 \\ 0 & 0 & 0 & 1 \end{bmatrix} \text{ respectively. Recall that the purpose of the wavelength}$$

retarder here is to first rotate the collected signal polarization by 90 degrees to expose the parallel (to the illumination polarization) image to the camera through the analyzer, then be switched to have no effect on the signal to expose the perpendicular image to the camera through the analyzer. Computing the Mueller calculus for these two transformations on the reflectance signal

$$\text{of polarization } \begin{bmatrix} A+B \\ -B \\ 0 \\ 0 \end{bmatrix} :$$

$$\text{For zero retardance: } \begin{bmatrix} 1 & 0 & 0 & 0 \\ 0 & 1 & 0 & 0 \\ 0 & 0 & 1 & 0 \\ 0 & 0 & 0 & 1 \end{bmatrix} \begin{bmatrix} A+B \\ -B \\ 0 \\ 0 \end{bmatrix} = \begin{bmatrix} A+B \\ -B \\ 0 \\ 0 \end{bmatrix}, \text{ and the signal is unchanged.}$$

$$\text{For half-wave retardance: } \begin{bmatrix} 1 & 0 & 0 & 0 \\ 0 & -1 & 0 & 0 \\ 0 & 0 & 1 & 0 \\ 0 & 0 & 0 & -1 \end{bmatrix} \begin{bmatrix} A+B \\ -B \\ 0 \\ 0 \end{bmatrix} = \begin{bmatrix} A+B \\ B \\ 0 \\ 0 \end{bmatrix}, \text{ in this case the only change to}$$

the signal is the 90-degree rotation of the polarized light, flipping the sign of  $Q = -B$  to  $B$ .

The complete transformation of the collected reflectance from the sample as it travels to the camera may now be described by the series of transformations it experiences as it passes first the wavelength retarder, then the analyzer:

For the parallel signal ( $\varphi = \pi$  radians):

$$\frac{1}{2} \begin{bmatrix} 1 & 1 & 0 & 0 \\ 1 & 1 & 0 & 0 \\ 0 & 0 & 0 & 0 \\ 0 & 0 & 0 & 0 \end{bmatrix} \begin{bmatrix} 1 & 0 & 0 & 0 \\ 0 & -1 & 0 & 0 \\ 0 & 0 & 1 & 0 \\ 0 & 0 & 0 & -1 \end{bmatrix} \begin{bmatrix} A + B \\ -B \\ 0 \\ 0 \end{bmatrix} = \frac{1}{2} \begin{bmatrix} A + 2B \\ 2B \\ 0 \\ 0 \end{bmatrix}$$

For the perpendicular signal ( $\varphi = 0$  radians):

$$\frac{1}{2} \begin{bmatrix} 1 & 1 & 0 & 0 \\ 1 & 1 & 0 & 0 \\ 0 & 0 & 0 & 0 \\ 0 & 0 & 0 & 0 \end{bmatrix} \begin{bmatrix} 1 & 0 & 0 & 0 \\ 0 & 1 & 0 & 0 \\ 0 & 0 & 1 & 0 \\ 0 & 0 & 0 & 1 \end{bmatrix} \begin{bmatrix} A + B \\ -B \\ 0 \\ 0 \end{bmatrix} = \frac{1}{2} \begin{bmatrix} A \\ A \\ 0 \\ 0 \end{bmatrix}$$

Subtracting the perpendicular signal from the parallel, the resulting DPL signal has the Stokes

vector  $\overrightarrow{S_{DPL}} = \begin{bmatrix} B \\ B \\ 0 \\ 0 \end{bmatrix}$ , which recovers the intensity  $I = B$  of the reflectance retaining the illumination

polarization from the initial total reflectance of  $\begin{bmatrix} A \\ 0 \\ 0 \\ 0 \end{bmatrix} + \begin{bmatrix} B \\ -B \\ 0 \\ 0 \end{bmatrix} = \begin{bmatrix} A + B \\ -B \\ 0 \\ 0 \end{bmatrix}$ .

Having been familiarized with the Mueller conceptualization of the system optics, we can now apply this description to better understand some of the sources of error introduced by the non-ideal functionality of the system components.

In the ideal analysis conducted earlier it was assumed that the laparoscope exhibited no polarization effects. In reality, this is not the case: in the work of Wood et al. (2010), the

polarization effects of several commercial laparoscopes (including our Karl-Storz variant) are demonstrated by the measurement of the Mueller matrix for each point in the field of view of the laparoscope. It was suspected and validated by the authors that for the Storz model much of these polarization effects were due to the presence of a sapphire crystal window in the device. To improve on these properties, in a separate paper the authors use a less polarizing replacement for the sapphire window in the form of fused silica (Qi et al., 2012). Once again, they measured the Mueller matrix over the field of view of the device. Their results for these matrices are displayed below for the sapphire and fused silica crystal respectively:

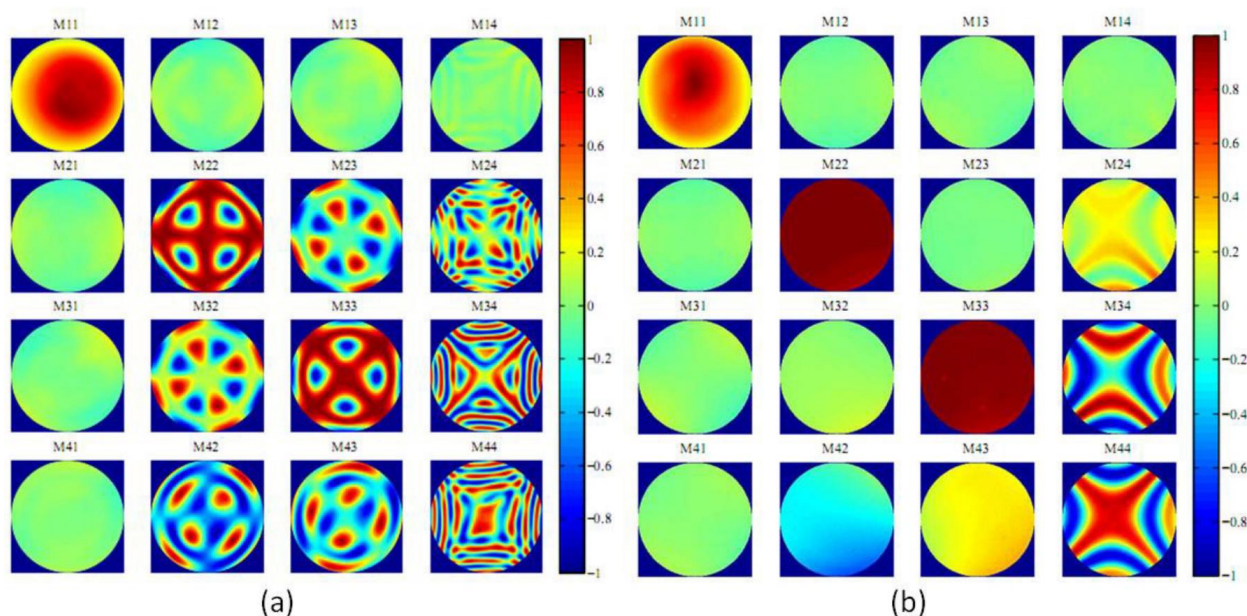


Figure 28: Mueller matrix values as a function of position within the field of view of a Karl-Storz laparoscope with a sapphire window (a), and a fused silica window (b) (Qi et al., 2012).

These data may seem daunting at first glance, but there are only a few key features we are concerned with. Since it is desired that the laparoscope be a non-polarizing optic, we must find regions in the field of view where the Mueller matrix resembles that of a non-polarizing optic. The non-polarizing Mueller matrix is the 4x4 identity matrix, which has zeros (0) at all the

sixteen indices, with the exceptions of ones (1) occupying the diagonal running from the top left to bottom right, which appears as

$$\begin{bmatrix} 1 & 0 & 0 & 0 \\ 0 & 1 & 0 & 0 \\ 0 & 0 & 1 & 0 \\ 0 & 0 & 0 & 1 \end{bmatrix}$$

Looking at the matrix for the sapphire window configuration in 28a (our configuration), it is possible to meet these criteria given certain restrictions to the field of view. If the FOV is limited to area surrounding the center, the state of the matrix comes very close to the form of the identity matrix detailed above, making it possible to conduct polarization-sensitive analysis within this region of the image relayed by the laparoscope. As depicted in 28b, it is possible to reduce the polarization effects of the laparoscope by replacing the sapphire window with fused silica, reducing the restrictions on the viable field of view that forms an identity Mueller matrix. However, there are still some elements of this matrix that still heavily depend on the position in the field of view (those in the 4th column).

Composing a Mueller matrix to represent the laparoscope:

$$\begin{bmatrix} 1 & 0 & 0 & 0 \\ 0 & m_{22} & m_{23} & m_{24} \\ 0 & m_{32} & m_{33} & m_{34} \\ 0 & m_{42} & m_{43} & m_{44} \end{bmatrix}$$

This matrix was derived from features in figure 28a. Here, only the matrix elements in the first row and first column have a consistent value ( $\sim 1$  for the top left,  $\sim 0$  for the rest) throughout the field of view. These values are reflected in our derived Mueller matrix. The remaining elements vary in value as a function of position in the field of view, and are

represented as variables  $m_{ij}$  for the  $i$ -th row and  $j$ -th column. For the transformation of the sample reflectance as it passes first through the laparoscope, then the retarder, and finally the analyzer, we have

$$\frac{1}{2} \begin{bmatrix} 1 & 1 & 0 & 0 \\ 1 & 1 & 0 & 0 \\ 0 & 0 & 0 & 0 \\ 0 & 0 & 0 & 0 \end{bmatrix} \begin{bmatrix} 1 & 0 & 0 & 0 \\ 0 & \cos \varphi & 0 & -\sin \varphi \\ 0 & 0 & 1 & 0 \\ 0 & \sin \varphi & 0 & \cos \varphi \end{bmatrix} \begin{bmatrix} 1 & 0 & 0 & 0 \\ 0 & m_{22} & m_{23} & m_{24} \\ 0 & m_{32} & m_{33} & m_{34} \\ 0 & m_{42} & m_{43} & m_{44} \end{bmatrix} \begin{bmatrix} A + B \\ -B \\ 0 \\ 0 \end{bmatrix}$$

$$= \frac{1}{2} \begin{bmatrix} A + B - m_{22}B \cos \varphi + m_{42}B \sin \varphi \\ A + B - m_{22}B \cos \varphi + m_{42}B \sin \varphi \\ 0 \\ 0 \end{bmatrix}$$

(Here the phase retardance  $\varphi$  of the wavelength retarder is left as a variable to study the influence of its value). Calculating the DPL Stokes vector where  $\varphi_{\perp}$  is the retardance for exposing the perpendicular image and  $\varphi_{\parallel}$  for the parallel image:

$$\vec{S}_{DPL} = \frac{1}{2} \begin{bmatrix} m_{22}B(\cos \varphi_{\perp} - \cos \varphi_{\parallel}) + m_{42}B(\sin \varphi_{\parallel} - \sin \varphi_{\perp}) \\ m_{22}B(\cos \varphi_{\perp} - \cos \varphi_{\parallel}) + m_{42}B(\sin \varphi_{\parallel} - \sin \varphi_{\perp}) \\ 0 \\ 0 \end{bmatrix}$$

An interesting detail to note is the only variable elements of the laparoscope Mueller matrix whose value has any effect on the detected signal are  $m_{22}$  and  $m_{42}$ , corresponding to M22 and M42 in figure 28. For these two elements to have no influence on the polarization of our signal, they must be one and zero respectively. For the sapphire matrix (28a) this condition is only met near the center of the field of view. However, if the sapphire were to be replaced with fused silica as in 28b, these elements exhibit a uniform distribution close to their target values of 1 and 0.

If we assume the retarder is accurate in the application of its zero ( $\varphi_{\perp} = 0$ ) and half-wavelength ( $\varphi_{\parallel} = \pi$ ) retardances, the expression for the DPL Stokes vector simplifies to  $\begin{bmatrix} m_{22}B \\ m_{22}B \\ 0 \\ 0 \end{bmatrix}$ .

This is an intriguing result: given the ideal function of the wavelength retarder, the only variable element of the laparoscope Mueller matrix that has any impact on the DPL signal is that associated with  $m_{22}$ , that is M22 in figure 28a and b. If this element's value is close to one and the retarder is accurate, the DPL Stokes vector returns to its ideal form calculated earlier:  $\overline{S_{DPL}} = \begin{bmatrix} B \\ B \\ 0 \\ 0 \end{bmatrix}$  accurately yielding intensity B, the sought intensity of the light retaining the illumination polarization. Thus, accurate DPL imaging relies regions within only M22 being close to one given ideal retarder function. This element is also completely uniform in the fused silica window, providing an option for overcoming the potential field of view limitations in the sapphire window.

Following the study of the laparoscope effects, the next step is to determine the potential impact the wavelength dependence of the retardance has on the collected DPL signal. For a static retarder (representative of our retarder at a constant voltage), the wavelength retardance ( $\delta$ ) may be described as  $\delta(\lambda) = \frac{\beta d}{\lambda}$ , where  $\beta$  is birefringence, and  $d$  is the geometric thickness of the retarder (Meadowlark Optics, 2005). Combining this knowledge with the retardance data provided by the manufacturer at two wavelengths (Thorlabs, 2017, plotted in figure 23, raw data can be found in appendix D), and approximating the variation of birefringence with wavelength



as a linear dependence, a model of the form  $\delta(\lambda) = \frac{C}{\lambda} + D$  is parameterized to estimate the wavelength dependence in the regime around each operating voltage:

$$\text{At } 25\text{V}, \delta_{25\text{V}}(\lambda) = \frac{111\text{nm}}{\lambda} - 0.156$$

$$\text{At } 1.4\text{V}, \delta_{1.4\text{V}}(\lambda) = \frac{303\text{nm}}{\lambda} - 0.0574$$

Based on the Stokes vector for the signal detected by the camera from earlier, assuming the signal is from a region in the field of view of the laparoscope that is not polarizing ( $m_1 = 1$ ,  $m_7 = 0$ ) the Stokes vector describing the calculated DPL signal is:

$$\overrightarrow{S_{DPL}} = \frac{1}{2} \begin{bmatrix} B(\cos \varphi_{25\text{V}} - \cos \varphi_{1.4\text{V}}) \\ B(\cos \varphi_{25\text{V}} - \cos \varphi_{1.4\text{V}}) \\ 0 \\ 0 \end{bmatrix}$$

Where  $\varphi_{25\text{V}}$  and  $\varphi_{1.4\text{V}}$  are the phase retardances applied at 25 and 1.4V respectively, which may be expressed simply as the wavelength retardance  $\delta(\lambda)$  at that voltage multiplied by  $2\pi$ . The intensity of the signal is expressed as the top element in this vector multiplied by  $1/2$ , thus the error fraction of this signal compared to the expected intensity of the polarized component (B) may be expressed as

$$\frac{\text{observed} - \text{expected}}{\text{expected}} = \frac{(1/2)B(\cos(\varphi_{25\text{V}}) - \cos(\varphi_{1.4\text{V}})) - B}{B}$$

$$\text{error} = 0.5(\cos(\varphi_{25\text{V}}) - \cos(\varphi_{1.4\text{V}})) - 1$$

$$\text{Where } \varphi_{25\text{V}}(\lambda) = (2\pi)(\delta_{25\text{V}}(\lambda)) = (2\pi)\left(\frac{111\text{nm}}{\lambda} - 0.156\right)$$

$$\text{And } \varphi_{1.4\text{V}}(\lambda) = (2\pi)(\delta_{1.4\text{V}}(\lambda)) = (2\pi)\left(\frac{303\text{nm}}{\lambda} - 0.0574\right)$$

Substituting these phase retardance functions, we obtain the expression for the error fraction due to the retarder as a function of wavelength:

$$errFraction(\lambda) = 0.5 \left( \cos \left( (2\pi) \left( \frac{111nm}{\lambda} - 0.156 \right) \right) - \cos \left( (2\pi) \left( \frac{303nm}{\lambda} - 0.0574 \right) \right) \right) - 1$$

Plotting this function:

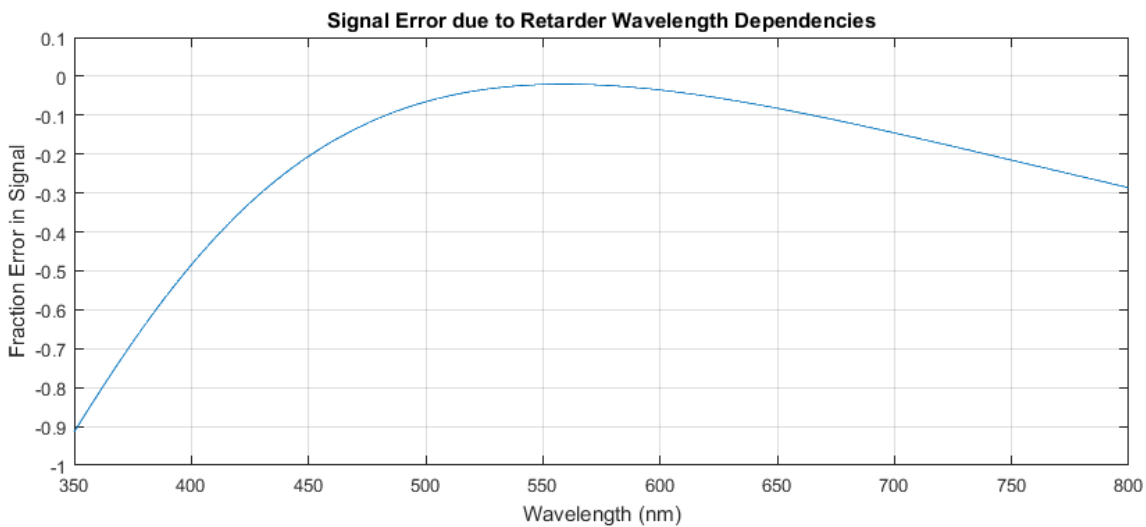


Figure 29: Fraction of error in signal due to the wavelength dependencies of the retarder as a function of signal wavelength.

Thus, the observed signal of intensity  $I$  and wavelength  $\lambda$  may be expressed as

$$I = I_0 + I_0(errFraction(\lambda))$$

$$I = I_0 \left( 0.5 \left( \cos \left( (2\pi) \left( \frac{111nm}{\lambda} - 0.156 \right) \right) - \cos \left( (2\pi) \left( \frac{303nm}{\lambda} - 0.0574 \right) \right) \right) \right)$$

$$I = I_0(error(\lambda))$$

Where  $I_0$  is the expected intensity of the signal.

We now look to the illumination spectrum of the lamp and the detection spectrum of the RGB camera to approximate the expected signal intensity  $I_0$  as a function of wavelength.

Examining the spectra recorded for the Storz lamp applied in our system:

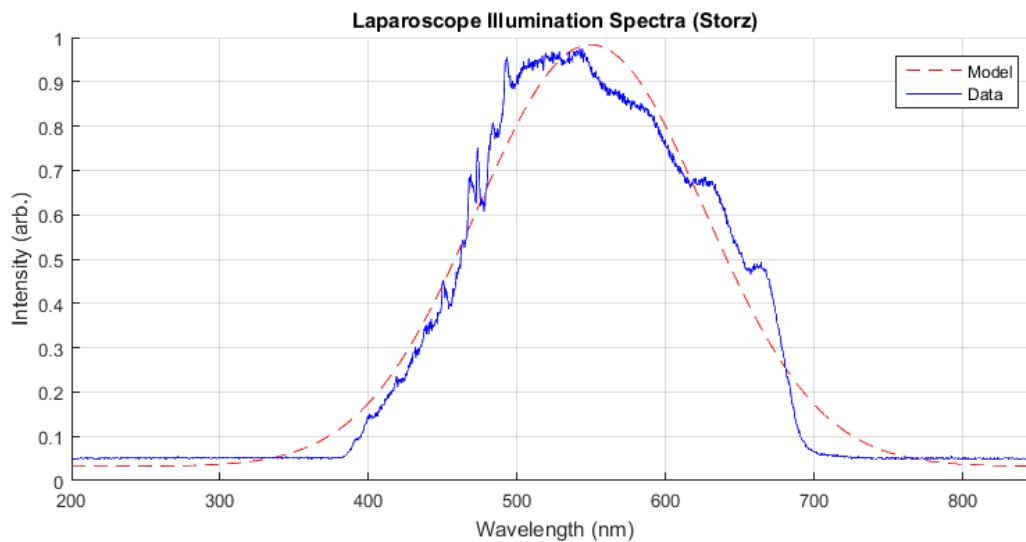


Figure 30: Plot of the measured illumination intensity spectrum for the xenon arc lamp used in the Storz laparoscope. Spectrum is modeled by a Gaussian.

The function of the illumination intensity as a function of wavelength is approximated here by a Gaussian (red dashed line).

Below are the transmission spectra for the three filters applied in our RGB camera's Bayer-tiled sensor mosaic, supplied by the manufacturer. These three spectra are once again approximated by Gaussians which each share the center wavelength (dotted line) and peak efficiencies of their corresponding data plot:

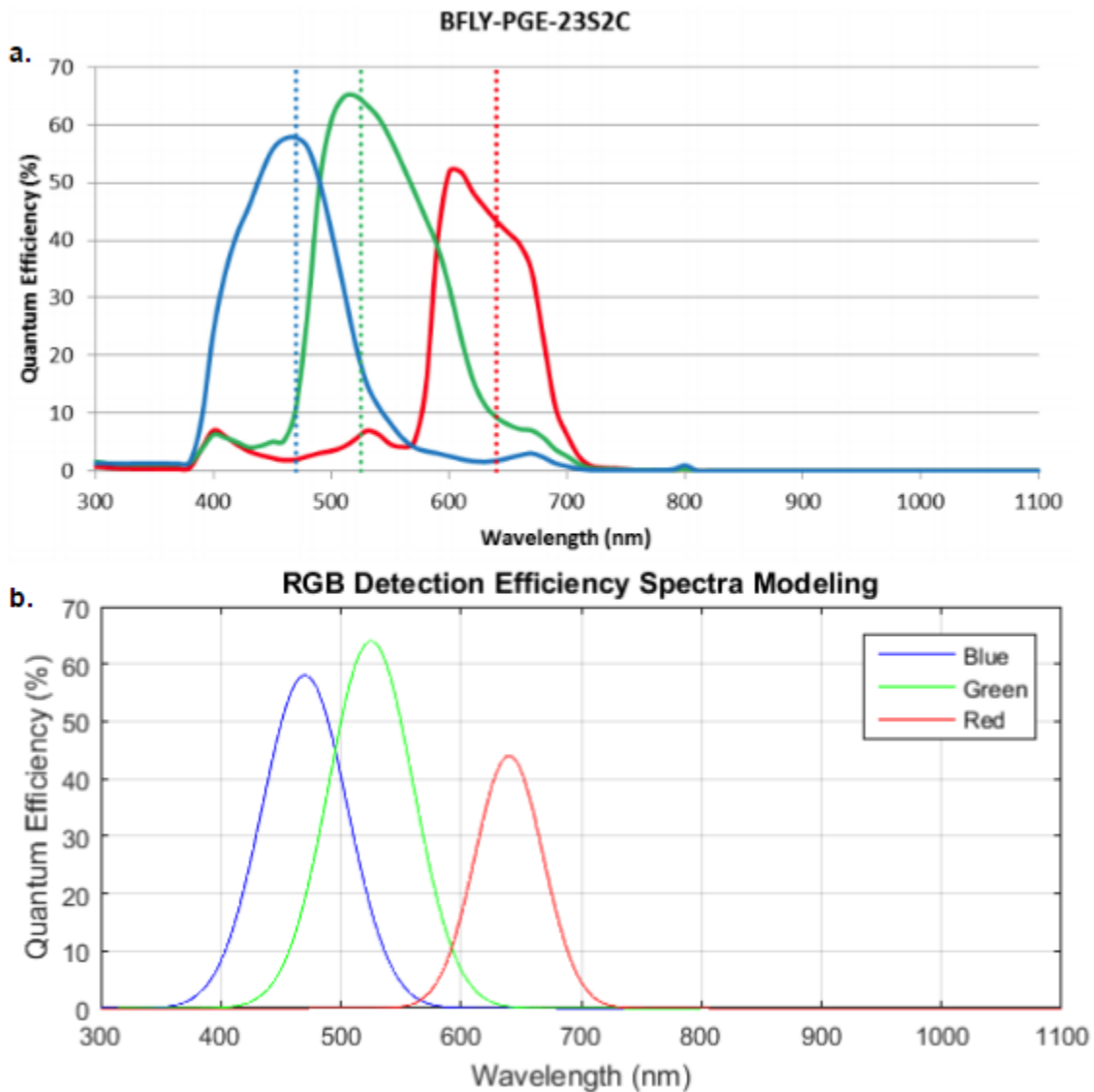


Figure 31: Detection efficiency spectra for the RGB camera used (FLIR 2017). Manufacturer-provided data in a, corresponding Gaussian models of this data in b.

The expected signal ultimately detected by the camera for each color pixel may be estimated as the product of the illumination spectra (figure 30) and the detection efficiencies (31b), yielding the solid-line plots in figure 32 below. To introduce the retarder error, we multiply these spectra by the error function  $\text{error}(\lambda)$  defined earlier. The resulting spectra (figure 32, dashed lines) model the observed signal:

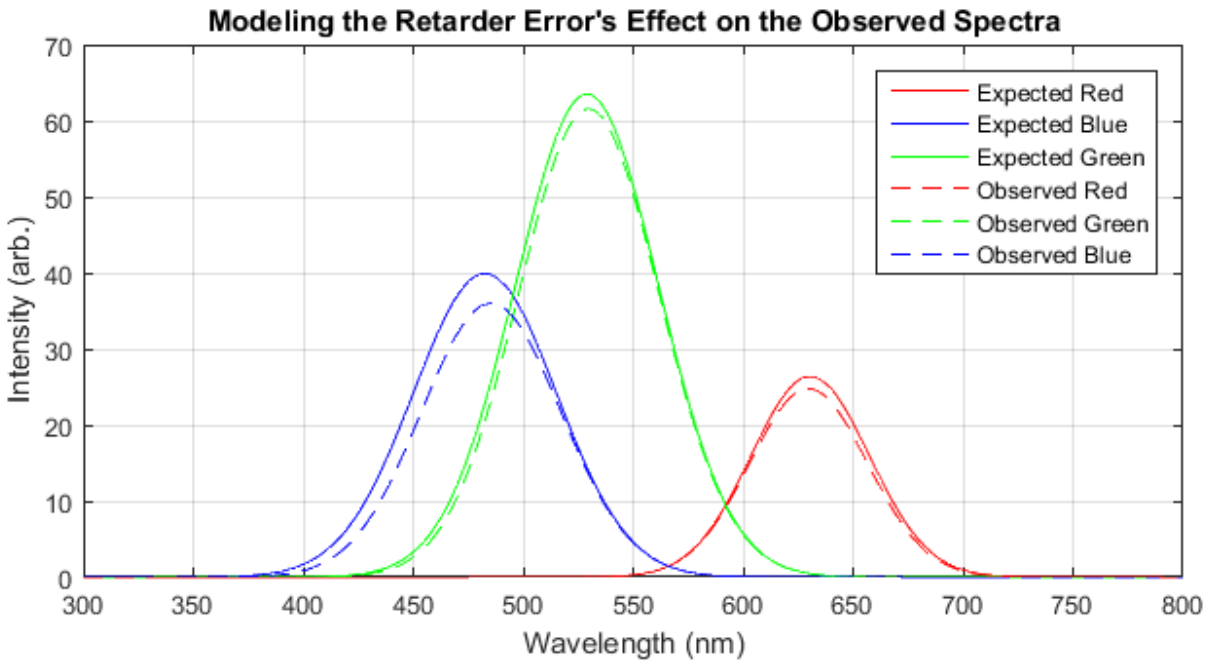


Figure 32: Expected and observed spectra for the RGB camera signal detection of the illumination. Expected case is without the influence of the retarder error (solid lines), observed is with this error included (dashed lines).

The intensity value reported by the camera is given by the integral of each of these spectra over the entire spectrum (~300-800nm):

$$I_{red} = \int_{300nm}^{800nm} I_{red}(\lambda) d\lambda$$

$$I_{green} = \int_{300nm}^{800nm} I_{green}(\lambda) d\lambda$$

$$I_{blue} = \int_{300nm}^{800nm} I_{blue}(\lambda) d\lambda$$

Calculating the error fraction between the observed and expected intensities for each color channel:

$$\frac{I_{red,obs} - I_{red,exp}}{I_{red,exp}} = -0.0643$$

$$\frac{I_{green,obs} - I_{green,exp}}{I_{green,exp}} = -0.0461$$

$$\frac{I_{blue,obs} - I_{blue,exp}}{I_{blue,exp}} = -0.125$$

These calculations and the spectra they are derived from may be examined in detail in the MATLAB code of appendix B-3. The error is lowest for the green channel (4.61%) and highest for the blue channel (12.5%) with red in between (6.43%). This trend is reflected in the plot of the retarder error function in figure 29, where the error magnitude is minimized around the green band, highest along the blue band, and intermediate in the red band. These errors serve as estimators of DPL signal error that may be encountered during operation in the manner proposed in the previous section. The error values suggest that this method of operation is indeed feasible, collecting wideband RGB signal with only two retarder voltage settings despite the associated wavelength dependence. If for whatever reason it is desired to reduce this error, it is also possible to tailor the voltage settings to each color channel individually. However, this requires the individual collection of each channels' signal rather than simultaneous detection, slowing the acquisition rate of the whole RGB image.

### **Device Verification**

With the proving of the theoretical functionality of this system design, the next logical step is to test the setup and verify its functionality experimentally. Naturally, it would make sense to image ex vivo tissues like those from Chapter 3 to ensure that the laparoscopic implementation of the system can maintain its performance relative to the benchtop configuration. This is simple enough, but in addition it is desired to probe the limits of the device

concerning the geometry of the lesions, that is, how small and thin of a lesion can the device detect versus conventional imaging? This is difficult to study rigorously with excised tissues, thus the possibility of fabricating an optical phantom with the desired geometry was investigated.

It was decided that the best substrate to compose the phantom would be polydimethylsiloxane (PDMS). This polymer base in its initial state is a viscous fluid that may be cast against a mold. After adding a curing agent, the base cures solid, retaining the features impressed upon it by the mold with great detail ( $<1\mu\text{m}$  resolution). By default, PDMS is optically clear in the visible range. This allows the control of the optical properties by adding optically active agents to the base prior to curing. With this, a phantom may be fabricated with tunable geometry and optical properties. The figure below details the protocol developed to create such a phantom:

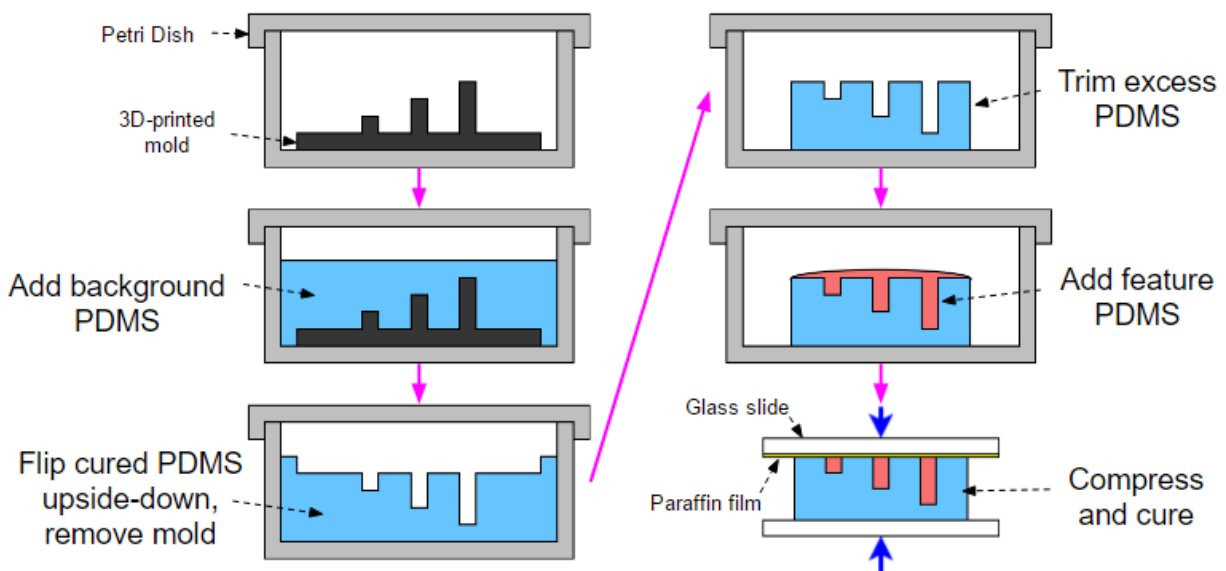


Figure 33: Process diagram describing the fabrication of a PDMS optical phantom with controlled feature geometry.

Following the process beginning in the top left, a 3D-printed mold is placed in a petri dish. This mold defines the size and thickness of the resulting phantom features. The dish is then

filled with a PDMS with optical properties representative of the background and the assembly is degassed for one hour. After curing, the PDMS and mold are flipped upside-down in the dish, and the mold is removed. The excess PDMS is then trimmed off, and the surface is covered in PDMS with optical properties representative of the feature. The film of excess feature PDMS is then squeezed out as the phantom is clamped between two glass slides. To prevent the PDMS from sticking to the slide as it cures, the slide in contact is covered in paraffin film (Bemis NA) for easier separation.

The mold design was printed on a Solus 3D printer (Junction 3D) from the proprietary resin SolusProto. The SolidWorks design file from which this mold was printed (figure 34a) and a resulting phantom prototype (b) are detailed below:

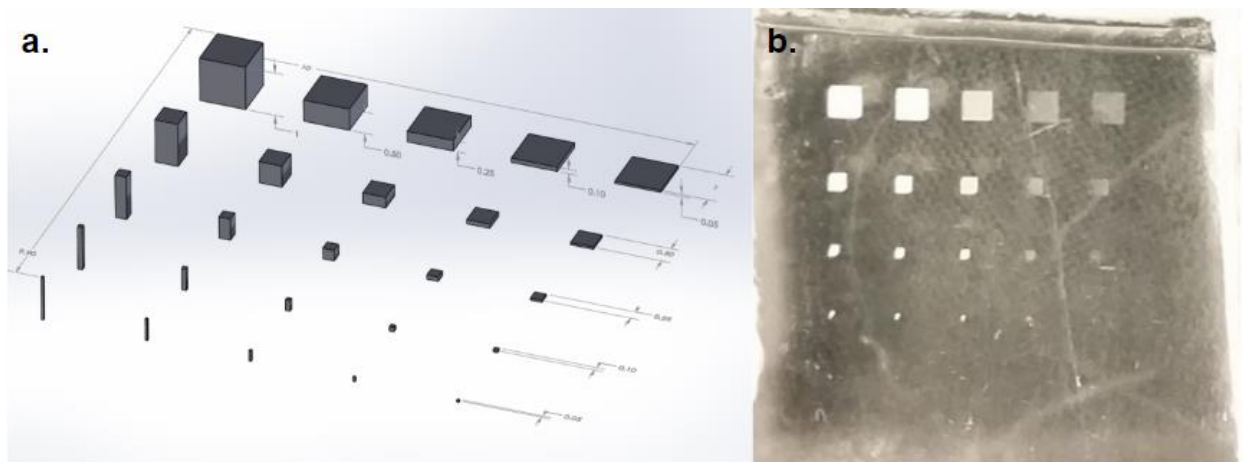


Figure 34: (a) SolidWorks model of the printed mold defining feature geometries. (b) PDMS phantom resulting from the mold printed from this design.

The mold defines an array of twenty-five different feature geometries. Each row contains features of the same area with decreasing thickness (depth) from left to right ranging from 1mm to 50 $\mu$ m. Each column contains features of the same thickness, while the dimensions of the area are varied ranging from 1x1mm to 50x50 $\mu$ m. The background PDMS (Sylgard 184, 1:10 curing agent to base ratio) in this case had no optical agents added, while rutile titanium dioxide powder



was added to the feature PDMS (6mg/g concentration) to help visualize the feature geometry. The fabrication protocol proved reasonably effective; features down to the fourth row translated to the phantom effectively, while the fifth row (50x50um) failed to be cleanly printed in the mold due to approach of resolution limit. With this degree of control over the feature geometry, the phantom can be effectively applied to study the sensitivity of the system to lesions of different size and thickness.

### **Alternative Design Considerations**

The proposed design here is only one of several possible configurations capable of DPL imaging, but it was selected as the most promising of these possibilities. Alternatives include the use of two cameras some combination of optical elements that separates the parallel and perpendicular components of the reflectance and directs each to its own camera. The advantage to having such a two-camera system relative to a singular one is that given all the cameras used here have the same max frame rate, a two-camera system would be able to stream DPL images at this max frame rate, while a single camera system would only be able to do so at half this frame rate. This follows from the single camera having to image two frames (parallel and perpendicular) for every DPL frame produced, while in the two-camera setup each of these two component frames is collected by a separate camera, allowing the resulting DPL image stream to be collected at the full framerate. However, there are notable difficulties to be considered in the technical details of a two-camera setup that are not applicable in a single camera design. First and most simply, a two-camera design would not be as compact and a singular one. This device is intended to be handheld by a clinician over the course of potentially long periods of time, thus it is of interest to minimize the size and weight to improve the efficacy and comfort with which

the clinician may operate it. Additionally, with each parallel and perpendicular image being resolved through two different optical paths, special care is required to ensure the paths are as close to identical as possible to ensure that no artifacts arise when subtracting the images from one another due to path difference. Finally, the most critical difficulty in a two-camera system is the challenge of splitting the collected signal and appropriately distributing it to each camera. The optical element that immediately comes to mind for this application is a 50:50 beam splitter, or a polarizing beam splitter. The primary problem with beam splitters in this case is that depending on the specific beam splitter there will be various angular, spectral, and/or polarization dependencies that will interfere with the signal in the resulting images. Conversely, the wavelength retarder exhibits only a subtle spectral dependence that is not of significance in our application. Beyond beam splitters, if one really wanted to push towards a two-camera system, a more realistic optic would be a Wollaston prism. These prisms would be able to separate orthogonal components of polarization into each camera with only a small spectral dependence.

## CHAPTER 5: CURRENT DIRECTIONS FINAL THOUGHTS

### Introduction

The work exhibited here makes a good case for DPL imaging as a solution to the clinical need. However, there is still an amount of additional progress required to arrive at the final goal of clinical implementation. It is the purpose of this section to outline this progress and its current stage, and ultimately comment on the project as a whole.

### Additional Device Development

There are still a few features of the system which are still currently in need of further development: the device control software and the polarizing cap of the laparoscope system.

The overview of the current software build was detailed previously in the device design section of Chapter 4 (code exhibited in appendix C). While conceptually sound, there are a few practical problems that hinder it. To start, the program ensures that the frame exposure and retarder switching are initialized in sync, but afterwards they operate independently of one another. The continued synchronization of the components relies on the precise matching of the camera capture and retarder switching frequencies. Given enough time, even the slightest frequency mismatch will result in the gradual desyncing of the components' operation. Thus, for sustained operation, a better implementation would be one in which the camera's end of exposure event would trigger the switching of the retarder on a frame-by-frame basis rather than just initialize its switching after the first end of exposure event occurs. This possibility was investigated, but it was discovered that if the frame rate of the camera is too high (above ~10fps) the end of exposure event triggering cannot keep up and will not trigger on every frame.

An alternative solution is proposed for future development involving a more hardware-oriented approach. Here, the camera's "strobe" (voltage pulse issued by the camera following every image exposure) feature would be exploited. The retarder controller would be calibrated such that this strobe acts as a hardware trigger to switch its voltage output. This would help bypass any software limitations of the system and provide simpler and more reliable functionality.

Regardless of the approach settled on, it is also desired to maintain the camera's compatibility with the manufacturer's software UI (user interface) following the implementation of the approach. The ability to continue using the camera's default UI would provide several features from the start that would not have to be developed later otherwise. These include most importantly the live streaming of camera imaging to a screen, infrastructure for the modification of camera settings while imaging, and triggers for camera recording and saving video to file.

Concerning the polarizing cap, the current prototype can effectively polarize the illumination in a benchtop setting, but there are some additional requirements it must meet before seeing use in the clinic. Namely, its attachment to the laparoscope must be secured, and the component must be made sterilizable by clinical means following its contact with the patient. It possible that the former be realized through the conversion of the polarizer from a cap to a sleeve configuration. In this case, the entire length of the laparoscope lens rod is covered by a rigid sleeve with a window at the distal end that contains the polarizing film for the illumination. The position and angular orientation of this sleeve is secured relative to the lens rod by its attachment to the perpendicular metal tube at the proximal end of the laparoscope. The materials from which the current cap is fabricated are not very heat-tolerant in the context of autoclave

sterilization at 121 degrees Celsius. The housing is composed of a proprietary 3-D printed material called VeroClear, which exhibits warping at temperatures in excess of 50C (Stratasys, 2016). Thus, barring the replacement of this material with a more heat-resistant one (polypropylene, polycarbonate, polymethylpentene, etc.) autoclaving is not a practical means of sterilization. Instead, it is recommended that sterilization by ethylene oxide is applied to avoid heat-induced damage to the component.

### **PDMS Phantom Testing**

Thus far, an effective protocol has been developed for the fabrication of PDMS optical phantoms as detailed in the prior chapter. What remains is to investigate the different optical agents that may be added to the PDMS to model in vivo pathology. In the context of peritoneal metastases, the primary characteristics these agents should mimic include the absorbance of hemoglobin exhibited by blood vessels in the peritoneum background and the high scattering of the cancer lesions relative to the peritoneum. Initial candidates for the scattering agent include the titanium dioxide powder used in the phantom prototype, as well as hollow glass microspheres. Polystyrene microspheres are also a possibility, however they are less cost-effective are usually stored in solution at relatively low concentration (~2% by volume) potentially creating difficulties in modeling higher scattering where a greater optical density is desired. Wide-band absorptive properties may be introduced with the addition of dyes like nigrosin or India ink, while absorption more representative of blood vessels may be modeled with the addition of powder hemoglobin.

Additionally, following the fabrication of the desired phantom, it would be prudent to verify the features of finer width and depth. Visual inspection is not sufficient in this case, rather it would be more effective to apply confocal microscopy. This allows the detailed inspection of small-width features, but more importantly provides depth-resolved imaging for the measurement of the thickness of the thinner features.

## **Conclusion**

It is believed that the application of DPL imaging in the clinic will help enhance the ability of physicians to make more accurate diagnoses concerning the presence or absence of peritoneal metastases. As the work here demonstrates, this belief is not unfounded. Evidence indicates that DPL imaging can provide a significant increase in the contrast between tumor tissue and the peritoneum. Additionally, there exists a reasonable method by which this imaging modality may be implemented in the desired clinical setting without greatly compromising its performance. Combined with the current dissatisfaction with the sensitivity of lesion detection, such a device would have a positive impact on patients at risk for these metastases. Ultimately, it is this potential for impact which decides the worth of the continued development of this device. It is thus concluded that the DPL imaging modality would prove to be a realistic and effective means to meet the clinical need outlined here. As a result, its continued development towards clinical application should be strongly considered.

## APPENDICES

### A. Cancer Incidence Data

#### A-1. Cancer Incidence Rates

##### Age-Specific (Crude) SEER Incidence Rates; by Cancer Site; All Ages, All Races, Both Sexes; 2005-2014

Age At Diagnosis (years)	Rate for all Cancer Varieties (per 100k)	Rate for Digestive System Varieties (per 100k)
<1	23.7989	1.9666
1-4	21.6982	0.9544
5-9	12.5177	0.2081
10-14	13.8358	0.335
15-19	22.0209	0.7601
20-24	36.1699	1.7829
25-29	57.4828	3.8317
30-34	88.9892	8.0047
35-39	134.2561	14.9501
40-44	217.9132	29.4457
45-49	353.194	55.9265
50-54	561.9879	106.1138
55-59	836.5394	151.3111
60-64	1208.1955	209.7537
65-69	1691.6209	289.2371
70-74	2028.445	374.6663
75-79	2293.1414	466.6783
80-84	2380.9708	548.701
85+	2224.3536	579.4303
Cumulative	14207.1312	2844.0574

#### A-2. Digestive System Cancer Stage Distribution

##### Stage Distribution (SEER Summary Stage 2000); by Cancer Site; All Ages, All Races, Both Sexes; 2005-2014

	Localized (percent)	Regional (percent)	Distant (percent)	Unstaged (percent)
Digestive System	32.4	31.6	27.3	8.8

## B. MATLAB Coding

### B-1. DPL Image Processing

```

%This script takes the pair of images obtained (grayscale or Bayer-tiled
%RGB) in parallel and perpendicular polarizations and performs the
%calibration and subtraction involved in computing the DPL image.

%Import all images you intend to work with to the workspace

%Settings START
calibrate = 0; %1 allows for calibration of image with a reference, 0 leaves the image
as is

bayerTiled = 0; %Image color type: 1 for bayer-tiled, 0 for grayscale

imRegistration = 1; %1 aligns parallel and perpendicular images to overlap features, 0
leaves their relative positions as is
%Settings END

%Data entry START
paraIm = parallelImage; %Enter parallel image
perpIm = perpendicularImage; %Enter perpendicular image
paraCal = parallelCalibrator; %Enter parallel calibrator image
perpCal = perpendicularCalibrator; %Enter perpendicular calibrator image
%Data entry END

paraIm = im2double(paraIm);
perpIm = im2double(perpIm);

if calibrate == 1; %Apply calibration
    paraCal = double(paraCal);
    perpCal = double(perpCal);
    paraIm = paraIm./imread(paraCal);
    perpIm = perpIm./imread(perpCal);
end

if imRegistration == 1; %Apply image co-registration
    [optimizer, metric] = imregconfig('Multimodal');
    perpIm = imregister(perpIm, paraIm, 'translation', optimizer, metric);
end

diffIm = (paraIm - perpIm); %Calculate difference of images (DPL image)

```



```

sumIm = ((paraIm/2 + perpIm/2)); %Calculate average of images (conventional image)

if bayerTiled == 1; %Additional processing for Bayer-tiled images
    colorParaIm = demosaic(im2uint16(paraIm),'gbrg'); %Convert Bayer-tiled images to
    RGB images
    colorPerpIm = demosaic(im2uint16(perpIm),'gbrg');
    colorSumIm = demosaic(im2uint16(sumIm),'gbrg');
    colorDiffIm = demosaic(im2uint16(diffIm),'gbrg');

    redParaIm = colorParaIm(:,:,1); %Separate the color channels in each image
    greenParaIm = colorParaIm(:,:,2);
    blueParaIm = colorParaIm(:,:,3);

    redPerpIm = colorPerpIm(:,:,1);
    greenPerpIm = colorPerpIm(:,:,2);
    bluePerpIm = colorPerpIm(:,:,3);

    redSumIm = colorSumIm(:,:,1);
    greenSumIm = colorSumIm(:,:,2);
    blueSumIm = colorSumIm(:,:,3);

    redDiffIm = colorDiffIm(:,:,1);
    greenDiffIm = colorDiffIm(:,:,2);
    blueDiffIm = colorDiffIm(:,:,3);
end

```

## B-2. Contrast Computation

```

%This script creates a data structure containing all of the output images
%from the RGB functionality of the image processing script and the contrast
%data associated with each

imageNames = char('diffIm', 'sumIm', 'paraIm', 'perpIm',... %Listing the workspace
image variable names from DPLImageProcessor
    'colorDiffIm', 'colorSumIm', 'colorParaIm', 'colorPerpIm',...
    'redDiffIm', 'redSumIm', 'redParaIm', 'redPerpIm',...
    'greenDiffIm', 'greenSumIm', 'greenParaIm', 'greenPerpIm',...
    'blueDiffIm', 'blueSumIm', 'blueParaIm', 'bluePerpIm');

numImages = length(imageNames(:,1)); %Counting the number of images

imageData(numImages) = struct('name', imageNames(numImages,:), 'image',
eval(imageNames(numImages,:)), 'contrast', -1, 'contrastStdev', -1); %Creating an
array of <numImages> structures that each can hold the name, image, and contrast data
for the image

```

```

for i = 1:numImages-1 %Loads images and their names into the structure array, contrast
values have not yet been determined so they are set to -1
    imageData(i) = struct('name', imageNames(i,:), 'image', eval(imageNames(i,:)),
'contrast', -1, 'contrastStdev', -1);
end

im = imageData(5).image; %Loads and shows image in figure for defining ROIs for
contrast calculation,
figure();
imshow(im);

disp('Press a key to continue') %Pause for zooming image if needed before defining
ROIs. Keypress continues program
pause;

%Generate glare mask
glareMask = glareMask(rgb2gray(imageData(5).image), .09, 2);

featureBoundary = imfreehand(); %Allows drawing of simply connected (no holes) ROI for
the feature
featureMask = logical((featureBoundary.createMask()).*not(glareMask)); %Mask for glare
featurePixels = sum(featureMask(:)); %Number of pixels in ROI

featureBoundaries = bwboundaries(featureMask); %Stores defined feature ROI
fROIxy = featureBoundaries{1}; % Get n by 2 array of x,y coordinates.

backgroundBoundary = imfreehand(); %Allows drawing of simply connected (no holes) ROI
for the background, should not intersect the feature ROI
backgroundMask =
logical((backgroundBoundary.createMask()).*not(glareMask).*not(featureMask)); %Mask
for glare
backgroundPixels = sum(backgroundMask(:)); %Number of pixels in ROI

backgroundBoundaries = bwboundaries(backgroundMask); %Stores defined background ROI
bROIxy = backgroundBoundaries{1}; % Get n by 2 array of x,y coordinates.

%Calculate mean contrast between defined feature and background
for i = 1:numImages
    im = im2double(imageData(i).image);

    featureMean = mean(im(featureMask));
    featureStdev = std(im(featureMask))/sqrt(featurePixels);
    backgroundMean = mean(im(backgroundMask));
    backgroundStdev = std(im(backgroundMask))/sqrt(backgroundPixels);

    imageData(i).contrast = (featureMean - backgroundMean)/backgroundMean; %Mean
contrast between feature and background

```

```

    imageData(i).contrastStdev =
sqrt(imageData(i).contrast^2*((featureStdev/featureMean)^2 +
(backgroundStdev/backgroundMean)^2)); %Standard deviation of mean contrast
end

sampleMask = logical((backgroundBoundary.createMask()).*not(glareMask)); %Mask for
glare
samplePixels = sum(sampleMask(:)); %Number of pixels in ROI

%Map the per pixel contrast against the sample mean for sum and difference
%images
finalPixels = sum(sampleMask(:)); %Count pixels in mask
sumMaskedAverage = sum(sum((rgb2gray(imageData(6).image)).*sampleMask))/finalPixels;
%Average intensity of masked sum image
diffMaskedAverage = sum(sum((rgb2gray(imageData(5).image)).*sampleMask))/finalPixels;
%Average intensity of masked diff image
maskedSum = (rgb2gray(imageData(6).image)).*sampleMask; %masked sum image
maskedDiff = (rgb2gray(imageData(5).image)).*sampleMask; %masked diff image

sumContrastMap = sampleMask.*((maskedSum - sumMaskedAverage)./sumMaskedAverage);
%Calculate the contrast of each pixel to the average intensity to create contrast map
diffContrastMap = sampleMask.*((maskedDiff - diffMaskedAverage)./diffMaskedAverage);
%Likewise for diff
lowerContrast = min([min(min(sumContrastMap)),min(min(diffContrastMap))]); %Find
minimum contrast value across both maps
upperContrast = max([max(max(sumContrastMap)),max(max(diffContrastMap))]); %Find
maximum contrast value across both maps
figure;imshow(sumContrastMap)
caxis([lowerContrast,upperContrast]) %Set upper and lower bounds
figure;imshow(diffContrastMap)
caxis([lowerContrast,upperContrast]) %Set the same upper and lower bounds for accurate
comparison

```

### B-3. Detected Signal Modeling

```

%This script serves to model the spectra detected by the RGB camera with
%(observed) and without (expected) the influence of the error introduced by
%the wavelength dependencies of the retarder.

x1 = 300:1:800; %wavelength range

%Create expected spectra and calculate detected signal
blueFun = @(x1) 58.*exp(-((x1-470)./50).^2).*... %Blue transmission function for
camera
(exp(-((x1-550)./113).^2)+.0323); %Lamp illumination spectra
blueSignal = integral(blueFun,300,800); %Signal integrated by camera

```

```

redFun = @(x1) 44.*exp(-((x1-640)./40).^2).*... %Same treatment for red
    (exp(-((x1-550)./113).^2)+.0323);
redSignal = integral(redFun,300,800);

greenFun = @(x1) 64.*exp(-((x1-525)./50).^2).*... %and green
    (exp(-((x1-550)./113).^2)+.0323);
greenSignal = integral(greenFun,300,800);

%Create observed spectra and calculate detected signal
blueErrFun = @(x2) 58.*exp(-((x2-470)./50).^2).*... %blue transmission function for
camera
    (exp(-((x2-550)./113).^2)+.0323).*... %Lamp illumination spectra
(1 + (.5*(cos(2*pi.*(111./x2-.156))-cos(2*pi.*(303./x2-.0574)))-1)); %Introducing
error due to retarder
blueErrSignal = integral(blueErrFun,300,800);

greenErrFun = @(x2) 64.*exp(-((x2-525)./50).^2).*... %green
    (exp(-((x2-550)./113).^2)+.0323).*...
(1 + (.5*(cos(2*pi.*(111./x2-.156))-cos(2*pi.*(303./x2-.0574)))-1));
greenErrSignal = integral(greenErrFun,300,800);

redErrFun = @(x2) 44.*exp(-((x2-640)./40).^2).*... %red
    (exp(-((x2-550)./113).^2)+.0323).*...
(1 + (.5*(cos(2*pi.*(111./x2-.156))-cos(2*pi.*(303./x2-.0574)))-1));
redErrSignal = integral(redErrFun,300,800);

%Calculate the error fraction between the actual and observed signals
blueErrSignalFraction = (blueErrSignal-blueSignal)/blueSignal
greenErrSignalFraction = (greenErrSignal-greenSignal)/greenSignal
redErrSignalFraction = (redErrSignal-redSignal)/redSignal

%Plot expected and observed spectra
figure;
plot(x1,redFun(x1))
hold on
plot(x1,blueFun(x1))
plot(x1,greenFun(x1))

figure;
plot(x1,redErrFun(x1))
hold on
plot(x1,blueErrFun(x1))
plot(x1,greenErrFun(x1))

```

## B-4. Functions

```
%GLARE MASK FUNCTION
```

```

%This function serves to apply Canny edge detection to identify glare in
%the supplied grayscale image and threshold value, then create a mask which
%describes the detected glare regions.

function [mask] = glareMask(image, threshold,dilation)

    edges = edge(image,'canny',threshold);

    fatEdges = imdilate(edges,strel('disk',dilation));

    mask = imfill(fatEdges,'holes'); %Mask returned by the function which includes
only the detected glare

%COLOR CHANNEL SEPARATION FUNCTION

%This function takes a Bayer-tiled image and returns three images of the
%red, green, and blue pixels, each with the other two color channel pixels
%suppressed

function [colorChannels] = colorChannelSeparator(im)
    colorChannels = zeros(length(im(:,1)),length(im(1,:)),3);
    imBlue = im; %Placeholders for writing image channels to
    imGreen = im;
    imRed = im;

    topLeft = false; %Initializing booleans
    bottomRight = true;

    %Usually bayer tiles are in the following configuration: GB RG This
    %configuration has green in the top left, blue in the top right, red in the
    %bottom left, and green in the bottom right. If this is not the config for
    %the loaded image, the following code may be modified by changing the
    %variable assignment under each comment.

    for j = 1:length(im(1,:));
        bottomRight = not(bottomRight);
        if not(bottomRight);
            for i = 1:length(im(:,1));
                topLeft = not(topLeft);
                if topLeft %Top left assignment
                    imBlue(i,j) = 0;
                    imGreen(i,j) = im(i,j);
                    imRed(i,j) = 0;
                else %Bottom left assignment
                    imBlue(i,j) = 0;
                    imGreen(i,j) = 0;
                    imRed(i,j) = im(i,j);
                end
            end
        end
    end

```

```

        end
    end
else
    for i = 1:length(im(:,1));
        bottomRight = not(bottomRight);
        if bottomRight %Bottom right assignment
            imBlue(i,j) = 0;
            imGreen(i,j) = im(i,j);
            imRed(i,j) = 0;
        else %Top right assignment
            imBlue(i,j) = im(i,j);
            imGreen(i,j) = 0;
            imRed(i,j) = 0;
        end
    end
end
end
colorChannels(:, :, 1) = imRed;
colorChannels(:, :, 2) = imGreen;
colorChannels(:, :, 3) = imBlue;

```

#### %IMAGE MASKING FUNCTION

%Applies a Boolean mask to a rgb or grayscale image, false pixels are set  
%to zero

```
function [imMasked] = maskImage(im,mask,type)
```

```

imMasked = im;

if strcmp(type, 'mono')
    for i = 1:length(im(:,1))
        for j = 1:length(im(1,:))
            if not(mask(i,j))
                imMasked(i,j) = 0;
            end
        end
    end
end

if strcmp(type, 'rgb')
    for i = 1:length(im(:,1,1))
        for j = 1:length(im(1,:,1))
            if not(mask(i,j))
                for k=1:3
                    imMasked(i,j,k) = 0;
                end
            end
        end
    end
end

```

```

        end
    end
end

%IMAGE NORMALIZING FUNCTION

%Normalize im1 to a point (x,y) in im2 in RGB or grayscale

function [imNorm] = normalizeImage(im1,im2,x,y,type)

    im1 = im2double(im1);
    im2 = im2double(im2);
    imNorm = im2;

    if strcmp(type, 'mono')
        imNorm = im2(y,x)/im1(y,x).*im1;
    end

    if strcmp(type, 'rgb')
        for i=1:3
            imNorm(:,:,i) = im2(y,x,i)/im1(y,x,i).*im1(:,:,i);
        end
    end

%ROW PLOTTING FUNCTION

%Plots the image intensity along the horizontal line bound by xMin and xMax
%at height c.

function [] = rowPlotter(im,c,xMin, xMax)

    x = xMin:xMax;
    y = zeros(length(x),1);

    for i= 1:length(x)
        y(i) = im(c,x(i));
    end
    figure()
    plot(x,y)

```

### C. Device Control Code

```

//Inclusions
#include "stdafx.h"
#include "FlyCapture2.h"
#include <iostream>

```

```

#include <sstream>
#include <stdio.h>
#include "LCC25_Api.h"
#include <iomanip>
#include <string.h>
#include <vector>
#include <assert.h>
#include <future>

//Namespace declaration
using namespace FlyCapture2;
using namespace std;

//Global variable instantiations and definitions
unsigned int imageCnt = 0; //Counter for difference images
unsigned int frameCnt = 0; //Counter for individual frames
bool modStart = false; //Boolean that tracks if framerate and switching have been
synchronized
const int k_numFrames = 500; //Number of frames for the camera to capture
const int k_numImages = k_numFrames/2; //Number of DPL images associated with the number
of frames
std::vector<Image> vecImages; //Vector to store collected images
char c[256]; //Retarder error string
Image paraImage; //Variable to store parallel image in
Image perpImage; //Variable to store perpendicular image in
Image diffImage; //Variable to store DPL image in
bool initializeDiffImage = true; //Boolean that tracks if the variable for the DPL image
has been initialized
bool polState = true; //Boolean that tracks the voltage state of the retarder

//Camera properties
Error error;
Property frameRateProp(FRAME_RATE);
CameraInfo camInfo;
FC2Config fc2Config;

//Video appending properties
enum AviType
{
    UNCOMPRESSED,
    MJPG,
    H264
};

//Printing camera information
void PrintBuildInfo()
{
    FC2Version fc2Version;
    Utilities::GetLibraryVersion(&fc2Version);

    ostringstream version;
    version << "FlyCapture2 library version: " << fc2Version.major << "."
        << fc2Version.minor << "." << fc2Version.type << "."
        << fc2Version.build;
    cout << version.str() << endl;
}

```



```

    ostream timeStamp;
    timeStamp << "Application build date: " << __DATE__ << " " << __TIME__;
    cout << timeStamp.str() << endl << endl;
}

void PrintCameraInfo(CameraInfo *pCamInfo)
{
    cout << endl;
    cout << "*** CAMERA INFORMATION ***" << endl;
    cout << "Serial number - " << pCamInfo->serialNumber << endl;
    cout << "Camera model - " << pCamInfo->modelName << endl;
    cout << "Camera vendor - " << pCamInfo->vendorName << endl;
    cout << "Sensor - " << pCamInfo->sensorInfo << endl;
    cout << "Resolution - " << pCamInfo->sensorResolution << endl;
    cout << "Firmware version - " << pCamInfo->firmwareVersion << endl;
    cout << "Firmware build time - " << pCamInfo->firmwareBuildTime << endl
        << endl;
}

void PrintError(Error error) { error.PrintErrorTrace(); }

//Function for taking the difference of two 16 bit mono images, called in OnImageGrabbed
void ImageDifference(Image* differenceImage, Image* minuendImage, Image* subtrahendImage)
{
    // This image difference routine only works for mono, 16-bit images.
    // cast the image data pointer to point to unsigned short int* instead of unsigned
    char*
    unsigned short int* p16BitMinuendImageData = reinterpret_cast<unsigned short
    int*>(minuendImage->GetData());
    unsigned short int* p16BitSubtrahendImageData = reinterpret_cast<unsigned short
    int*>(subtrahendImage->GetData());
    unsigned short int* p16BitDifferenceImageData = reinterpret_cast<unsigned short
    int*>(differenceImage->GetData());
    // With the cast to a 16-bit data type, the image "size" must be adjusted (in this
    case halved).
    unsigned int castImageSize = minuendImage->GetDataSize() / sizeof
    *p16BitMinuendImageData;

    for (unsigned int index = 0; index < castImageSize; index++)
    {
        p16BitDifferenceImageData[index] = p16BitMinuendImageData[index] -
        p16BitSubtrahendImageData[index];
    }
}

// User-supplied callback function to run when an event (end of camera exposure) is
triggered.
void ModSimpleCallback(void *cbData)
{
    if (!modStart)
    {
        fnLCC25_DLL_SetOutputMode(0, 0);
        modStart = !modStart;
    }
    cout << "Callback executes.\n";
    return;
}

```

```

}

// User-supplied callback function to run when an image is read from the camera.
void OnImageGrabbed(Image *pImage, const void *pCallbackData)
{
    if (frameCnt < k_numFrames) {
        if (polState) {
            paraImage = *pImage;
            if (initializeDiffImage) { //Initialize variable to hold difference
                image
                    diffImage = paraImage;
                    initializeDiffImage = !initializeDiffImage;
            }
        }
        else {
            perpImage = *pImage;
            ImageDifference(&diffImage, &paraImage, &perpImage);
            vecImages[imageCnt].DeepCopy(&diffImage);
            imageCnt++;
        }
    }
    polState = !polState;
    frameCnt++;
    cout << "Frame " << frameCnt << " Recieved.\n";
    return;
}

// Trigger a single camera to start streaming images, calling ModSimpleCallback on the
// first end of exposure event and OnImageGrabbed on each image read
int RunSingleCamera(PGRGuid guid)
{
    // Context variable
    Camera cam;

    // Connect to a camera
    error = cam.Connect(&guid);
    if (error != PGRERROR_OK)
    {
        PrintError(error);
        return -1;
    }

    //Get camera framerate
    error = cam.GetProperty(&frameRateProp);
    if (error != PGRERROR_OK)
    {
        PrintError(error);
        return -1;
    }

    //Wavelength retarder initialization
    int ret = Init();
    assert(ret == 0);
    int hdl = 0;
    char sn[256] = "COM4";
    char a = 'e';
}

```

```

char c[256];
memset(c, 0, sizeof(c));
hdl = fnLCC25_DLL_Open(sn);
assert(hdl == 0);

//Setting operating voltages
ret = fnLCC25_DLL_SetVoltage1(hdl, 1.4); //Set parallel voltage
assert(ret == 0);
ret = fnLCC25_DLL_SetVoltage2(hdl, 25); //Set perpendicular voltage
assert(ret == 0);

//Sets voltage switching frequency to half camera framerate
ret = fnLCC25_DLL_SetFrequency(hdl, (frameRateProp.absValue)/2);
assert(ret == 0);
ret = fnLCC25_DLL_SetOutputMode(hdl, 1);
assert(ret == 0);
ret = fnLCC25_DLL_SetOutputEnable(hdl, 1);
assert(ret == 0);
cout << "Retarder Initialized.\n" << endl;

// Register the End of Exposure (EoE) event and tie it to ModSimpleCallback.
EventOptions optEOE;
optEOE.EventName = "EventExposureEnd";
optEOE.EventCallbackFcn = &ModSimpleCallback;
CustomUserDataStruct UserDataEOE = {1, 'a'};

// Clear previously registered events.
error = cam.DeregisterAllEvents();
if (error != PGRERROR_OK)
{
    PrintError(error);
    return (-1);
}

// Register our event
error = cam.RegisterEvent(&optEOE);

if (error != PGRERROR_OK)
{
    PrintError(error);
    return (-1);
}
else
{
    cout << "Successfully registered event:" << optEOE.EventName << endl;
}

// Get the camera information (serial number, capabilities, etc)
CameraInfo camInfo;
error = cam.GetCameraInfo(&camInfo);
if (error != PGRERROR_OK)
{
    PrintError(error);
    return -1;
}

```

```

PrintCameraInfo(&camInfo);

//Resize image vector to fit all the images
vecImages.resize(k_numImages);

// Start reading images from the camera, executing callback OnImageGrabbed with each
image read.
error = cam.StartCapture(OnImageGrabbed);
if (error != PGRERROR_OK)
{
    PrintError(error);
    return -1;
}

//Continue capture until all frames captured
while (frameCnt < k_numFrames)
{
    const unsigned int millisecondsToSleep = 1000 / frameRateProp.absValue;
    #if defined(_WIN32) || defined(_WIN64)
        Sleep(millisecondsToSleep);
    #else
        usleep(millisecondsToSleep * 1000);
    #endif
}

// Stop capturing images
error = cam.StopCapture();
if (error != PGRERROR_OK)
{
    PrintError(error);
    return -1;
}

// De-register all events before disconnecting from camera
cam.DeregisterAllEvents();

// Disconnect the camera
error = cam.Disconnect();
if (error != PGRERROR_OK)
{
    PrintError(error);
    return -1;
}
return 0;
}

// Function to append collected image vector into avi video
void SaveAviHelper(AviType aviType, std::vector<Image> &vecImages, std::string
aviFileName, float frameRate)
{
    AVIRecorder aviRecorder;

    // Open the AVI file for appending images
    switch (aviType)
    {

```

```

case UNCOMPRESSED:
{
    AVIOption option;
    option.frameRate = frameRate;
    error = aviRecorder.AVIOpen(aviFileName.c_str(), &option);
}
break;
case MJPG:
{
    MJPGOption option;
    option.frameRate = frameRate;
    option.quality = 75;
    error = aviRecorder.AVIOpen(aviFileName.c_str(), &option);
}
break;
case H264:
{
    H264Option option;
    option.frameRate = frameRate;
    option.bitrate = 1000000;
    option.height = vecImages[0].GetRows();
    option.width = vecImages[0].GetCols();
    error = aviRecorder.AVIOpen(aviFileName.c_str(), &option);
}
break;
}

if (error != PGRERROR_OK)
{
    PrintError(error);
    return;
}

cout << endl;
cout << "Appending " << vecImages.size()
    << " images to AVI file: " << aviFileName.c_str() << endl;
for (int imageCnt = 0; imageCnt < vecImages.size(); imageCnt++)
{
    // Append the image to AVI file
    error = aviRecorder.AVIAppend(&vecImages[imageCnt]);
    if (error != PGRERROR_OK)
    {
        PrintError(error);
        continue;
    }

    cout << "Appended image " << imageCnt << "..." << endl;
}

// Close the AVI file
error = aviRecorder.AVIClose();
if (error != PGRERROR_OK)
{
    PrintError(error);
    return;
}
}

```

```

}

// Main entry point
int main(int /*argc*/, char ** /*argv*/)
{
    PrintBuildInfo();

    Error error;

    // Since this application saves images in the current folder
    // we must ensure that we have permission to write to this folder.
    // If we do not have permission, fail right away.
    FILE *tempFile = fopen("test.txt", "w+");
    if (tempFile == NULL)
    {
        cout << "Failed to create file in current folder. Please check "
             << "permissions."
             << endl;
        return -1;
    }
    fclose(tempFile);
    remove("test.txt");

    // Create a Bus Manager instance so we can query all connected cameras.
    BusManager busMgr;
    unsigned int numCameras;
    error = busMgr.GetNumOfCameras(&numCameras);
    if (error != PGRERROR_OK)
    {
        PrintError(error);
        return -1;
    }
    cout << "Number of cameras detected: " << numCameras << endl;

    // Get a handle to an individual camera, and start to receive images and
    // execute callbacks
    for (unsigned int i = 0; i < numCameras; i++)
    {
        PGRGuid guid;
        error = busMgr.GetCameraFromIndex(i, &guid);
        if (error != PGRERROR_OK)
        {
            PrintError(error);
            return -1;
        }

        //Here is where the camera is actually operated
        RunSingleCamera(guid);
    }

    //Appending image vector to avi video
    cout << "Using frame rate of " << fixed << setprecision(1) <<
         frameRateProp.absValue/2 << endl;

    ostringstream aviFileName;

```

```

aviFileName << "SaveImageToAviEx-Uncompressed-" << camInfo.serialNumber;
SaveAviHelper(
    UNCOMPRESSED, vecImages, aviFileName.str().c_str(),
    (frameRateProp.absValue)/2);

cout << "Done! Press Enter to exit..." << endl;
cin.ignore();

return 0;
}

```

#### D. Thorlabs LCC111125-A Variable Retarder Performance Data

Retardance by Wavelength at 25 °C			
Driver RMS Voltage	405 nm	635 nm	
0.1	1.32434	0.74277	
0.2	1.32544	0.74248	
0.3	1.32603	0.7423	
0.4	1.32507	0.74197	
0.5	1.32317	0.74129	
0.6	1.32023	0.73986	
0.7	1.31304	0.73495	
0.8	1.28526	0.71319	
0.9	1.2179	0.66649	
1	1.15237	0.61918	
1.02	1.14317	0.60874	
1.04	1.13727	0.5991	
1.06	1.13365	0.58939	
1.08	1.13147	0.57975	
1.1	0.86702	0.57049	
1.12	0.8627	0.56067	
1.14	0.85547	0.55151	
1.16	0.84666	0.5418	
1.18	0.83642	0.53288	
1.2	0.82592	0.52554	
1.22	0.81251	0.51624	
1.24	0.79953	0.50731	
1.26	0.7867	0.5	
1.28	0.77327	0.48833	
1.3	0.7601	0.47559	
1.32	0.74686	0.46484	
1.34	0.73316	0.45339	
1.36	0.7195	0.44193	

<b>1.38</b>	0.70591	0.43124
<b>1.4</b>	0.69188	0.4205
<b>1.42</b>	0.67891	0.41033
<b>1.44</b>	0.66547	0.40117
<b>1.46</b>	0.65309	0.39182
<b>1.48</b>	0.64075	0.38295
<b>1.5</b>	0.62879	0.37469
<b>1.52</b>	0.61854	0.36656
<b>1.54</b>	0.60618	0.35853
<b>1.56</b>	0.59499	0.35078
<b>1.58</b>	0.58254	0.34325
<b>1.6</b>	0.56993	0.33595
<b>1.62</b>	0.55882	0.32912
<b>1.64</b>	0.54658	0.32229
<b>1.66</b>	0.53677	0.31554
<b>1.68</b>	0.52695	0.30933
<b>1.7</b>	0.51801	0.30325
<b>1.72</b>	0.5	0.29697
<b>1.74</b>	0.49609	0.29108
<b>1.76</b>	0.49414	0.28545
<b>1.78</b>	0.49805	0.27999
<b>1.8</b>	0.48242	0.27454
<b>1.82</b>	0.46834	0.26922
<b>1.84</b>	0.46149	0.26401
<b>1.86</b>	0.45342	0.25898
<b>1.88</b>	0.44584	0.2542
<b>1.9</b>	0.43717	0.24944
<b>1.92</b>	0.4275	0.24468
<b>1.94</b>	0.42084	0.24021
<b>1.96</b>	0.41684	0.23577
<b>1.98</b>	0.40854	0.2315
<b>2</b>	0.40384	0.22739
<b>2.02</b>	0.39727	0.22335
<b>2.04</b>	0.39207	0.21945
<b>2.06</b>	0.38538	0.21585
<b>2.08</b>	0.37951	0.21242
<b>2.1</b>	0.37326	0.20899
<b>2.12</b>	0.36681	0.20581
<b>2.14</b>	0.36186	0.20269
<b>2.16</b>	0.35723	0.19984
<b>2.18</b>	0.35274	0.19713



<b>2.2</b>	0.34738	0.19449
<b>2.22</b>	0.34326	0.19201
<b>2.24</b>	0.33907	0.18948
<b>2.26</b>	0.33509	0.18702
<b>2.28</b>	0.32972	0.18469
<b>2.3</b>	0.3254	0.18235
<b>2.32</b>	0.32189	0.18022
<b>2.34</b>	0.31809	0.17777
<b>2.36</b>	0.31441	0.17563
<b>2.38</b>	0.31083	0.17358
<b>2.4</b>	0.3075	0.17138
<b>2.42</b>	0.30418	0.16948
<b>2.44</b>	0.30098	0.16752
<b>2.46</b>	0.29792	0.16564
<b>2.48</b>	0.29466	0.16374
<b>2.5</b>	0.29092	0.16191
<b>2.52</b>	0.28853	0.16016
<b>2.54</b>	0.28519	0.15842
<b>2.56</b>	0.28215	0.15664
<b>2.58</b>	0.27979	0.15505
<b>2.6</b>	0.27759	0.15348
<b>2.62</b>	0.27563	0.15169
<b>2.64</b>	0.2728	0.15007
<b>2.66</b>	0.27035	0.14855
<b>2.68</b>	0.2672	0.14693
<b>2.7</b>	0.26533	0.14538
<b>2.72</b>	0.26237	0.14385
<b>2.74</b>	0.26019	0.14222
<b>2.76</b>	0.25833	0.14085
<b>2.78</b>	0.25575	0.13919
<b>2.8</b>	0.25495	0.13759
<b>2.82</b>	0.25319	0.13618
<b>2.84</b>	0.25119	0.13459
<b>2.86</b>	0.24841	0.13316
<b>2.88</b>	0.24702	0.1315
<b>2.9</b>	0.24422	0.13008
<b>2.92</b>	0.24332	0.12843
<b>2.94</b>	0.2415	0.12713
<b>2.96</b>	0.24027	0.12561
<b>2.98</b>	0.2387	0.12427
<b>3</b>	0.23787	0.12294

<b>3.1</b>	0.22988	0.1175
<b>3.2</b>	0.22267	0.11248
<b>3.3</b>	0.21387	0.10813
<b>3.4</b>	0.20965	0.10388
<b>3.5</b>	0.20421	0.10002
<b>3.6</b>	0.19873	0.09654
<b>3.7</b>	0.19417	0.09326
<b>3.8</b>	0.19068	0.09022
<b>3.9</b>	0.18733	0.08736
<b>4</b>	0.18405	0.08474
<b>4.1</b>	0.18097	0.08232
<b>4.2</b>	0.17782	0.08
<b>4.3</b>	0.17509	0.07782
<b>4.4</b>	0.17149	0.07596
<b>4.5</b>	0.16709	0.07415
<b>4.6</b>	0.16615	0.07245
<b>4.7</b>	0.16668	0.07092
<b>4.8</b>	0.16568	0.06968
<b>4.9</b>	0.16439	0.06841
<b>5</b>	0.16195	0.06718
<b>5.1</b>	0.16031	0.06595
<b>5.2</b>	0.15883	0.06481
<b>5.3</b>	0.15711	0.06364
<b>5.4</b>	0.1556	0.06254
<b>5.5</b>	0.15415	0.06143
<b>5.6</b>	0.15329	0.06037
<b>5.7</b>	0.15227	0.05928
<b>5.8</b>	0.15076	0.05838
<b>5.9</b>	0.14871	0.0574
<b>6</b>	0.14887	0.05648
<b>6.1</b>	0.14763	0.05548
<b>6.2</b>	0.14615	0.05464
<b>6.3</b>	0.14594	0.05374
<b>6.4</b>	0.14444	0.05294
<b>6.5</b>	0.14364	0.05211
<b>6.6</b>	0.14375	0.05143
<b>6.7</b>	0.14302	0.05059
<b>6.8</b>	0.14126	0.04983
<b>6.9</b>	0.14148	0.04916
<b>7</b>	0.14035	0.04853
<b>7.1</b>	0.13996	0.04774

<b>7.2</b>	0.13892	0.04714
<b>7.3</b>	0.13835	0.04649
<b>7.4</b>	0.13771	0.04581
<b>7.5</b>	0.13768	0.04524
<b>7.6</b>	0.13751	0.04461
<b>7.7</b>	0.13518	0.04389
<b>7.8</b>	0.13695	0.04341
<b>7.9</b>	0.13616	0.0427
<b>8</b>	0.13551	0.04227
<b>8.1</b>	0.13521	0.04154
<b>8.2</b>	0.13398	0.04107
<b>8.3</b>	0.13409	0.04045
<b>8.4</b>	0.1345	0.03976
<b>8.5</b>	0.13401	0.03917
<b>8.6</b>	0.13332	0.03857
<b>8.7</b>	0.13333	0.03792
<b>8.8</b>	0.13251	0.03739
<b>8.9</b>	0.12599	0.03699
<b>9</b>	0.128	0.03646
<b>9.1</b>	0.12846	0.03604
<b>9.2</b>	0.12773	0.03726
<b>9.3</b>	0.12826	0.03827
<b>9.4</b>	0.12851	0.0374
<b>9.5</b>	0.12783	0.03685
<b>9.6</b>	0.12709	0.03626
<b>9.7</b>	0.12731	0.03583
<b>9.8</b>	0.12731	0.03522
<b>9.9</b>	0.12703	0.03456
<b>10</b>	0.12728	0.03422
<b>10.2</b>	0.12609	0.03308
<b>10.4</b>	0.12676	0.0323
<b>10.6</b>	0.12699	0.03165
<b>10.8</b>	0.1258	0.03099
<b>11</b>	0.12619	0.0303
<b>11.2</b>	0.12546	0.02975
<b>11.4</b>	0.1253	0.02928
<b>11.6</b>	0.12496	0.0288
<b>11.8</b>	0.12465	0.02846
<b>12</b>	0.12463	0.02809
<b>12.2</b>	0.1246	0.02765
<b>12.4</b>	0.12397	0.02741

<b>12.6</b>	0.12383	0.02691
<b>12.8</b>	0.12288	0.02657
<b>13</b>	0.12262	0.02625
<b>13.2</b>	0.12298	0.02602
<b>13.4</b>	0.12188	0.02562
<b>13.6</b>	0.12258	0.02539
<b>13.8</b>	0.12353	0.02503
<b>14</b>	0.12303	0.02478
<b>14.2</b>	0.12207	0.02473
<b>14.4</b>	0.12207	0.02437
<b>14.6</b>	0.12215	0.02431
<b>14.8</b>	0.12181	0.02412
<b>15</b>	0.12151	0.02402
<b>15.2</b>	0.1215	0.0238
<b>15.4</b>	0.12233	0.02365
<b>15.6</b>	0.12196	0.02369
<b>15.8</b>	0.12276	0.02349
<b>16</b>	0.12212	0.02342
<b>16.2</b>	0.12226	0.02337
<b>16.4</b>	0.12282	0.02298
<b>16.6</b>	0.12255	0.02289
<b>16.8</b>	0.12196	0.02286
<b>17</b>	0.12139	0.02253
<b>17.2</b>	0.12125	0.02258
<b>17.4</b>	0.12082	0.02251
<b>17.6</b>	0.12165	0.02232
<b>17.8</b>	0.12191	0.02232
<b>18</b>	0.12078	0.02236
<b>18.2</b>	0.1215	0.0223
<b>18.4</b>	0.12115	0.02206
<b>18.6</b>	0.11939	0.02195
<b>18.8</b>	0.12002	0.02198
<b>19</b>	0.12073	0.02182
<b>19.2</b>	0.1201	0.02173
<b>19.4</b>	0.12014	0.02168
<b>19.6</b>	0.12005	0.02171
<b>19.8</b>	0.12089	0.02131
<b>20</b>	0.12023	0.02123
<b>20.2</b>	0.11947	0.02117
<b>20.4</b>	0.11843	0.02099
<b>20.6</b>	0.11833	0.021

<b>20.8</b>	0.11903	0.02102
<b>21</b>	0.1201	0.02085
<b>21.2</b>	0.12075	0.02072
<b>21.4</b>	0.11854	0.02077
<b>21.6</b>	0.11764	0.02062
<b>21.8</b>	0.11592	0.0204
<b>22</b>	0.11799	0.02051
<b>22.2</b>	0.11708	0.02026
<b>22.4</b>	0.11778	0.02027
<b>22.6</b>	0.11748	0.02027
<b>22.8</b>	0.11735	0.02018
<b>23</b>	0.11765	0.02017
<b>23.2</b>	0.11804	0.02015
<b>23.4</b>	0.11819	0.02024
<b>23.6</b>	0.11889	0.01995
<b>23.8</b>	0.11914	0.02006
<b>24</b>	0.1184	0.01995
<b>24.2</b>	0.11895	0.01981
<b>24.4</b>	0.11886	0.01984
<b>24.6</b>	0.1187	0.01988
<b>24.8</b>	0.11924	0.01975
<b>25</b>	0.11931	0.01974

## BIBLIOGRAPHY

- 1) Abid, H., Charif, I., Mellouki, I., Aqodad, N., Benajah, D., Ibrahim, A., . . . Yousfi, M. E. (2013). Role of laparoscopy in diagnosis of peritoneal tuberculosis (About 414 cases). *Open Journal of Gastroenterology*, 03(03), 205-207. doi:10.4236/ojgas.2013.33033
- 2) Albert Cerussi, Natasha Shah, David Hsiang; Amanda Durkin, John Butler, Bruce J. Tromberg. *J. Biomed. Opt.* 11(4), 044005 (September 05, 2006). doi:10.1117/1.2337546
- 3) Arnfield, M. R., Chapman, J. D., Tulip, J., Fenning, M. C. and McPhee, M. S. (1993), optical properties of experimental prostate tumors in vivo. *Photochemistry and Photobiology*, 57: 306–311. doi:10.1111/j.1751-1097.1993.tb02292.x
- 4) Bashkatov, A.N., Genina, E.A., Kozintseva, M.D. et al. (2016). Optical properties of peritoneal biological tissues in the spectral range of 350–2500 nm. *Opt. Spectrosc.* 120: 1. doi:10.1134/S0030400X16010045
- 5) Bass, M., Van Stryland, E. W., Williams, D. R., & Wolfe, W. L. (1995). *Handbook of Optics: Fundamentals, Techniques, & Design* (2nd ed., Vol. 1). New York City, N.Y.: McGraw-Hill.
- 6) Bayer, B. E. (1976). U.S. Patent No. US3971065 A. Washington, DC: U.S. Patent and Trademark Office.
- 7) Cancer Statistics. (2017). Retrieved from <https://seer.cancer.gov/>
- 8) Canny, J. (1986). A Computational Approach to Edge Detection. *Readings in Computer Vision, PAMI-8*(6), 679- 698. doi:10.1016/b978-0-08-051581-6.50024-6
- 9) Clancy, N. T., Arya, S., Qi, J., Stoyanov, D., Hanna, G. B., & Elson, D. S. (2014). Polarised stereo endoscope and narrowband detection for minimal access surgery. *Biomedical Optics Express*, 5(12), 4108. doi:10.1364/boe.5.004108
- 10) Demos, S. G., & Alfano, R. R. (1997). Optical polarization imaging. *Applied Optics*, 36(1), 150. doi:10.1364/ao.36.000150
- 11) Demos, S. G., Papadopoulos, A. J., Savage, H., Heerdt, A. S., Schantz, S., & Alfano, R. R. (1997). Polarization Filter for Biomedical Tissue Optical Imaging. *Photochemistry and Photobiology*, 66(6), 821-825. doi:10.1111/j.1751-1097.1997.tb03231.x
- 12) Demos, S. G., Radousky, H. B., & Alfano, R. R. (2000). Deep subsurface imaging in tissues using spectral and polarization filtering. *Optics Express*, 7(1), 23-28.
- 13) Eickhoff, E. (2014). *Enhanced Imaging Laparoscope to Improve Visualization of Superficial Metastases*. Tufts University.

- 14) FLIR Integrated Imaging Solutions. (2017). *BFLY-PGE-23S2C-CS Imaging Performance*. Retrieved from <https://www.ptgrey.com/support/downloads/10107>
- 15) Franko, J. (n.d.). Cytoreductive Surgery [SEP] & HIPEC. Retrieved April 03, 2017, from [http://www.cancersurgery.us/Cancer\\_Surgery/Cytoreductive\\_Surgery\\_%26\\_HIPEC.html](http://www.cancersurgery.us/Cancer_Surgery/Cytoreductive_Surgery_%26_HIPEC.html)
- 16) Fujimura, T., Kinami, S., Ninomiya, I., Kitagawa, H., Fuchida, S., Nishimura, G., . . . Miwa, K. (2002). Diagnostic Laparoscopy, Serum CA125, and Peritoneal Metastasis in Gastric Cancer. *Endoscopy*, *34*(7), 569-574. doi:10.1055/s-2002-33228
- 17) Ghosh, N., Vitkin, I. A. & Wood, M. F. G. Mueller matrix decomposition for extraction of individual polarization parameters from complex turbid media exhibiting multiple scattering, optical activity, and linear birefringence. *J. Biomed. Opt.* *13*, 044036–044036 (2008).
- 18) Gono, K., Yamazaki, K., Doguchi, N., Nonami, T., Obi, T., Yamaguchi, M., . . . Endo, T. (2003). Endoscopic Observation of Tissue by Narrowband Illumination. *Optical Review*, *10*(4), 211-215. doi:10.1007/s10043-003-0211-8
- 19) Green PH, O'Toole KM, Slonim D, et al.: Increasing incidence and excellent survival of patients with early gastric cancer: experience in a United States medical center. *Am J Med* *85* (5): 658-61, 1988.
- 20) Greening GJ, Istfan R, Higgins LM, et al; Characterization of thin poly(dimethylsiloxane)-based tissue-simulating phantoms with tunable reduced scattering and absorption coefficients at visible and near-infrared wavelengths. *J. Biomed. Opt.* *0001;19*(11):115002. doi:10.1117/1.JBO.19.11.115002
- 21) Gurjar, R. S., Backman, V., Perelman, L. T., Georgakoudi, I., Badizadegan, K., Itzkan, I., . . . Feld, M. S. (2001). Imaging human epithelial properties with polarized light-scattering spectroscopy. *Nature Medicine*, *7*(11), 1245-1248. doi:10.1038/nm1101-1245
- 22) Hecht, E. (2017). *Optics* (5th ed.). Boston, MA: Pearson Education.
- 23) Honda, N., Kariyama, Y., Hazama, H., Ishii, T., Kitajima, Y., Inoue, K., . . . Awazu, K. (2015). Optical properties of tumor tissues grown on the chorioallantoic membrane of chicken eggs: tumor model to assay of tumor response to photodynamic therapy. *Journal of Biomedical Optics*, *20*(12), 125001. doi:10.1117/1.jbo.20.12.125001
- 24) Hunter, M., Backman, V., Popescu, G., Kalashnikov, M., Boone, C. W., Wax, A., . . . Feld, M. S. (2006). Tissue Self-Affinity and Polarized Light Scattering in the Born Approximation: A New Model for Precancer Detection. *Physical Review Letters*, *97*(13). doi:10.1103/physrevlett.97.138102
- 25) Jacques, S. L. (2002). U.S. Patent No. US6437856 B1. Washington, DC: U.S. Patent and Trademark Office.

- 26) Jacques, S. L., Roman, J. R., & Lee, K. (2000). Imaging Superficial Tissues with polarized light. *Lasers in Surgery and Medicine*, 26, 119-129.
- 27) Keller, C. U. (2008). *Lecture 6: Fixed Retarders*. Lecture presented at International Summer School On Solar Polarization in South Sichuan's Bamboo Sea, Sichuan Province. Retrieved from [http://home.strw.leidenuniv.nl/~keller/Teaching/China\\_2008/CUK\\_L07\\_handout.pdf](http://home.strw.leidenuniv.nl/~keller/Teaching/China_2008/CUK_L07_handout.pdf)
- 28) Kelsen DP: Postoperative adjuvant chemoradiation therapy for patients with resected gastric cancer: intergroup 116. *J Clin Oncol* 18 (21 Suppl): 32S-4S, 2000.
- 29) Kozintseva, M. D., Bashkatov, A. N., Kochubey, V. I., Genina, E. A., Gorodkov, S. Y., Morozov, D. A., & Tuchin, V. V. (2014). Optical properties of parietal peritoneum in the spectral range 350-2500 nm. *Saratov Fall Meeting 2013: Optical Technologies in Biophysics and Medicine XV; and Laser Physics and Photonics XV*. doi:10.1117/12.2051685
- 30) Levy, A. D., Shaw, J. C., & Sobin, L. H. (2009). Secondary Tumors and Tumorlike Lesions of the Peritoneal Cavity: Imaging Features with Pathologic Correlation. *RadioGraphics*, 29(2), 347-373. doi:10.1148/rg.292085189
- 31) Meadowlark Optics. (2005). Sources of Error in Retarders and Waveplates. Retrieved from <http://www.meadowlark.com/store/applicationNotes/Sources%20of%20Error%20in%20Retarders%20and%20Waveplates.pdf>
- 32) Morgan, S. P., & Stockford, I. M. (2003, February 15). Surface-reflection elimination in polarization imaging of superficial tissue. *Optics Letters Opt. Lett.*, 28(2), 114-116. doi:10.1364/ol.28.000114
- 33) Morgan, S., & Ridgway, M. (2000). Polarization properties of light backscattered from a two layer scattering medium. *Opt. Express Optics Express*, 7(12), 395. doi:10.1364/oe.7.000395
- 34) Muto, M., Horimatsu, T., Ezoe, Y., Hori, K., Yukawa, Y., Morita, S., . . . Chiba, T. (2009). Narrow-band imaging of the gastrointestinal tract. *Journal of Gastroenterology*, 44, 13-25.
- 35) Myakov, A., Nieman, L., Wicky, L., Utzinger, U., Richards-Kortum, R., & Sokolov, K. (2002). Fiber optic probe for polarized reflectance spectroscopy in vivo: Design and performance. *Journal of Biomedical Optics*, 7(3), 388. doi:10.1117/1.1483314
- 36) Nazarov, R., Jin, H., & Kaplan, D. L. (2004). Porous 3-D Scaffolds from Regenerated Silk Fibroin. *Biomacromolecules*, 5(3), 718-726. doi:10.1021/bm034327e
- 37) National Institute of Health. "Gastric Cancer Treatment." (2017, April 27). Retrieved from <https://www.cancer.gov/types/stomach/patient/stomach-treatment-pdq>



- 38) Paola Di Ninni, Fabrizio Martelli, and Giovanni Zaccanti, "The use of India ink in tissue-simulating phantoms," *Opt. Express* 18, 26854-26865 (2010)
- 39) Peli, E. (1990). Contrast in complex images. *Journal of the Optical Society of America A*, 7(10), 2032. doi:10.1364/josaa.7.002032
- 40) Qi, J., Barrière, C., Wood, T. C., & Elson, D. S. (2012). Polarized multispectral imaging in a rigid endoscope based on elastic light scattering spectroscopy. *Biomedical Optics Express*, 3(9), 2087. doi:10.1364/boe.3.002087
- 41) Qi, J., & Elson, D. S. (2016). A high definition Mueller polarimetric endoscope for tissue characterisation. *Scientific Reports*, 6(1). doi:10.1038/srep25953
- 42) Qi, J., Ye, M., Singh, M., Clancy, N. T., & Elson, D. S. (2013). Narrow band  $3 \times 3$  Mueller polarimetric endoscopy. *Biomedical Optics Express*, 4(11), 2433. doi:10.1364/boe.4.002433
- 43) Schnelldorfer, T., Gagnon, A. I., Birkett, R. T., Reynolds, G., Murphy, K. M., & Jenkins, R. L. (2014). Staging Laparoscopy in Pancreatic Cancer: A Potential Role for Advanced Laparoscopic Techniques. *Journal of the American College of Surgeons*, 218(6), 1201-1206. doi:10.1016/j.jamcollsurg.2014.02.018
- 44) Siegel, R. L., Miller, K. D., & Jemal, A. (2017). Cancer statistics, 2017. *CA: A Cancer Journal for Clinicians*, 67(1), 7-30. doi:10.3322/caac.21387
- 45) Stockford, I. M., Morgan, S. P., Chang, P. C., & Walker, J. G. (2002). Analysis of the spatial distribution of polarized light backscattered from layered scattering media. *J. Biomed. Opt.* *Journal of Biomedical Optics*, 7(3), 313. doi:10.1117/1.1483316
- 46) Stratasys. (2016). *Polyjet Materials Data Sheet*. Retrieved from the Stratasys, Ltd. website html [http://global72.stratasys.com/~//media/Main/Files/Material\\_Spec\\_Sheets/MSS\\_PJ\\_PJMaterialsDataSheet.pdf#\\_ga=1.55962667.188213582.1491971381](http://global72.stratasys.com/~//media/Main/Files/Material_Spec_Sheets/MSS_PJ_PJMaterialsDataSheet.pdf#_ga=1.55962667.188213582.1491971381)
- 47) Tata, D., Foresti, M., Cordero, J., Tomashefsky, P., Alfano, M., & Alfano, R. (1986). Fluorescence polarization spectroscopy and time-resolved fluorescence kinetics of native cancerous and normal rat kidney tissues. *Biophysical Journal*, 50(3), 463-469. doi:10.1016/s0006-3495(86)83483-x
- 48) Thekkek, N., Pierce, M. C., Lee, M. H., Polydorides, A. D., Flores, R. M., Anandasabapathy, S., & Richards-Kortum, R. R. (2013). Modular video endoscopy for in vivo cross-polarized and vital-dye fluorescence imaging of Barrett's-associated neoplasia. *Journal of Biomedical Optics*, 18(2), 026007. doi:10.1117/1.jbo.18.2.026007
- 49) Thorlabs. (2017). *LC Retarder Performance*. Retrieved from the Thorlabs, Inc. website html [https://www.thorlabs.com/newgroupage9.cfm?objectgroup\\_id=4182&pn=LCC25](https://www.thorlabs.com/newgroupage9.cfm?objectgroup_id=4182&pn=LCC25)

- 50) Wang, H., Zhu, T. C., Putt, M. E., Solonenko, M., Metz, J., Dimofte, A., . . . Yodh, A. G. (2005). Broadband reflectance measurements of light penetration, blood oxygenation, hemoglobin concentration, and drug concentration in human intraperitoneal tissues before and after photodynamic therapy. *Journal of Biomedical Optics*, 10(1), 014004. doi:10.1117/1.1854679
- 51) Wood, T. C., & Elson, D. S. (2010). Polarization response measurement and simulation of rigid endoscopes. *Biomedical Optics Express*, 1(2), 463. doi:10.1364/boe.1.000463
- 52) Yaroslavsky, A. N., Barbosa, J., Neel, V., Dimarzio, C., & Anderson, R. R. (2005). Combining multispectral polarized light imaging and confocal microscopy for localization of nonmelanoma skin cancer. *Journal of Biomedical Optics*, 10(1), 014011. doi:10.1117/1.1854173
- 53) Yaroslavsky, A. N., Neel, V., & Anderson, R. R. (2004). Fluorescence polarization imaging for delineating nonmelanoma skin cancers. *Optics Letters*, 29(17), 2010. doi:10.1364/ol.29.002010